COUPLING-OF-MODES STUDIES OF SURFACE ACOUSTIC WAVE OSCILLATORS AND DEVICES

by

P.J. Edmonson, Dipl.T., B.Eng., M.Eng., P. Eng.

A Thesis

Submitted to the School of Graduate Studies

in Partial Fulfilment of the Requirements

for the Degree

Doctor of Philosophy

McMaster University

February 1995

COUPLING-OF-MODES STUDIES OF SURFACE ACOUSTIC WAVE OSCILLATORS AND DEVICES

DOCTOR OF PHILOSOPHY (1995) McMaster University

(Electrical Engineering) Hamilton, ON., Canada

TITLE: **Coupling-of-Modes Studies of Surface Acoustic Wave Oscillators and Devices**

AUTHOR: Peter John Edmonson, Dipl.T. (Mohawk College)

B. Eng. (McMaster)

M. Eng. (McMaster)

P. Eng. (Province of Ontario)

SUPERVISORS: Prof. C.K. Campbell, Ph.D., D. Sc., FRSC, FIEEE, FEIC, FRSA, P. Eng.

Prof. P.M. Smith, B. Eng & Mgt, M. Eng., Ph.D.

NUMBER OF PAGES: xiv, 152

ABSTRACT

Recent advances in the area of communications has inspired the concept of ubiquitous coverage onto the market place. A pocket-size mobile unit will be able to provide two-way messaging on a global perspective. In order to realize this "radio on a chip" philosophy small, rugged, low power and inexpensive components must be designed. In this thesis, new circuits and devices that meet this communication challenge are examined. These involve the use of surface acoustic wave (SAW) components and devices.

The coupling-of-modes theory is used to study the effects of injecting a very small stimulus signal into a SAW oscillator loop. This diminutive injected signal may force the loop, if the conditions prevail, to follow and track it. These injection-locked oscillators (ILOs) follow the theory of phase locked loops (PLLs) to provide circuits suitable for amplification and demodulation of digital modulation signals. The locking phase angle of an ILO follows a similar sigmoidal shape found in neurons. An equivalent SAW ILO neuron circuit is presented and further developed into a self organized neural network. The SAW-based ILOs are then modified by controlling the quality factor of the SAW feedback element to produce carrier recovery, analog to digital converters and data multiplexer circuits. A very non-linear, near-chaotic ILO is introduced and examined with the aid of the Duffing equation. The Duffing model accurately verifies a periodic pulse

generator employing a driven unlocked SAW ILO.

A crucial component in any communication receiver is a "front-end" filter that eliminates any interfering frequencies that are close-in to the receiver channel. A study of such a component reveals that a dual-mode leaky-SAW resonator filter is ideal for the task. Antenna theory is applied to model the radiation conductance of thick-film interdigital transducers (IDTs) in dual mode wideband leaky-SAW resonator-filters on 64° Y-X $LiNbO_3$ employing a three-IDT structure. As well. SAW coupling-of-modes reflection-grating equations and IDT S-parameters are modified to cater for increased leaky-SAW attenuation above the Bragg frequency. Theoretical frequency response computations are in excellent agreement with experimental results obtained for several low-loss 85-MHz structures fabricated with metallization film thickness ratios (h/λ) of up to 3 %.

ACKNOWLEDGEMENTS

First and foremost I would once again like to express my gratitude to Dr. C. K. Campbell for his patience, guidance and generosity that he has given me for the past twenty two years as employer, supervisor and friend.

I have to give special thanks to my wife Marlene Horning for putting up with me during this process. I once again fallaciously promise that this is the last project that I will attempt.

TABLE OF CONTENTS

APPENDICES

LIST OF FIGURES

CHAPTER 1

INTRODUCTION

1.1 Motivation for the Study of SAW Devices

The increasing use of wireless communications to transmit both voice and data has increased dramatically during the 1990s. This area of information transfer is commonly referred to as the Personal Communication Service (PCS). The frequency spectrum allocated for both voice and data transmission is mostly in the ultra-high frequency (UHF) band of about 800 to 900 MHz for North America. The Europeans though, have also allocated data transmission in the 400 to 450 MHz region . Other countries have adapted a combination of frequency usage depending on the specific licensing agreements [1].

Transceivers being designed for this emerging PCS market must be small, light weight, rugged, have low power consumption and be able to cope with operating temperature differentials of about -25°C to +50°C. Another critical parameter in the design, is the height that the component may have. With laptop and handheld personal digital assistants (PDAs) being popular in the mobile data market, the transceiver must fit within a Type II personal computer memory card international association (PCMCIA) slot. This opening allows for a total of only 5 millimetres in thickness, that must include both the mounting board and components [2].

One well established area of thin-film planar electronics that is adapting to this demand is the surface acoustic wave (SAW) technology. SAW devices are particulary effective in creating, conditioning and processing radio frequency (RF) signals [2]-[3]. Their advantages are that they are of simple thin-film construction, small in size and rugged.

Several areas that SAW devices have excelled in are:

i) Oscillators for the generation of very-high frequency (VHF) and UHF signals with excellent stability characteristics. These oscillators may be modified into a two- port device with an injected input signal [4].

ii) Bandpass filters for front-end receivers in the VHF and UHF regions. These components can have a total cascaded insertion loss (IL) of about 3.5 dB and approximately a 3-4 % bandwidth [5].

iii) VHF-UHF signal processing with applications as convolvers, correlators, Fourier transformers and chirp filters [3].

1.2 Objectives

The main objective in writing this thesis is to demonstrate the intense effect that the coupling-of-modes (COM) phenomena has had on SAW devices and their application to novel circuitry. This thesis is divided into two parts. The first concentrates on the

various applications that can be realized by a SAW-based injection-locked oscillator (ILO). The degree of coupling between the injected signal and the oscillator and the characteristics of the SAW within the oscillator loop produce diverse effects. The second part investigates a dual-mode leaky-SAW in-line coupled resonator filter design.

A short treatise on the fundamentals of acoustic waves is given in Chapter 2. The three types of acoustic waves implemented within this thesis are the surface-wave, surface-transverse-wave and the leaky-SAW. Part 1 describes the COM studies of SAW oscillators that are divided into three chapters. The background and the development of the COM equations are removed from the main text and designated to Appendix B. Chapter 3 describes SAW injection-locked oscillators. For this case the oscillator can track the very small injected signal and behaves similarly to a phase-lock-loop (PLL) tracking the reference crystal. The uniqueness of this chapter is the application of an injection-locked oscillator neuron (ILON). Not all ILOs have to be completely locked to be effective, and Chapter 4 investigates SAW oscillators in the vicinity of injection-locking. Finally for Part 1, Chapter 5 examines a non-linear dynamical system based on a SAW ILO.

In Part II of this thesis a low-loss SAW resonator-filter is introduced. A design using a modified COM technique, for a dual-mode leaky-SAW resonator is described in Chapter 6. Antenna theory is applied to model the radiation conductance of the thick-film interdigital transducers (IDTs). The COM reflection-grating equations and the IDT S-parameters are modified to cater for the increased leaky-SAW attenuation above the Bragg frequency.

A short segment containing a summary and conclusions completes Chapter 7. The Appendices include sections on, a) fabrication of devices, b) coupling-of-modes derivation and in sections c,d,e and f, recent publications of this author and g) a short synopsis on the basics of surface acoustic waves and piezoelectricity.

CHAPTER 2

FUNDAMENTALS OF SAW AND PSEUDO-SAW ACOUSTIC WAVE DEVICES

2.1 Introduction to SAW Devices

Surface acoustic wave (SAW) propagation at the free surface of a homogeneous isotropic elastic solid was first introduced by Lord Rayleigh in London, England in 1885 [3]. These surface waves that are also named the Rayleigh wave phenomenon, are the waves present on or near the surface of the earth during earthquakes. The mining and oil companies also take advantage of these waves by using seismographic recording techniques for resource exploration purposes.

The electronic industry finally discovered SAW propagation on crystals in 1965, with the invention of the interdigital transducer (IDT) by White and Voltmer [6]. The IDT is used as an efficient technique for the generation and detection of surface waves on a piezoelectric substrate's surface.

2.2 The Structure of Surface Acoustic Wave Devices

A surface acoustic wave device in its simplest form can be modelled as a device that performs:

i) An electrical-to-mechanical transformation via an interaction of the electromagnetic fields of the IDT with the piezoelectric crystal. This phenomena would occur at the input IDT.

ii) A propagation of the acoustic wave in a specific direction that is a function of the crystal cut and IDT placement.

iii) A mechanical-to-electrical transformation opposite to item (i), occurring at the output IDT.

The input and output IDTs can both be thought of as resembling electromagnetic transmitting and receiving antennas. From reciprocity concepts, a voltage signal can be applied to either IDT with the same end result. A preliminary illustration of a surface acoustic wave motion initialized by a set of IDTs, on a piezoelectric substrate, is shown in Fig. 2.1.

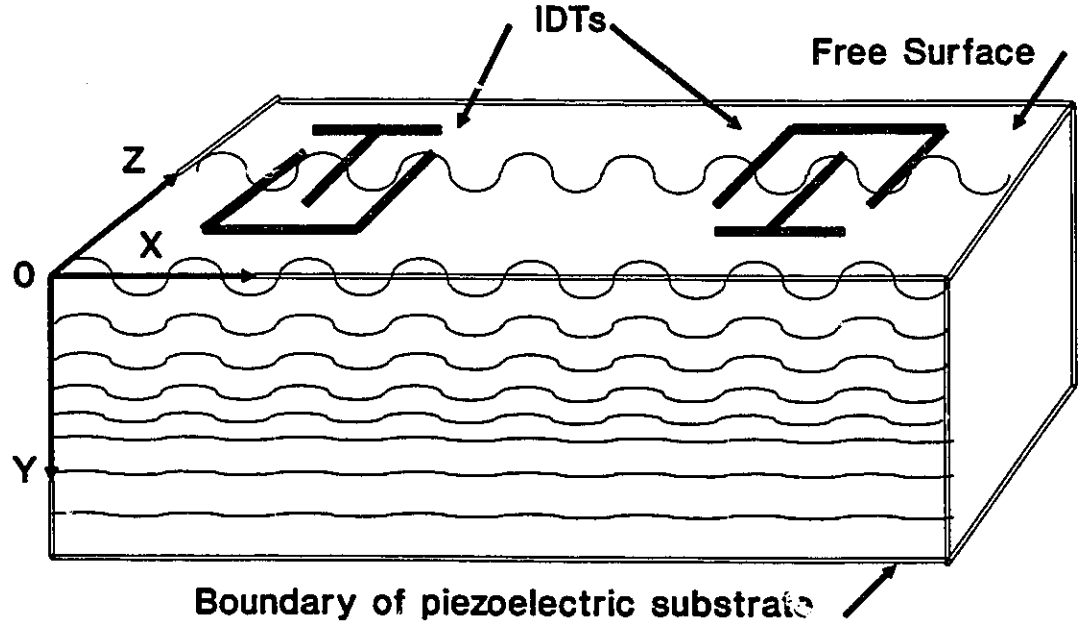

Figure 2.1 The wave motion both on the surface and within a piezoelectric substrate. The IDTs excite the acoustic wave which in this case propagates along the X axis.

A more detailed description of Fig. 2.1, would illustrate that on a solid, a surface wave may be regarded as a disturbance involving deformations of the surface of the solid. These deformations are a result of the electric field components (both parallel and normal to the IDT) interaction with the piezoelectric substrate. The distortion of the surface is caused by the motion and displacement of the atoms within the lattice structure of the solid. These deformations taper off quickly as the depth increases. For ideal elastic solids, there are internal restoring forces that tend to restore the surface of the solid to its equilibrium position.

An acoustic wave can be resolved into two basic components;

1) Longitudinal waves - where the atoms vibrate in the propagation direction, ie. the X axis of Fig. 2.1.

2) Shear waves - where the atoms vibrate in the (Y,Z) plane of Fig. 2.1.

2.3 Properties of SAW Devices

The acoustic wave does not necessarily have to travel on the surface of the device for the device to perform as a resonator or a filter. Several variations of acoustic wave devices include the surface wave (SAW), shallow bulk acoustic wave (SBAW) [3]. The main difference between a SAW and SBAW is the propagation of longitudinal bulk waves with shear horizontal (SH) polarization rather than the elliptically polarized SAW. The SH waves also utilize the IDT for their excitation, with the exception that the SH waves are excited only by the parallel electric field component of the IDT. Figure 2.2 is a

pictorial simplification, to illustrate the difference in propagation characteristics within a piezoelectric substrate for various acoustic waves. For SAW propagation shown in Fig. 2.2 (a), the amplitude of the surface displacement along the Y axis is larger than that along the X axis, (see Fig. 2.1 for axis reference). This results in a mechanically time dependent elliptical displacement of the solid surface. The first type of SBAW wave studied is the surface skimming bulk wave (SSBW) propagation within a crystal, as shown in Fig. 2.2 (b). This particular wave propagates below the surface, with the wave either dissipating within the crystal or re-converting to a bulk mode. The real usefulness of a SSBW wave can be obtained by the use of an energy-trapping grating structure placed on the surface as illustrated in Fig. 2.2 (c). This propagation mode is referred to as a surface transverse wave (STW). STW devices usually have several advantages over their SAW counter-parts. They have higher velocities, allowing a higher achievable frequency for the same IDT layout. Since the wave travels just below the surface, any surface contamination (excluding the IDTs) will not greatly alter the device's characteristics. The STW can also exhibit superior temperature coefficients, operate at higher powers and yield good suppression of spurious modes with respect to SAW. A relatively new propagating mode utilizing a another type of SBAW is the leaky-SAW shown in Fig. 2.2 (d). These waves propagate within the crystal in a similar fashion to an STW with the exception that above the reflection stopband the waves tend to propagate downwards towards the lower surface boundaries [7]. The efficient coupling between the IDT and the leaky-SAW provides good, low insertion loss devices.

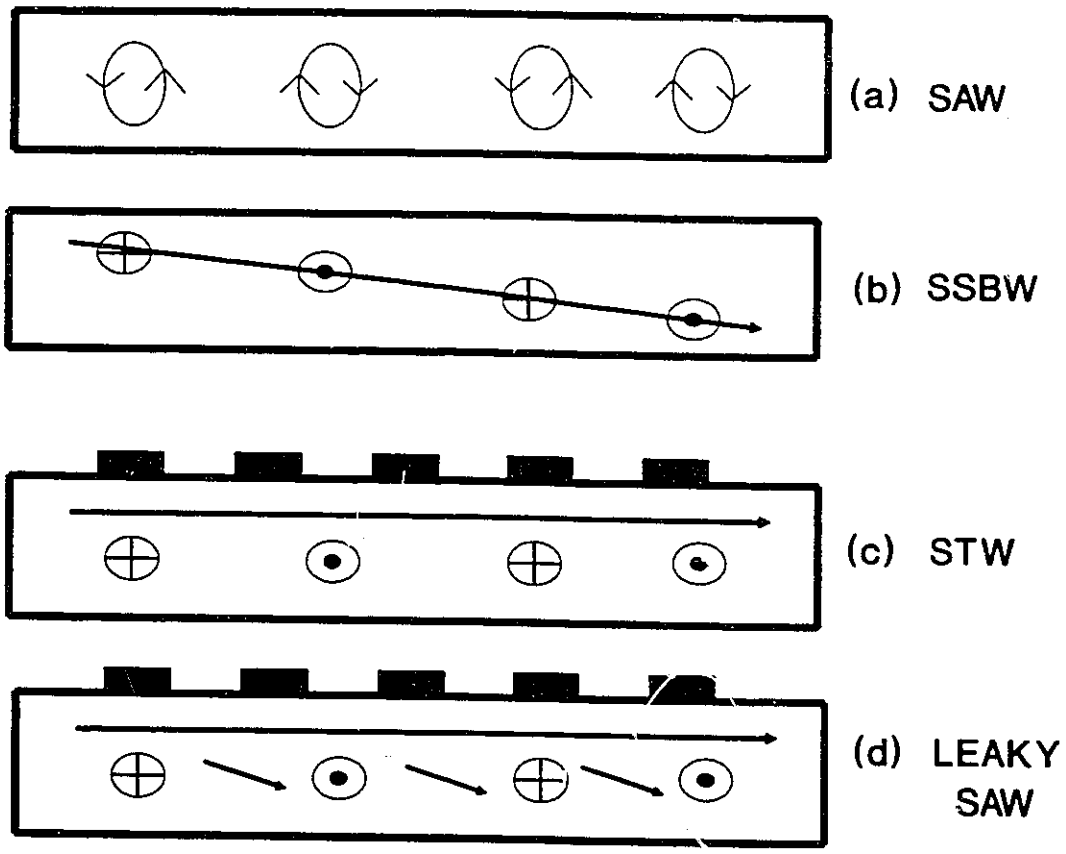

Figure 2.2 Propagation characteristics for different propagating waves; (a) surface acoustic wave, (b) surface skimming bulk wave, (c) surface transverse wave and (d) leaky-SAW.

2.4 Basic SAW Delay Line

The main element of SAW devices is the IDT structure. The electrical RF input signal is converted to an acoustic waveform by the piezoelectric effect. The structure of the IDT determines the impedance and frequency response of the SAW device.

A simple SAW delay line shown in Fig. 2.3, will operate at a nominal centre frequency of f_c . Its 4% bandwidth of operation is a function of the number of finger pairs N_p of the input IDT.

$$BW_{4\%} \simeq \frac{f_o}{N_p} \tag{2.1}$$

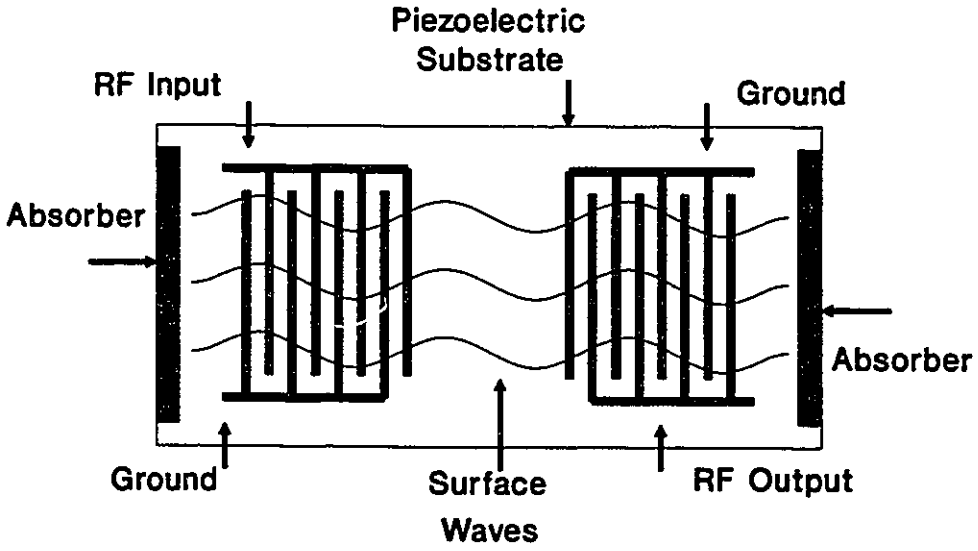

Figure 2.3 Basic SAW delay line.

Each metal electrode finger is normally a quarter wavelength in width and separated by a space of a quarter wavelength.

The total phase shift will be determined by $e^{(-j\beta d)}$, where d is the distance between the centres of the input and output IDTs. With uniform geometry of both the input and output IDTs, the phase shift ($-\beta d$) will be a linear function of frequency. Deviations from this linearity will depend on second-order perturbations within the SAW device that are described in more detail in [8]. The absorber on either end of the crystal prevents the surface wave from reflecting back from the edges and helps diminish some of the second-order effects.

The IDT can be modeled by the equivalent circuit of Fig. 2.4. A transducer consisting of N_A electrode finger pairs, produces circuit elements, of total static capacitance C_T,

$$C_T = N_A \cdot C_s \qquad (2.2)$$

with conductance G_a,

$$G_a = 8 \cdot N_a^2 \cdot G_o \cdot [\frac{\sin(x)}{x}]^2 , \qquad (2.3)$$

with the susceptance B_a given by

$$B_a = 8 \cdot N_a^2 \cdot G_o \cdot [\frac{\sin((2x) - 2x)}{2x^2}] , \qquad (2.4)$$

where

$$G_o = K^2 \cdot C_s \cdot f_c \qquad (2.5)$$

and

$$x = \pi \cdot [f - f_c] \cdot \frac{N_A}{f_c} . \qquad (2.6)$$

In the above, λ_c = wavelength at the IDTs centre frequency f_c, K^2 = piezoelectric coupling coefficient of the substrate, f = frequency and v_c = acoustic velocity under the IDT and C_s = the static capacitance of one periodic section.

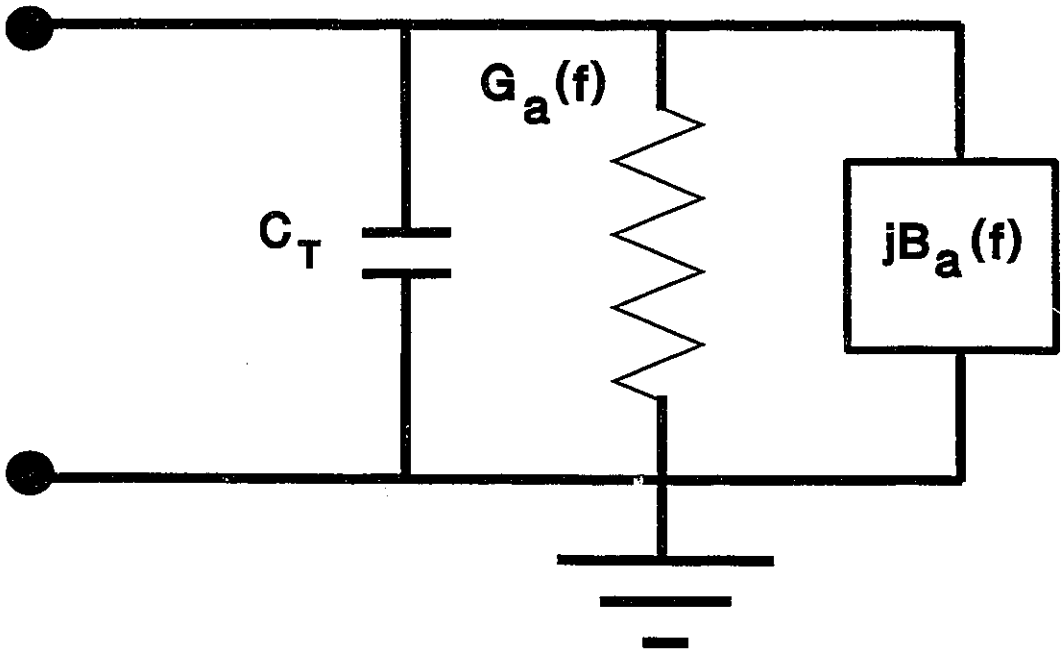

Figure 2.4 Equivalent circuit of an IDT.

Figure 2.5 illustrates the IDT conductance $G_a(f)$ and Hilbert transform susceptance $B_a(f)$ of an IDT centred at 930 MHz [9].

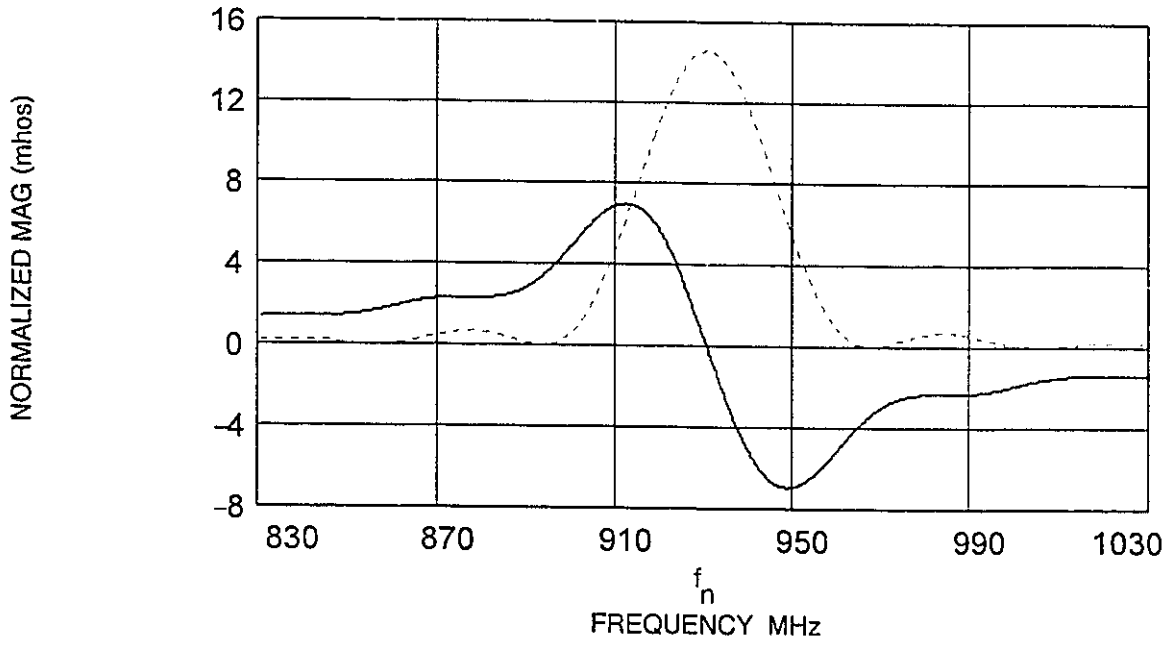

Figure 2.5 Theoretical conductance (dotted line) and susceptance (solid line) for a SAW IDT centred at 930 MHz.

The frequency response of the previous Fig. 2.3 with 60 finger pairs per IDT centred at a normalized frequency of 500 Hz is shown in Fig. 2.6. The frequency response of a simple delay line SAW device is the equivalent of the Fourier transform of the uniform IDT structures with N_A sample points [2] .

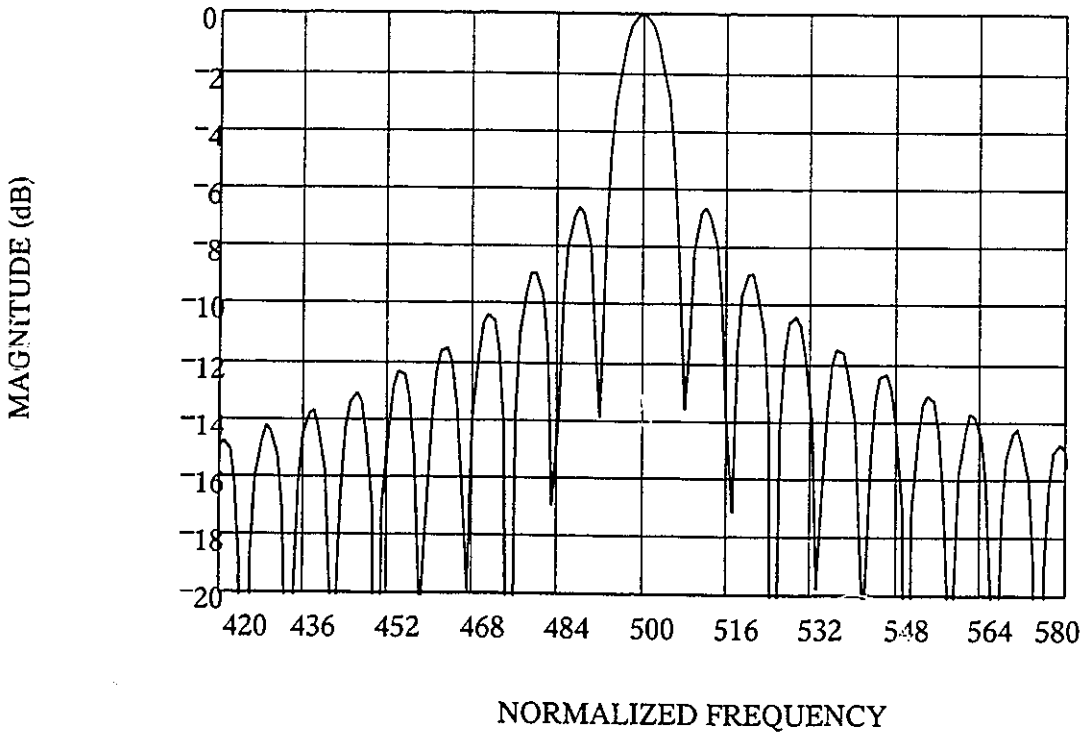

Figure 2.6 Frequency response of an illustrative SAW IDT.

2.5 Quality Factor of SAW Filters

A useful property of a SAW filter is the quality factor or Q. For a tuned circuit the quality factor Q is

$$Q = \frac{\omega_c}{2 \cdot B'} \qquad (2.7)$$

where $\omega_c = 2\pi f_c$ is the centre frequency and B' is the half bandwidth in rad/sec of the circuit between the 3-dB points. The Q may also be expressed for SAW devices, in terms

of the group delay time, $\tau_g = -d\Phi/d\omega$. For the delay line discussed so far this delay would also equate to the approximate time the acoustic wave takes to travel the centre-to-centre distance between the IDTs. The Q can then be expressed as

$$Q_e = \frac{\omega_c \tau_g}{2} . \qquad (2.8)$$

This Q is often called the effective Q_e , since the SAW device involves energy transfer rather than energy storage.

For applications involving the need for a higher Q_e , a SAW resonator structure could be utilized. Figure 2.7 illustrates a typical two-port SAW resonator (SAWR). The physical difference is in the reflective grating structures on either sides of the IDTs. These gratings have the properties of a distributed feedback (DFB) structure [10], which in effect increases the delay time τ_g a signal remains in the cavity. The distances d_g and d_t are important in the design of the desired frequency response.

To put in perspective the size of the device in Fig 2.7, the width of each dark strip (finger) and space is usually $\lambda_o/4$ each , where the acoustic wavelength $\lambda_o = v/f$. The velocity v can vary between 3300 m/s to 4700 m/s depending on the substrate material used. A 100 MHz SAWR device, [3], on YZ-lithium niobate (v = 3488 m/s) would then have 10 strips per IDT and 564 reflector strips at each end. The $\lambda_o/4$ distance would be about 8.72 microns, to give an overall dimension of 10 mm in length and a width of 1.5 mm, using the aperture (finger overlap) width of 40 λ_o with about 4 λ_o gap at the finger ends. The distances d_g and d_t would be typically be $\lambda_o/4$ and $10\lambda_o$ respectively.

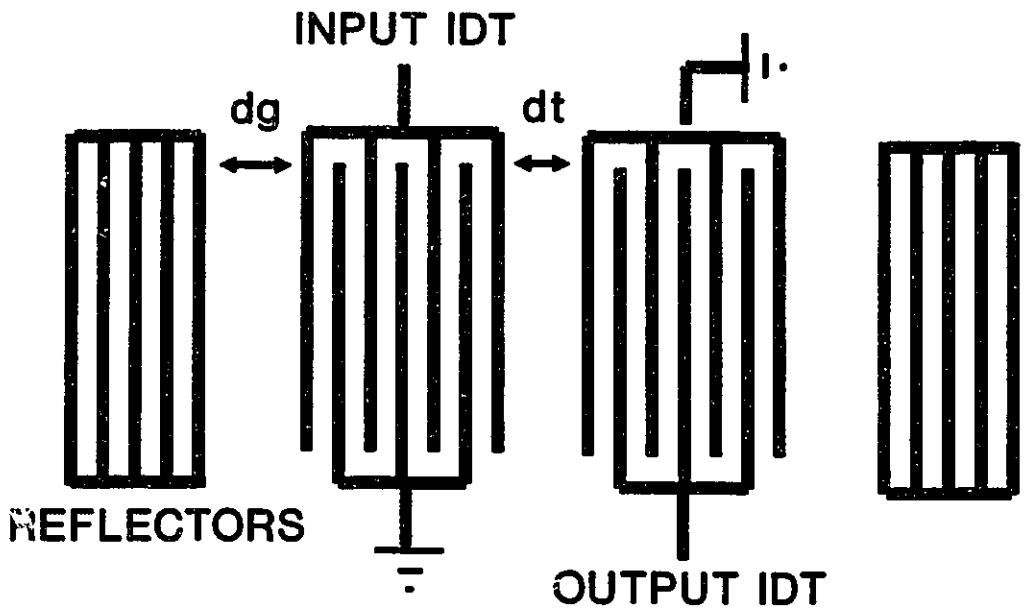

Figure 2.7 A SAW resonator with end gratings as reflectors.

2.6 SAW Applications in the Coupling-of-Waves Studies

In this thesis, the first applications involving coupling-of-modes, will relate to SAWR filters as the feedback element in modified oscillator circuits, found in Part 1. In these oscillators an injected signal is coupled into the loop as shown in Fig. 2.8. The function of these circuits depends on the quality factor of the SAWR within the feedback path and the amount of injected signal allowed to couple to the oscillator circuit.

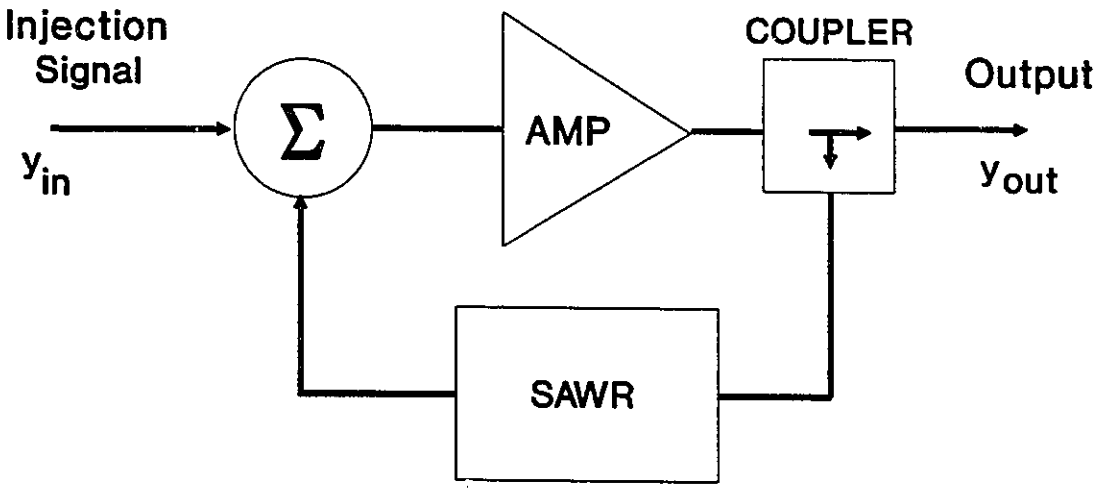

Figure 2.8 Injected oscillator with a SAWR as the feedback element.

The operation of the circuit of Fig. 2.8, which will be studied in Part 1 of this thesis, will be governed by three different conditions,

1) The Q of the SAWR is low enough and the coupled injected signal is sufficient to lock the oscillator. The results are that this circuit can behave as an amplifier or as a modified neuron within a neural network. Chapter 3 will elaborate on these ideas.

2) The Q of the SAW device is high enough and the coupled injected signal is only sufficient to keep the oscillator in the vicinity of lock-in. Chapter 4 will discuss the utilizations of this configuration that include a carrier-recovery scheme for a digital modulated signal, an analog-to-digital converter operational at 915 MHz, and a data multiplexer.

3) The loop amplifier operates in the non-linear region. The injected signal is adjusted to keep the oscillator in the vicinity of lock-in. The output of the oscillator y_{out}, is fed into another non-linear amplifier. This produces a pulse output which is a twin-well dynamical system that will be analyzed in chapter 5 by chaotic analytical methods.

The second application discussed in Part 2, chapter 6 of this thesis is the coupling effects within a dual-mode wideband leaky-SAW resonator-filter on 64^{o} Y-X lithium niobate (64^{o} Y-X $LiNbO_3$) employing a three-IDT structure illustrated in Fig. 2.9 [11].

The novelty of this filter arises from two design parameters: the gap distance, d_t, separating the IDTs as well as the choice of substrate. The gap between the single input and dual output IDTs is chosen for optimum coupling between the two modes, while the distance $d_t = 0$. This can be accomplished by allowing the grounded portions of the IDT finger arrays to touch. The choice of a leaky-SAW substrate enhances the filter's characteristics by reducing the sidelobes above the grating stopband.

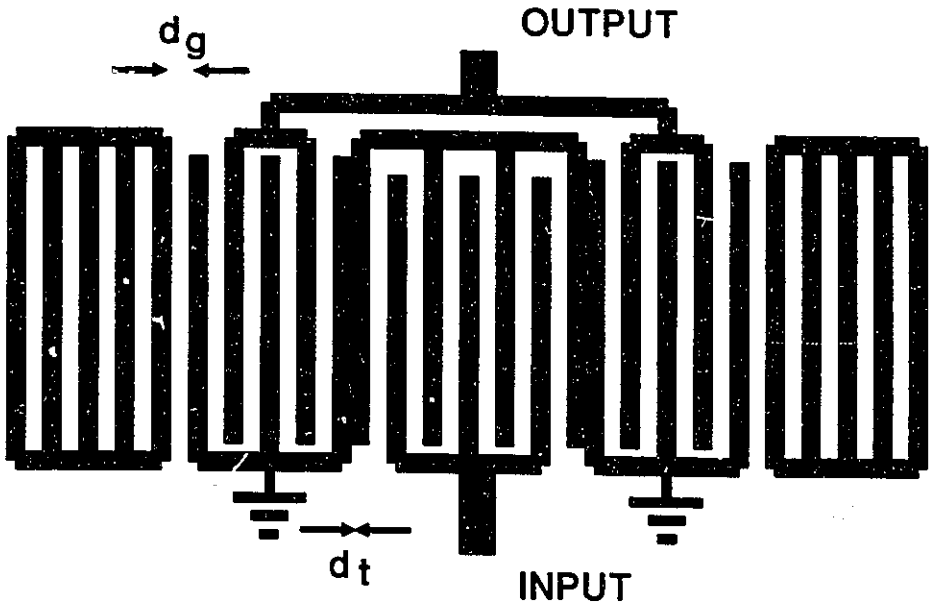

Figure 2.9 The finger geometry of a three IDT dual-mode leaky-SAW structure with shorted reflectors.

A complete description on the fabrication process for SAW devices at McMaster University is included in Appendix A. The section contains an explanation of the substrate preparation, metal deposition, mask photolithography and the final etching of the circuits.

PART I

COUPLING-OF-MODES STUDIES OF SAW OSCILLATORS

CHAPTER 3

SAW INJECTION-LOCKED OSCILLATORS

3.1 Introduction

Surface acoustic wave resonators are normally high Q (>1000) devices which can be fabricated to close frequency tolerances, to provide very accurate filters. Since their introduction to the electronic industry over twenty years ago [12], they have been developed to provide unsurpassed performance in the ultra-high-frequency (UHF) range. Oscillators employing these filters in their feedback path, routinely exhibit single-sideband phase noise of less than -180 dBc/Hz at 100 kHz offset, and aging frequency drifts of less than 1 ppm/yr [13]. Surface transverse wave resonators are very similar to their SAWR counterparts, but provide a lower Q (>100).

If a signal of appropriate frequency and power is injected into a free-running oscillator, the latter will track it. This phenomenon, known as injection-locking, was first studied by van der Pol [14] and subsequently by Adler [15]. Since these early investigations, circuits employing injection-locked oscillators (ILO) have performed a wide range of functions including amplification, phase-shifting, carrier recovery, frequency multiplication and signal modulation and demodulation [16].

While injection-locking is often used at optical frequencies [17], it has not often been used at UHF frequencies, due to the difficultly in fabricating stable inductor and capacitor (LC) resonant tank circuits. The purpose of this chapter is to study, using the

coupling-of-modes (COM) method, the effects of a SAWR oscillator locking to an injected signal. The applications section of this chapter will show that SAWR oscillators can provide a cost-effective approach with a number of advantages over conventional methods of electronic communication and neural network circuits.

3.2 Theory of Injection-Locking Using COM

The *coupling-of-mode* equations are fundamentally an analysis of a resonant system being perturbed by a weak external stimulus. A short derivation of the COM formulism of an LC circuit is described in Appendix B. Equations (B.5a and b) will serve as a good starting point for this particular development and have been expanded within the brackets and reintroduced as

$$\frac{da_+}{dt} = j\omega_o\, a_+ \qquad (3.1a)$$

$$\frac{da_-}{dt} = -j\omega_o\, a_- \,, \qquad (3.1b)$$

where a_+ is the *positive-frequency component* of the mode amplitude and ω_0 = free running angular frequency. The resonant mode is fully described by eqn (3.1a) alone, since eqn (3.1b) is the complex conjugate of eqn (3.1a).

Since a SAW component will be used as the feedback element in this system, a loss factor associated with the insertion loss (IL) of the SAW device is introduced. If the insertion loss can be considered small, then the introduction of a SAW into the mode amplitude equation of (3.1a), with the complex conjugate term now ignored, is

$$\frac{da}{dt} = j\omega_o\, a - \frac{1}{\tau_o}\, a \,, \tag{3.2}$$

where $1/\tau_o$ is the decay rate due to the insertion loss of the SAW .

The decay rate is further enhanced if the external output load power is also considered as a loss. In this case the mode amplitude with both internal ($1/\tau_o$) and external ($1/\tau_e$) loss components included is

$$\frac{da}{dt} = j\omega_o\, a - (\frac{1}{\tau_o} + \frac{1}{\tau_e})\, a \,. \tag{3.3}$$

The schematic of an injected oscillator is shown in Appendix D, Fig. 1, [18], and contains three main features. The first is the external injected forward signal S_+ travelling towards the oscillator. The second is a transmission line connecting the external signal to the oscillator. Finally, a reflected signal S_- that will travel back down the transmission line to the external signal. This configuration lends itself to transmission line theory, as a reflection coefficient will result due to the mismatch of circuit parameters such as frequencies and quality factors (Q) of the injecting source and oscillator.

The COM equation for a SAW based injected oscillator with an unloaded quality factor, $Q_0 = (\omega_0 \tau_0)/2$ and sufficient amplifier gain medium, for which the oscillator mode amplitude is, from reference [10]

$$\frac{da}{dt} = a \cdot \left(j\omega_0 - \frac{1}{\tau_0} - \frac{1}{\tau_e} + \frac{1}{\tau_g} \right) + \sqrt{\frac{2}{\tau_i}} S_+ \qquad (3.4)$$

Here $1/\tau_g$ = rate of growth of the mode amplitude due to the gain of the amplifier within the oscillator and S_+ = injected wave mode amplitude at angular frequency ω_i with a rate of growth of $1/\tau_i$. The coefficient $(2/\tau_i)^{1/2}$ is actually the coupling factor $\varkappa$ of the injected signal into the oscillator. This circuit will oscillate in the steady state at ω_0 with no driving source S_+, provided $1/\tau_g = 1/\tau_0 + 1/\tau_e$.

The above COM equation can explain how a smaller amplitude and injected signal from a higher Q source, can influence and control a much larger amplitude and lower Q, oscillator signal. Fig. 3.1 illustrates two signals. In the first $1/\tau_g \neq 1/\tau_0 + 1/\tau_e$, and the signal decays as the SAW feedback element has too much loss. The other waveform is derived directly from eqn (3.4) and illustrates how a smaller injected signal, when added to the first waveform, now satisfies the condition $da/dt = j\omega_0 a + (2/\tau_i)^{1/2}$ and the output of the oscillator will track and follow the injected signal. Note that there will be a small frequency change when $\omega_i \neq \omega_0$.

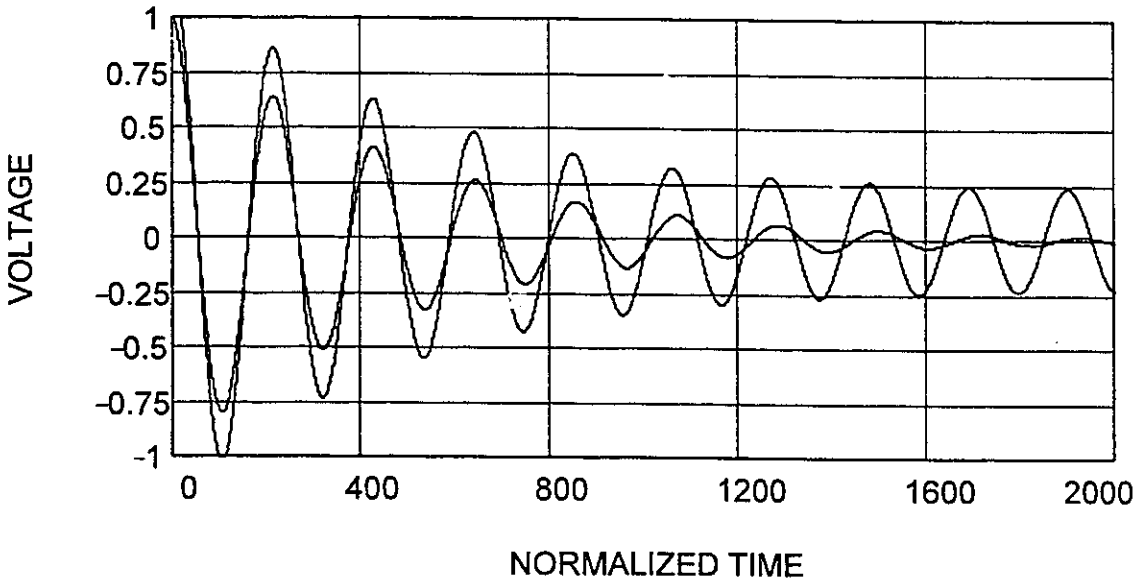

Figure 3.1 Voltage-versus-time diagram of the COM equation for an ILO. The higher Q signal will have the larger amplitude after a finite time. The oscillator loop will track this signal.

3.3 Analysis of an ILO Circuit

The equations governing the stationary phase angle α_{sp} between oscillator and injected signals in an injection-locked oscillator (ILO) employing a tuned-circuit feedback element are given as [15],[19],[20],

$$\sin(\alpha_{sp}) = 2Q \cdot \frac{E_{osc}}{E_{inj}} \cdot \frac{\Delta\omega_0}{\omega_0} \quad , \tag{3.5}$$

for $+90° \leq \alpha_{sp} \leq -90°$, where Q = tuned resonator circuit quality factor, E_{osc} = oscillator voltage, E_{inj} = injection signal voltage, ω_0 = "free-running" frequency, and locking

bandwidth $\Delta\omega_0 = (\omega_0 - \omega_i)$, where ω_i = injection signal frequency. The locking-bandwidth range is given in terms of lock parameter K

$$K = 2Q \cdot \frac{E_{osc}}{E_{inj}} \cdot \frac{\Delta\omega_0}{\omega_0} = \frac{\Delta\omega_0}{B} \quad , \tag{3.6}$$

where $|K| < 1$ for synchronization lock.

For the simple injected oscillator shown previously in Fig. 2.8, if the conditions for the locking parameter $|K| < 1$ are met, then y_{out} will follow the input frequency and eventually lock to it. Fig. 3.2 illustrates the locking process of an ILO as described 3-dimensionally with the parameters E_{inj} and time forming the horizontal plane and amplitude along the vertical axis. The left side of the plot shows initially only the unperturbed oscillator output waveform at ω_0, then the composite waveform consisting of ω_i, ω_0 and $\Delta\omega_0$. The right side of the figure shows how the locked oscillator has but a single frequency, ω_i.

The phase function $\alpha(t)$ of eqn (3.7) describes the synchronization of the two frequencies within the ILO. This function will have either a positive or negative slope depending if the injection frequency is higher or lower than the free-running oscillator frequency.

$$\alpha(t) = 2\arctan\left[\frac{1}{K} + \frac{\sqrt{K^2 - 1}}{K} \tan\left(B \frac{(t - t_0)}{2} \sqrt{K^2 - 1}\right)\right] \quad . \tag{3.7}$$

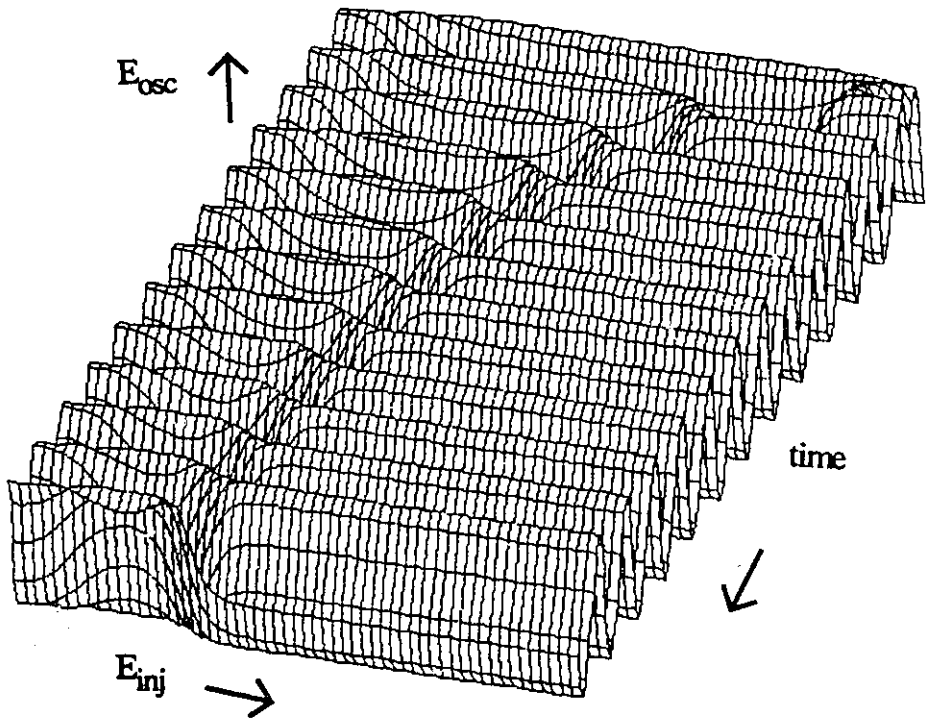

Figure 3.2 3-D plot of the locking process as functions of E_{inj} and time. The parameters E_{inj} form the horizontal axis and the time axis is coming out of the page. Amplitude is on the vertical axes.

This phase function is similar to the sigmoidal function found in the error voltage of a phase-lock-loop (PLL). In fact, the nonlinear equations describing an ILO (eqns 3.5, 3.6 and 3.7) are identical to those for a PLL [21].

Shown below is Fig. 3.3 that illustrates a typical response calculation for $\alpha(t)$ as a function of time.

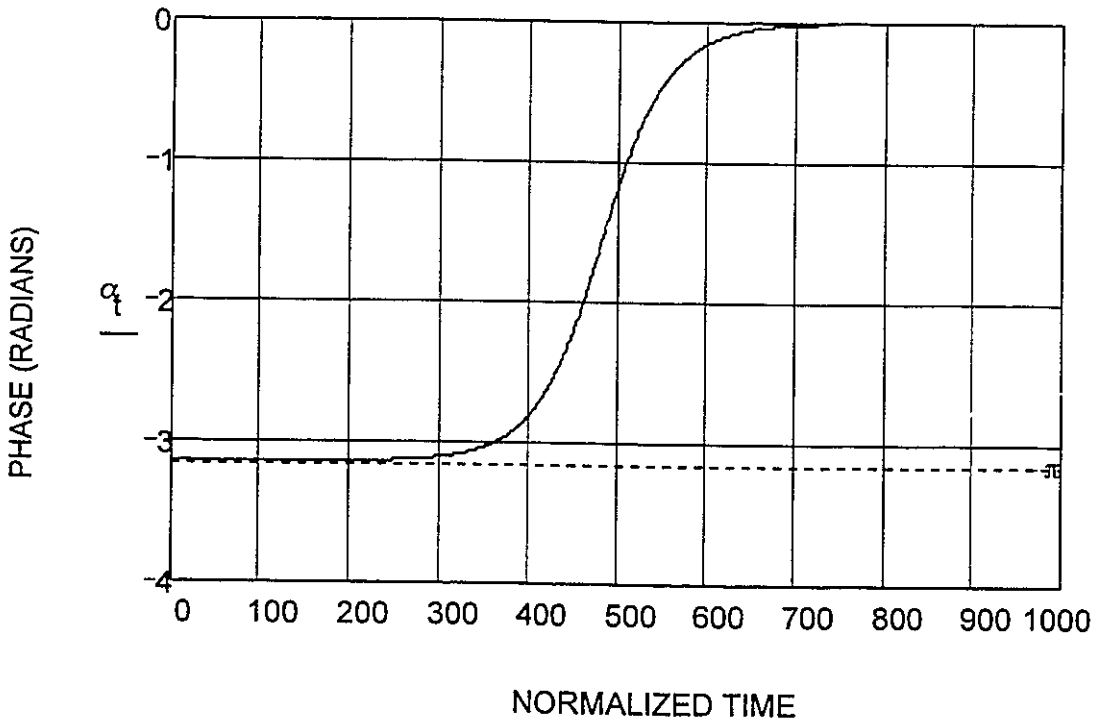

Figure 3.3 Phase component $\alpha(t)$ when the injecting frequency is greater than the oscillator frequency.

3.4 Circuit Applications

A common utilization of an ILO, is to stabilize a high output power, low Q oscillator with a much smaller injected continuous wave (CW) signal from a higher Q source. An advantage of this configuration is that the output signal now adapts to the improved phase-noise characteristics of the injected signal [22].

The concept of an ILO tracking, and eventually adapting to the injected signal's attributes was extended to include a number of injected signals. For signals that exhibit frequency hopping traits, studies were performed, in the mid to late 1980's on the lock-in characteristics, using SAW multimode devices [23], [24]. Later within that time frame ILO's were also implemented with STW resonators and used for the amplification of very weak frequency modulated signals [25]-[28]. Once these signals were detected it was discovered that an ILO could also demodulate directly from input RF to baseband in one process [25]-[27]. This circuit therefore eliminates any need for costly intermediate-frequency (IF) stages.

The following sections will illustrate several applications of ILO's with coupled signals.

3.4.1 Amplification Using an ILO

This section presents the use of a 1012-MHz STW resonator-based oscillator for low-noise amplification of 2-Mb/s binary phase-shift-keyed (BPSK) signals. Experimental results showed that the oscillator maintained about 0-dBm output power if the injected BPSK was varied from -40 dBm to +20 dBm with little or no distortion present. A further

test of this amplifier showed that a bit error rate (BER) of 10^{-10} was achieved for an input carrier to noise ratio (C/N) of about 12.5 dB. A complete copy of reference [29] appears in Appendix E to further describe the results.

3.4.2 Demodulation Using an ILO

A frequency-shift-keyed (FSK) system is a digital FM system in which the transmitted signal is given by

$$s(t) = A \sin (2\pi \cdot (f_o + b_i \Delta f) \cdot t) \quad . \qquad (3.8)$$

The transmitted frequency will either be $f_1 = f_o + \Delta f$ or $f_2 = f_o - \Delta f$, depending on the polarity of the binary data bit b_i (-1 or +1).

Minimum-shift keying (MSK) is a member of a group of modulation systems called continuous-phase modulation (CPM) [30]. The phase of a MSK signal is a continuous function of time and has a constant envelope [31]. This results in a spectrum whose envelope decays as the inverse fourth-power of frequency, as compared to conventional discontinuous phase modulation schemes where the spectrum decays as the inverse-square of frequency. A further consequence of MSK is that memory is introduced into the modulation, and a receiver can make more robust decisions than one that makes independent symbol by symbol decisions [32].

The MSK scheme imposes the condition shown in the following equation

$$\Delta f = \frac{1}{4T} \quad , \qquad (3.9)$$

on the frequency deviation Δf, where T is the chip period. This results in a signal with

four phase states, namely (0, $\pi/2$, π, and $3\pi/2$) at the sampling instances.

The demodulator is shown in Fig. 3.4, where the front-end section is an ILO amplifier with about a 63-dB dynamic range. The demodulator follows the amplifier, and the signal splits into two paths. One is directly fed into the mixer's LO port via a fixed phase shifter. The mixer will act as a phase detector and the fixed phase shifter will adjust the voltage swing of the output data. The other path connects the signal to the RF port of the mixer via the STW device. The phase slope of the STW resonator is very steep, (0.1^{o}/kHz), in the region of f_o. The two frequencies f_1 and f_2 will produce two different phase values to the mixer port. The IF port of the mixer will therefore produce baseband-demodulated data bits as two different voltages produced by the phase difference. This method eliminates the need of down-conversion found in most traditional intermediate frequency (IF) stages.

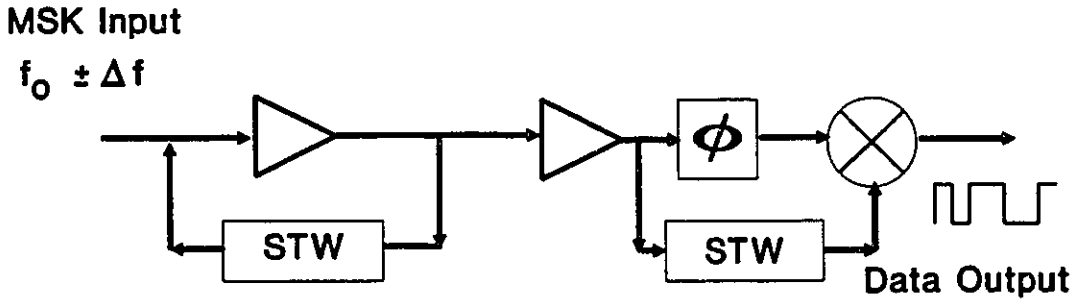

Figure 3.4 Circuit schematic of a SAW demodulator without any down conversion.

In experiments conducted by the author, it was found that this demodulator was capable of handling a very broad range of data rates for a given input power. Figure 3.5 illustrates the bits per second (bps) versus injected power. At the low end the circuit demodulated 400 bps at -60-dBm and at the upper end 280 kbps at -35-dBm input power [26], [27].

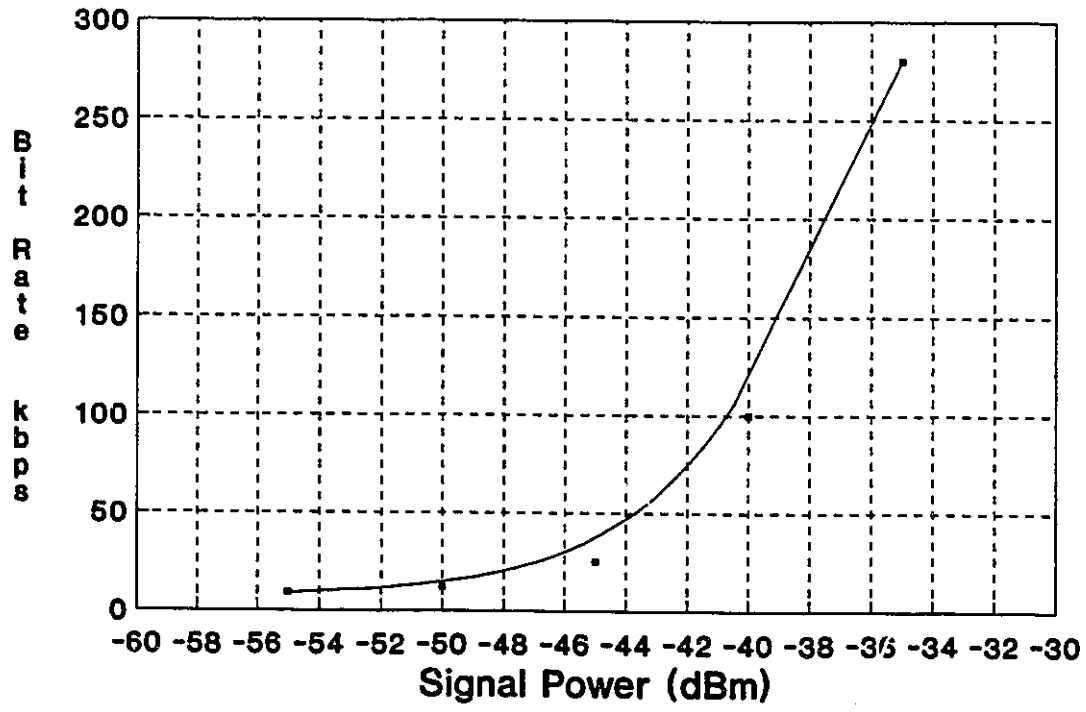

Figure 3.5 Approximate curve through measured data points illustrating bit-rate versus injected input power.

3.4.3 An Equivalent Neuron Circuit

The use of an acoustic wave injected-locked oscillator neuron (ILON) model is presented. These ILONs have a high dynamic range while requiring fewer components and operate at a higher frequency than voltage controlled oscillator neurons (VCONs) used in the Hoppensteadt models [33].

Both software and hardware artificial-neural networks (ANNs) can be used to model sets of neurons, consisting of axons feeding dendrites through synapses, as symbolized in Fig. 3.6. The operation of such networks is highly parallel, with each network element performing independently. In these, the ANN is structured as a set of simple network elements each of which is an essentially-independent processor, in terms of nodes and links. Paths between neurons, consisting of axons feeding dendrites through synapses, are modelled by ANN links.

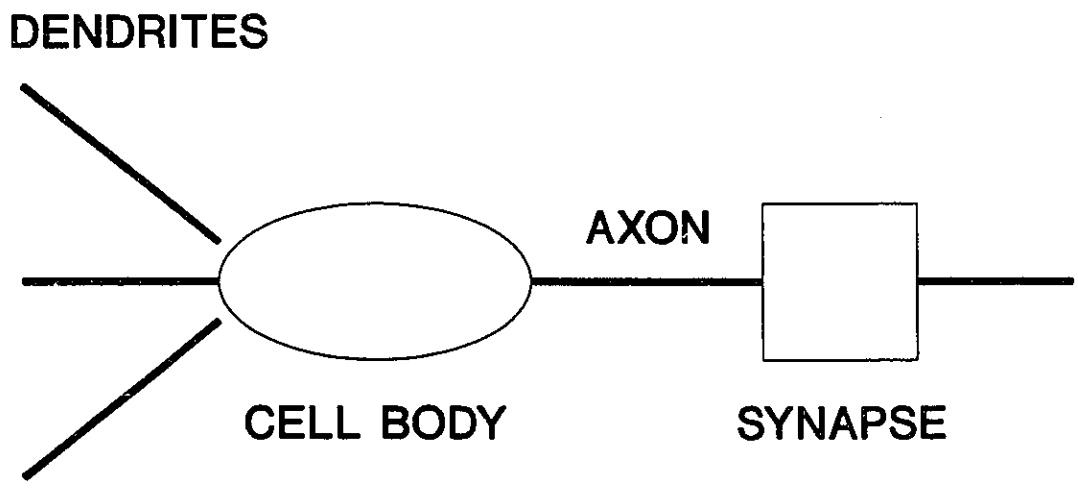

Figure 3.6 Neuron physiology model. The cell fires when a weighted sum of inputs from the dendrites exceeds a threshold.

Many variations of ANNs exist, ranging from computational-oriented parallel distributed processing (PDP) involving massively-connected multi-layered systems for optical character recognition [34], to reduced hardware-oriented two-level perceptron networks such as for adaptive phased array antenna controllers [35].

The Hopfield net approach to the derivation of large networks involves an energy surface approach, and is based on the determination of whether or not a neuron is firing. A second approach by Hoppensteadt [33] to neuron construction involves controlling large networks by synchronizing firing frequencies. This latter approach has been demonstrated to associate an energy function with phase-locking of a network of electrical oscillators. Hoppensteadt applied such phase-locking concepts to an ANN of voltage-controlled oscillator neurons (VCONs).

In an alternative approach to the VCON concept, a model involving an injection-locked oscillator neuron (ILON) is presented, using a resonator as the feedback element. Use of the latter is based on the similarity between the chemical equation governing diffusion in the biological synaptic gap, and that relating a coupled stimulus and an electrical resonator containing a gain medium. Relative advantages of the ILON model over the VCON include 1) reduced component count for large-array models and structures, 2) faster response and 3) operation in real-time at higher frequencies up into the gigahertz regime.

The potential difference V across a semipermeable-membrane separating regions of differing concentrations of electrically-charged chemical material may be expressed in terms of the Nernst equation, given as [33]

$$V = \frac{kT}{q} \cdot \log\left(\frac{C_1}{C_2}\right), \tag{3.10}$$

where k = Boltzmann constant, T = absolute temperature, q = ionic charge, while C_1 and C_2 are ionic concentrations on either side of the membrane. In neural physiology, signals are conveyed from dendrites to the cell body. If the pulse exceeds the neuron threshold for firing, an action pulse is generated and transmitted through the axon to the synapse. Neuro-transmitters are then generated in the synapse and diffuse through the synaptic gap to the next dendrite membrane.

The chemical kinetics governing concentration C of neuro-transmitters in the synaptic gap may be modelled as [33]

$$\frac{dC}{dt} = - k_{diff} \cdot C - k_{post} \cdot C + S, \tag{3.11}$$

where k_{diff} = rate constant for diffusion out of the synaptic gap, k_{post} = rate constant for combination with postsynaptic membrane, and S = source releasing neuro-transmitters into

the synaptic gap. It can be observed here that an analogous electrical kinetic equation may be deduced from COM formalism originally described in eqn (3.4). This equation may be regarded as a more general form of the low-frequency chemical-response mechanisms inherent in eqn (3.11).

A series circuit is shown in Fig. 3.7, for a neuron model of the synapse response. Here a resonator-type injection-locked oscillator of free-running angular frequency ω_0 is followed by a narrow-band bandpass filter centred at frequency ω_i , where ω_i is the input stimulus frequency to the oscillator and $\omega_i \neq \omega_0$. Resonator, frequency and voltage parameters are chosen to satisfy eqn (3.6) for the threshold locking condition $|K| < 1$. Under these conditions, application of an input injected voltage to satisfy the threshold will effect a synchronizing state of ω_i , similar to a "firing" of a neuron cell.

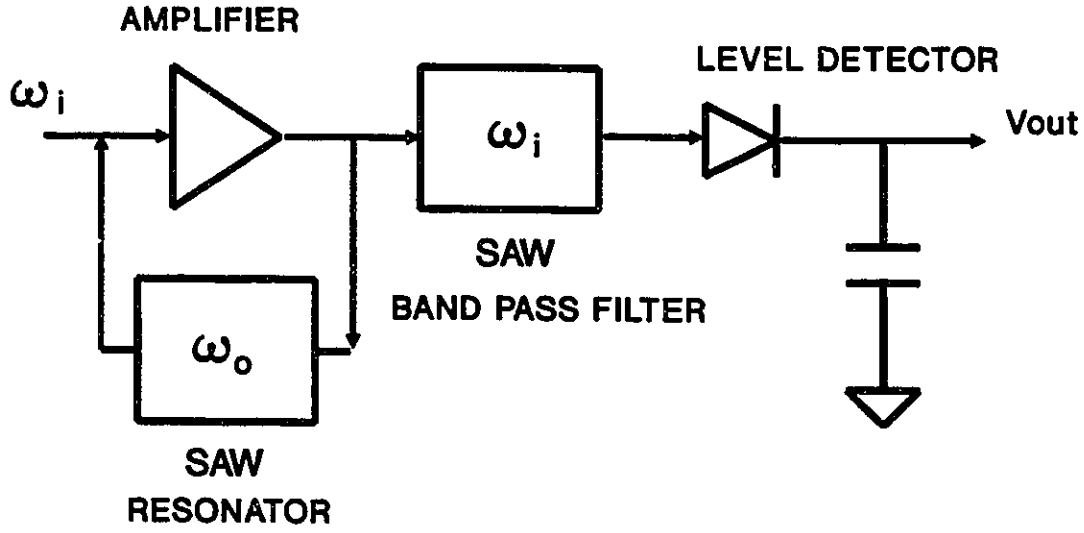

Figure 3.7 Series-connected ILO and level detector.

This will cause an increase in voltage at the level detector output, as the system locks.

The Hopfield model proposes an energy surface approach and an energy function $H(y)$

$$H(y) = -\frac{1}{2} \sum \kappa \cdot y_{inj} \cdot y_{out} \quad , \qquad (3.12)$$

where $\varkappa$ is the coupling between E_{inj} and the resonator parameters and y_{out} and $y_{inj} = y_{in}$ are represented from Fig. 2.8. The change in this energy function ΔH is then

$$\Delta H = -\Delta \omega_0 \cdot \sum \kappa \cdot y_{out} \, , \qquad (3.13)$$

where $\Delta\omega_0$ is the change between the frequency of the injected signal and the output signal. When $\Delta\omega_0 = 0$, the phase $\alpha(t) = 0$, in addition, $|K| = 0$ and the system is locked so that the energy surface can follow the contours of the phase $\alpha(t)$ as shown in Fig. 3.8. The flat plateau or global minimum on the right side of Fig. 3.8 indicates a phase locked state. The local minimum near the left side is actually a trough along the line of $|K| = 1$, where the oscillator has insufficient stimulus signal and is stable at its own free running frequency but is still higher in energy than the locked state.

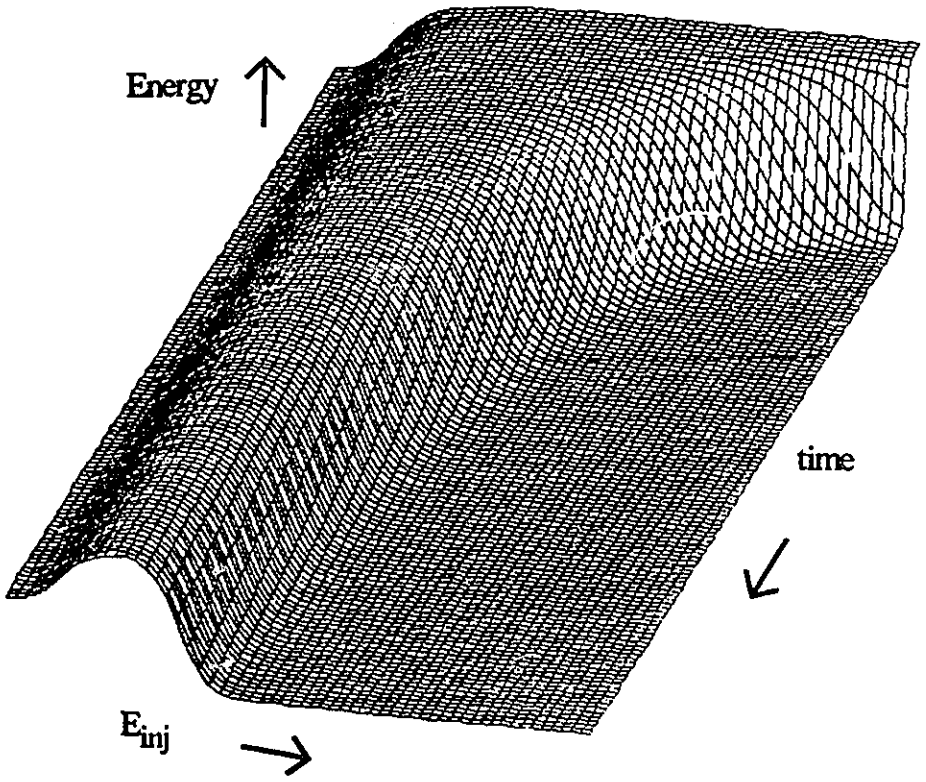

Figure 3.8 3-D plot of the oscillator's energy surface during a locking sequence. The axes are the same as in Fig. 3.4, with the flat "valley" indicating a stable locked condition.

3.4.4 An Equivalent Self-Organized Neural Network

Within this section a SAW based neural network that can associate, categorize and store input stimuli is presented. The network can be modelled as a modified Kohonen self-organizing feature map.

The concept of adapting several ILONs to form a feature map can easily be realized by a multimode ILO. A momentary input signal at frequency f_x will excite (associate) only one mode of the multimode SAW device. This signal will lock the oscillator (categorize) to f_x and the oscillator will remain locked even if the input stimulus is removed (store). A full description of this atypical application is reproduced in reference [18] which is reproduced in its entirety in Appendix D.

CHAPTER 4

SAW OSCILLATORS IN THE VICINITY OF INJECTION LOCKING

4.1 Introduction

The results of the previous chapter have shown that a completely locked oscillator will be in absolute synchronization with the injected signal. This chapter will illustrate the benefits of keeping the oscillator in the vicinity of the locked condition.

An analogy will be shown between the dynamic behaviour of a SAW ILO and its similarity near lock-in to that of an acousto-optic modulator. This analogy includes a reflective wave component travelling between the injected source and the oscillator, resulting in momentary locking and unlocking of the system. These reflected waves are responsible for the classical modulation sidebands near lock-in.

An equation can be developed to predict the dynamic amplitude just prior to lock-in, that has similarities to an acousto-optic modulator. Within the modulator, the sidebands due to the acoustic signal regenerate about the incident signal to produce a diffracted signal, $\omega_d = \omega_i \pm m\omega_a$ where m is an integer >>1. For the case of an ILO, the output waveform is equal to $\omega_{out} = \omega_{osc} \pm m\Delta\omega$

Further experimental results achieved by this author for an analog-to-digital converter and data multiplexer will serve to confirm the importance of the relationship of $\omega_{out} = \omega_{osc} \pm m\Delta\omega$

4.2 Theory of the Dynamics in the Vicinity of Lock-in

A reflection coefficient Γ can be developed to evaluate the dynamics of an oscillator at various levels of injected amplitude S_+ and reflected amplitude S_- . From Haus [10] , $\Gamma = S_- / S_+$,where

$$\Gamma = \frac{(1/\tau_e)-(1/\tau_o)-j(\omega_i-\omega_o)}{(1/\tau_e)+(1/\tau_o)+j(\omega_i-\omega_o)} \quad . \qquad (4.1)$$

A similar phenomenon occurs within an ILO in terms of the summation of signals to produce multiple sidebands within the device. Within an ILO the relationship for the mode amplitude is the sum of the oscillator, injected and reflected signals S_{+m} and S_{-m} , where

$$S_{+\,m+1}(t) = \Gamma \cdot S_{+\,m} \cdot e^{(+j\Delta\omega t)} \qquad (4.2)$$

and

$$S_{-\,m+1}(t) = \Gamma \cdot S_{-\,m} \cdot e^{(-j\Delta\omega t)} \quad . \qquad (4.3)$$

A plot of the dynamic mode amplitude versus time is shown in Fig. 3 of Appendix D. The frequency response of this composite waveform is illustrated in Fig. 4 of Appendix D where the classic cascading sidebands inherent to the vicinity of lock-in are distinguished. The experimental results relating to these previous figures are shown in Appendix D Figs. 7a,b, respectively. Here the injected signal perturbs the oscillator's waveform, with the occurrence of standing waves . A similar sequence is described below for an acousto-optic modulator.

An in-line acousto-optic frequency translator for fiber-optic sensors is illustrated in Fig. 4.1, see reference [36]. The device operates at a fixed wavelength of 723 nm (f_o = 414.9 x 10^{12} Hz) propagating down the titanium waveguide that is electrically isolated from the IDTs by an insulating layer.

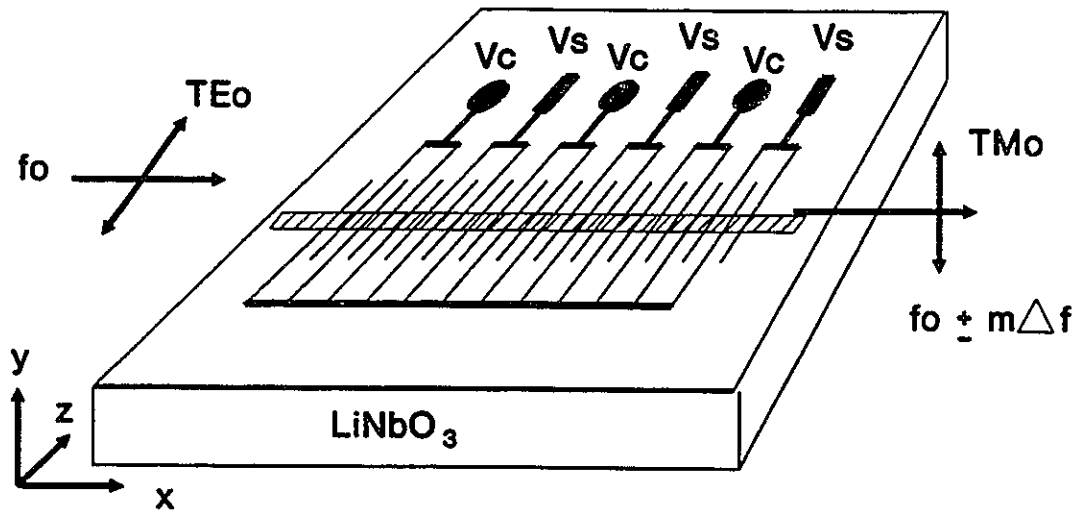

Figure 4.1 Schematic of a frequency shifter within a lithium niobate substrate:titanium waveguide structure.

An injected signal at a frequency f_{inj} is applied in phase quadrature to positions Vs and Vc on the interdigital transducers. The resulting optical waveform exiting from the device is translated from a TE to a TM mode due to the applied voltage and has shifted in frequency equal to the difference Δf of the injected signal and the input mode frequency f_o. Since this system also follows eqns (4.1), (4.2) and (4.3) there will be subsequent side-bands at $\pm m \Delta f$ locations. Figure 4.2 displays the theoretical result of the above equations and should be compared to Fig. 4 of reference [36]. Here the mode input frequency f_o is normalized to 20, with $f_{inj} = 18$ and $\Delta f = 2$.

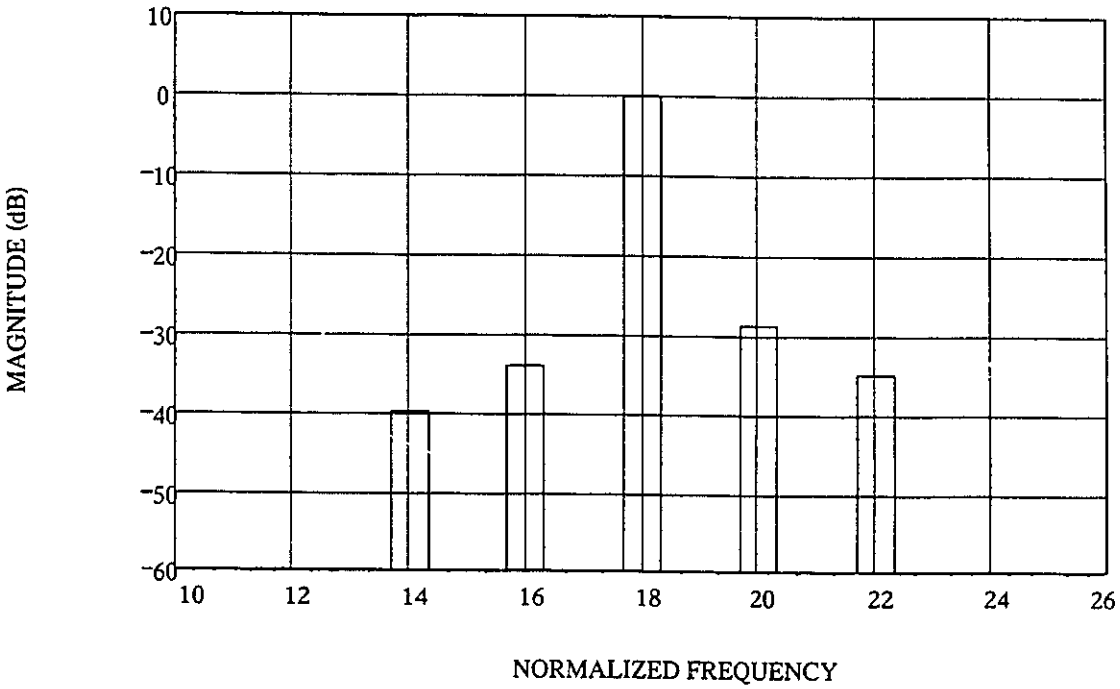

Figure 4.2 A theoretical plot of an acousto-optic frequency translator.

4.3 Circuit Applications

The following three circuit applications will demonstrate the usefulness of allowing an ILO to remain in the vicinity of locking.

4.3.1 Carrier Recovery Circuit

A SAW-based carrier recovery system for wireless binary phase shift keying (BPSK) input signals operating at 915 MHz was designed by the author. The successful operation of this circuitry relies on the partial loss of synchronization of the ILO during the phase transition of the BPSK signal. As the ILO re-locks it goes through a phase transition $\alpha(t)$ of eqn (3.7) shown previously in Fig. 3.3. A "zero to one" or "one to zero" binary transition will force in the ILO to either a positive or negative phase slope. This will correspond to a positive- or negative-going pulse on the output of a phase detector, to provide binary detection. A full description of this carrier-recovery technique is described in the author's references [29], [37] and are reproduced in their entirety in Appendix E and Appendix F respectively.

4.3.2 Analog-to-Digital Converter

An equivalent analog-to-digital (A/D) converter circuit can be constructed from an ILO that is held in the vicinity of lock-in. Following the oscillator mode amplitude described previously by eqn (3.4) of chapter 3, (and working with powers instead of voltages), as the injected signal power P_{inj} is increased to a point of lock-in, the beat frequencies do not remain constant. As the injected signal increases in value the

difference frequency, Δf, decreases from an initial $\Delta f = f_{osc} - f_{inj}$ to a final locked condition of $\Delta f = 0$. This effect is plotted in Fig. 4.3. If the Δf were to be connected directly to a frequency counter, then a binary number can be derived from an injected signal power P_{inj}.

Another inherent advantage of this A/D converter is its capability to perform at signal frequencies well above several hundred MHz. That is, there is an immediate real time conversion by simply connecting a frequency counter to the output of an ILO to register the beat frequency Δf. All sampling is done in the kHz range while the input signal could be in the GHz range.

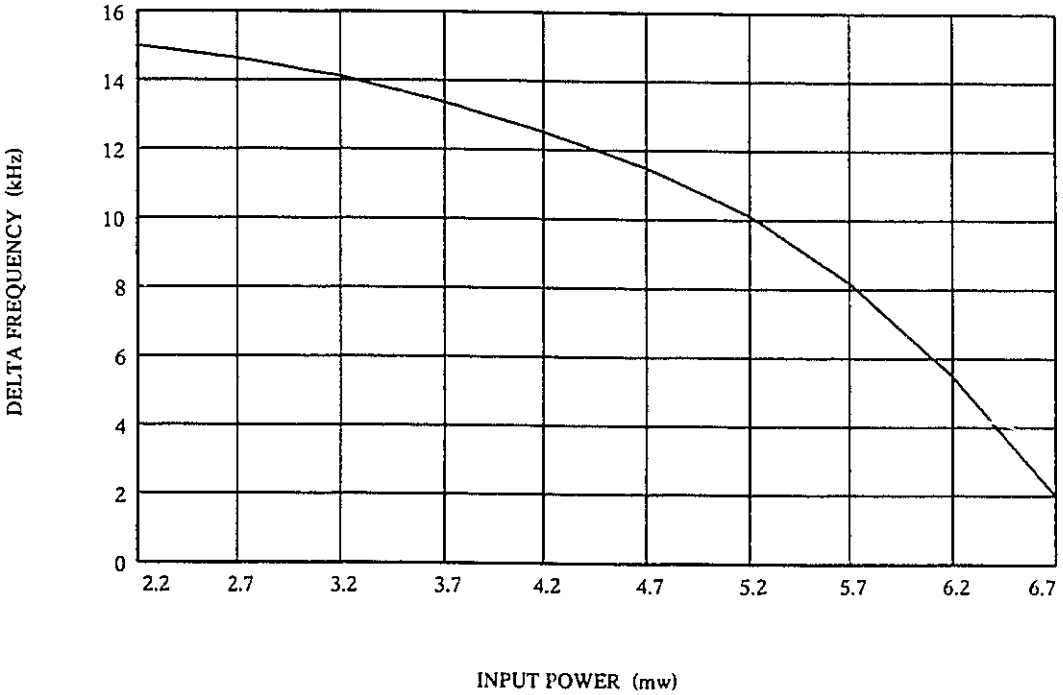

Figure 4.3 Experimental data indicating the relationship of P_{inj} in mW and the beat frequency Δf in kHz.

4.3.3 Data Multiplexer

If eqns (4.2) and (4.3) are modified to include a modulated injected signal rather than a continuous wave (CW) one, then the spectrum will be altered slightly. Figure 4.4 illustrates the theoretical spectrum of such a combination that still follows $\omega_{out} = \omega_{osc} \pm m\Delta\omega_{mod}$, where m is again an integer >>1. The most noticeable feature is that the sidebands due to the modulation $m\Delta\omega_{mod}$ spread out as m increases. This is due to each reflected component being multiplied by the previous incident component times the reflection coefficient. The $\Delta\omega_{mod}$ component is therefore widened by the factor of m on each reflection.

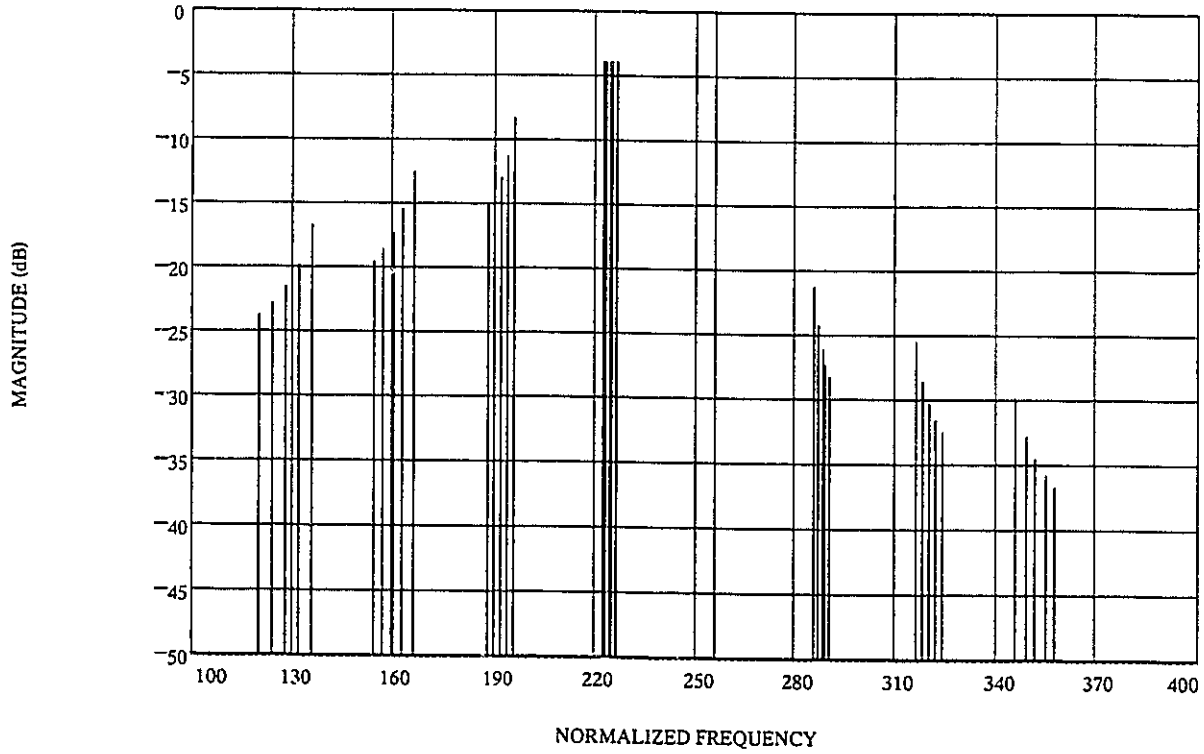

Figure 4.4 Theoretical beat spectrum of a normalized 256-Hz SAWR oscillator injected with a 226-Hz signal with 5-Hz of frequency deviation.

The power of this system is demonstrated in Fig. (4.5) and Figs. 4.6(a,b,c) that illustrate an ILO subjected to a frequency modulating injected signal. Figure 4.5 is a wideband spectrum of an 81.678-MHz SAWR oscillator being injected with an 81.828-MHz signal with 19-kHz of deviation.

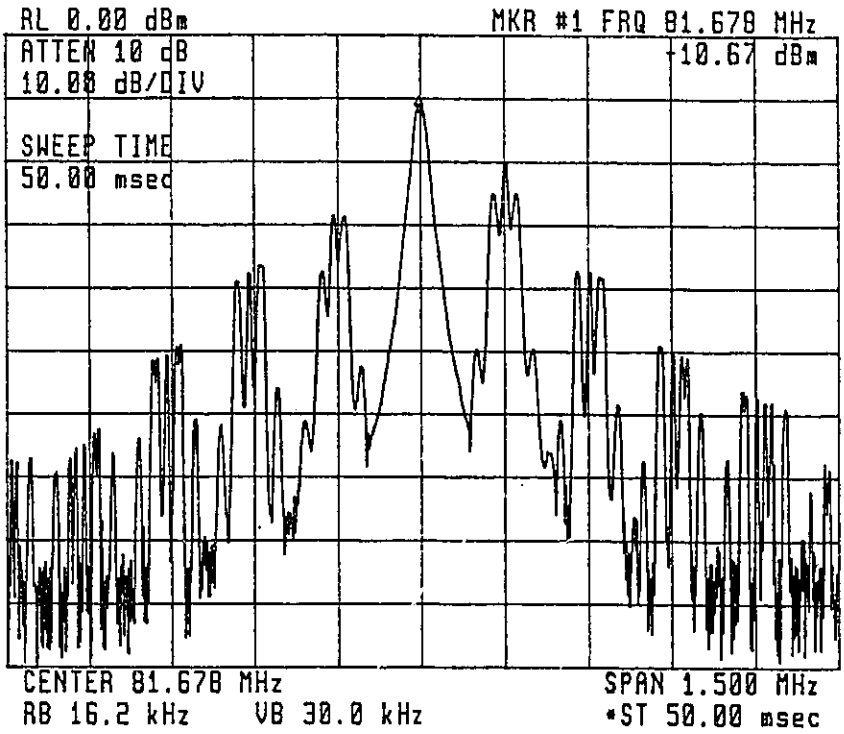

Figure 4.5 Experimental wideband display of a spectrum analyzer indicating the beat frequencies of a SAWR 81.678-MHz oscillator with a 19-kHz deviation, FM injected signal. Horizontal scale 150 kHz / div, centred at 81.678 MHz ; vertical scale, 10 dB/div. Centre peak measured at -10.67 dBm.

Figures 4.6(a,b,c) demonstrate that the modulating frequency is increased by 38 kHz, 57 kHz and 76 kHz, respectively for each decreasing sideband. If the injected signal were to be a BPSK signal then the bit rate would increase by increasing integers for each sideband. With no digital components, the bit rate could be multiplexed up to a faster bit rate and still remain synchronized due to the fixed starting position shown in eqn (4.2) and eqn (4.3).

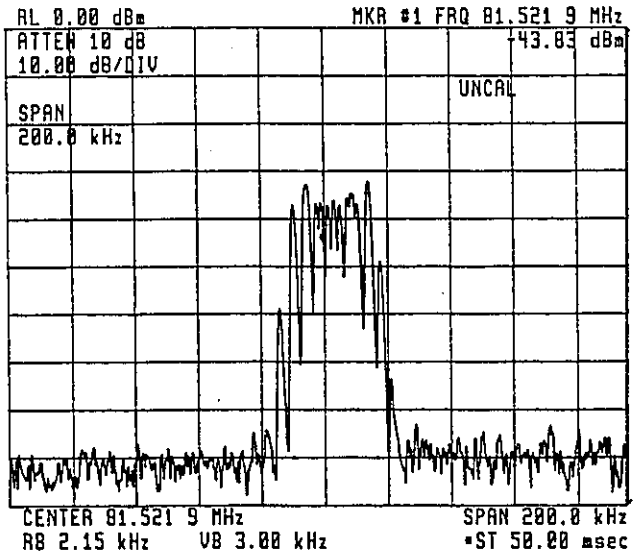

Figure 4.6a First sideband at 81.521 MHz showing a doubling of the initial deviation from 19 kHz to 38 kHz. Horizontal scale 20 kHz / div, centred at 81.521 MHz ; vertical scale, 10 dB/div. Centre amplitude measured at - 37.2 dBm.

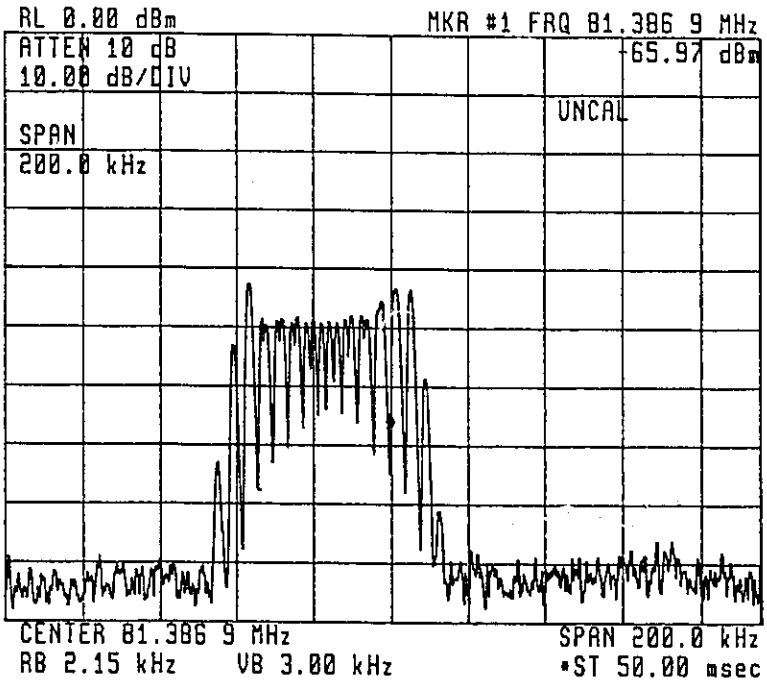

Figure 4.6b Second sideband at 81.386 MHz showing a tripling of the initial deviation from 19 kHz to 57 kHz. Horizontal scale 20 kHz / div, centred at 81.386 MHz ; vertical scale, 10 dB/div. Centre of sideband measured at - 49.5 dBm.

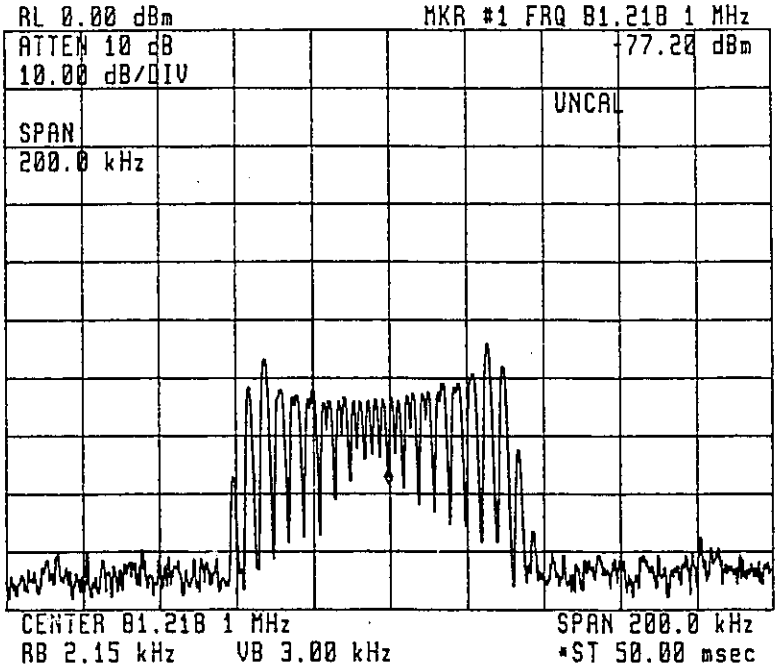

Figure 4.6c Third sideband at 81.218 MHz showing a quadrupling of the initial deviation from 19 kHz to 76 kHz. Horizontal scale 20 kHz / div, centred at 81.218 MHz ; vertical scale, 10 dB/div. Centre of sideband measured at - 63.5 dBm.

CHAPTER 5

SAW BASED NON-LINEAR DYNAMICAL SYSTEM

5.1 Introduction

The previous chapter described several driven-unlocked SAW oscillators in signal conversion systems. In those circuits the loop amplifier was operating in a low saturation condition. In the studies described in this chapter, the loop amplifier in a driven-unlocked SAW oscillator is purposely overdriven. The oscillator output is then used to drive yet another saturated amplifier, which results in a very non-linear dynamical state. The state that prevails is near a chaotic condition [38].

The schematic of a driven-unlocked SAW oscillator employing a resonant SAW feedback element and a over-driven loop amplifier (AMP #1) is shown in Fig. 5.1, together with an ancillary external over-driven amplifier (AMP #2). Here, the injection signal frequency and power level are appropriate for a driven-unlocked SAW oscillator operation.

Chaos theory is used to model the pulse output of Fig. 5.1 by using a forced Duffing equation [38-39]. Within a driven non-linear oscillator system, closed-form analytical solutions are not available and access must certainly be made to numerical analysis. The solution to these numerical techniques will produce *two alternate stable states*, which can be modelled by a twin-well potential [40]. The switching between these

states will imitate the locking and unlocking conditions within the oscillator loop. Experiments involving measuring frequency-versus-time with a modulation analyzer (Fig. 8 of appendix D) have shown that the oscillator momentarily locks then unlocks with a periodicity of $T = 1/\Delta f$ [10]. This phenomenon initiates the intermittency of this system.

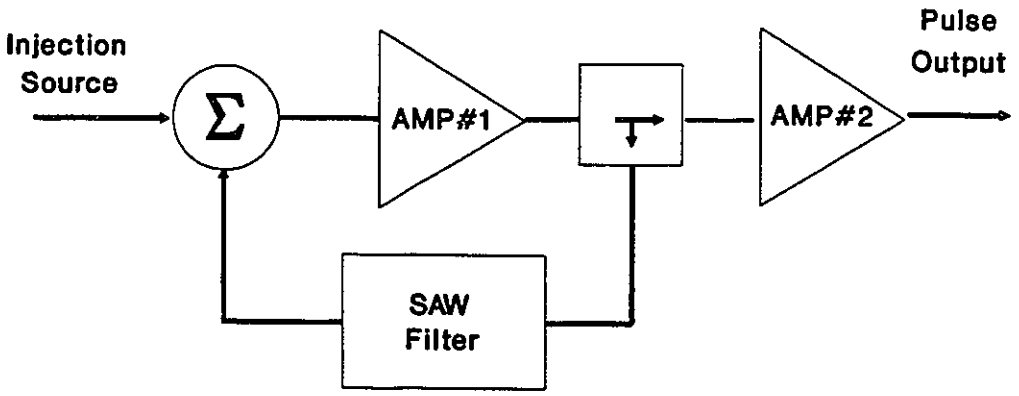

Figure 5.1 An injected over-driven SAW oscillator with a non-linear output amplifier.

The non-linear loop amplifiers distort the beat spectrum that normally has a linear slope on either side of the injection frequency, shown in Fig. 4 of Appendix D. This results in a spectrum with a non-uniform amplitude distribution. Groups of various sets of $\pm n\Delta\omega$ can then be considered as frequency-splitting about the injecting frequency. This can lead to a massive period-doubling effect that can be plotted as chaotic bifurcations on a Feigenbaum tree [38]. Under certain injection powers, a manifold develops to produce a pulse with a repetition rate of periodicity T. In the limit, as the oscillator goes

from the driven-unlocked to the injection-locked state, the analytic Feigenbaum tree collapses onto itself and the output is a stable continuous wave (CW).

5.2 Theory of Non-Linear Dynamics and Chaos

A non-linear oscillator that is perturbed by a forcing signal can be modelled as a forced Duffing eqn [38-39],

$$y'' + 0.04y' - 0.2y + \frac{8}{15}y^3 = 0.4\cos(2\pi ft) \qquad (5.1)$$

where f is the excitation frequency. A solution to this ordinary differential equation (ODE) can be realized by numerical techniques by rewriting the ODE of eqn (5.1) as

$$y'(2) = A \cdot y(1) - B \cdot y^3(1) - C \cdot y(2) + C \cdot \cos(2\pi ft) \qquad (5.2)$$

$$y'(1) = 2\pi \cdot 3.3 \cdot y(2) \quad , \qquad (5.3)$$

where $A = 1.32\pi$, $B = 6.6\pi$ and $C = 0.264\pi$.

A plot of the attractor of y' versus y is shown in Fig. 5.2. This plot indicates that there exists two stable equilibria and it takes some finite time T' until enough energy is collected (or injected) before a transition to the other attracting basin is possible.

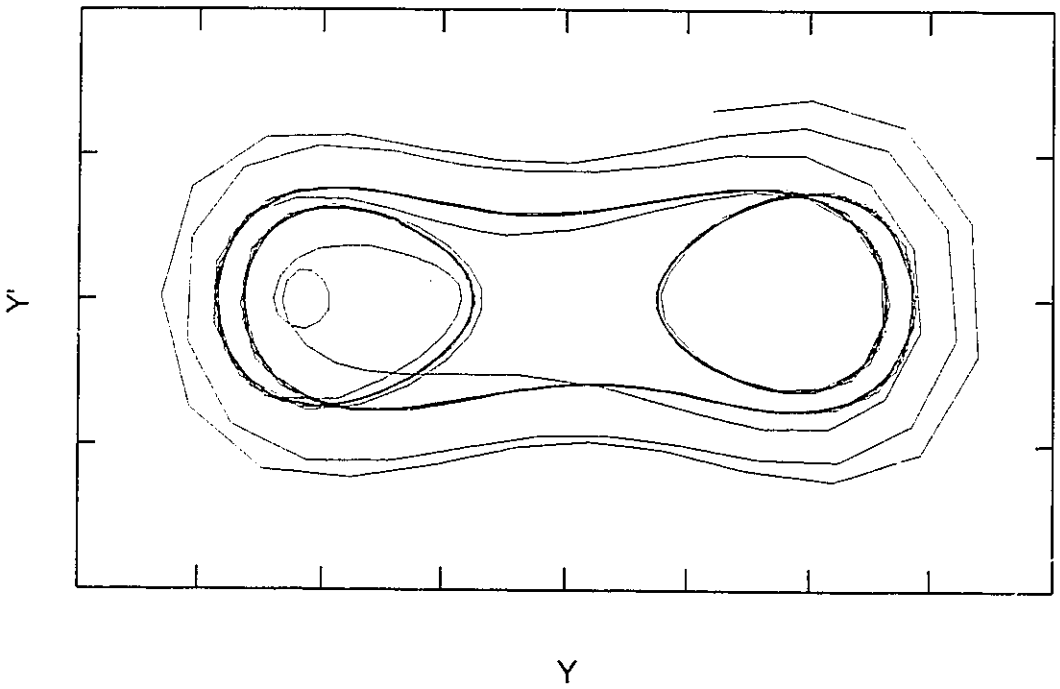

Figure 5.2 Phase plot of the Duffing equation showing two stable equilibrium states.

In the driven-unlocked state, this dynamical system possesses a transient periodicity T, due to the circuit momentarily locking then unlocking, (as is observed experimentally with a frequency-modulation analyzer). The related circuit equation can be expressed as

$$f(\kappa,t) = f(\kappa,t + T) \qquad (5.4)$$

a non-autonomous continuous-time dynamical system. Figure 5.3 illustrates this system by using eqns (5.2) and (5.3) to produce a periodic waveform.

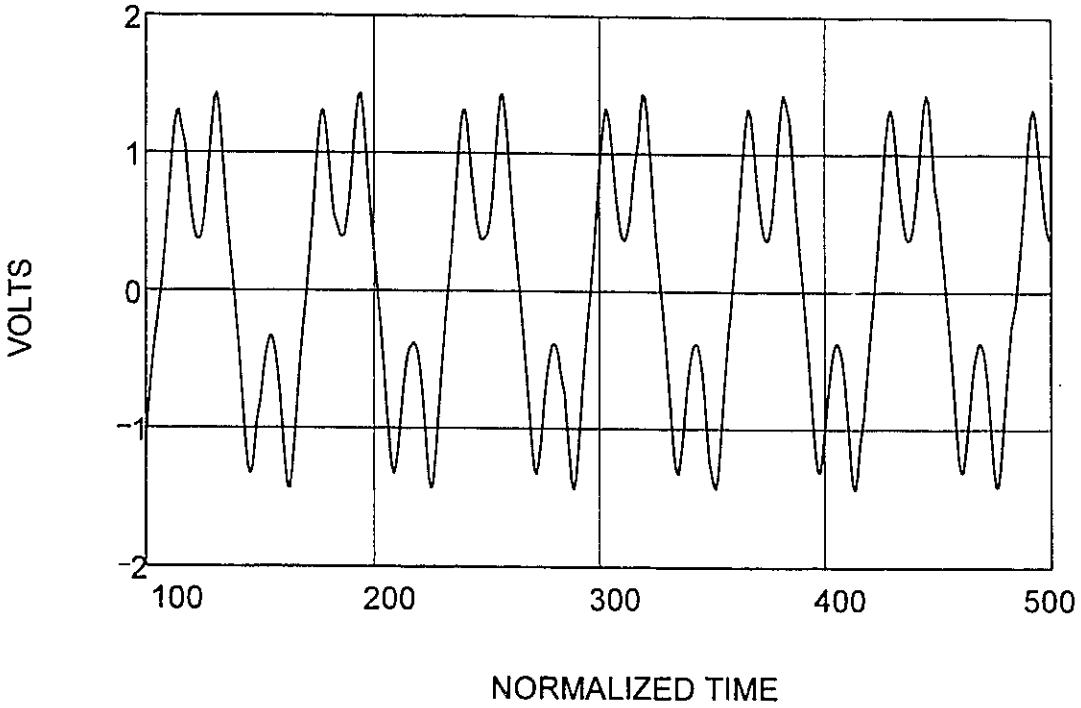

Figure 5.3 Amplitude versus time plot, showing the intermittency of the Duffing waveform.

A simple mechanical analogy that incorporates eqns (5.2) and (5.3) is shown in Fig. 5.4, where a ball is placed in a twin-well potential with a base vibrating with a periodic motion ω_{inj} [40]. The shape of the two potential wells is critical. One well is

shallow and broad to allow the ball to oscillate back and forth to produce a large amplitude at a certain oscillating frequency. The other well is deep and very narrow. The ball stops at the bottom of the well and remains stationary until the system changes state. For these cases the ball escapes from one well to the other when the base is perturbed by a changing phase angle $\alpha(t)$ between the oscillator and injected signal (from chapter 3 eqn 3.7 that is displayed in Fig. 3.3). The slope of the phase angle $\alpha(t)$ depends on whether the injecting frequency is greater or less than the oscillator frequency, and would be analogous to bumping the base to the right or left respectively.

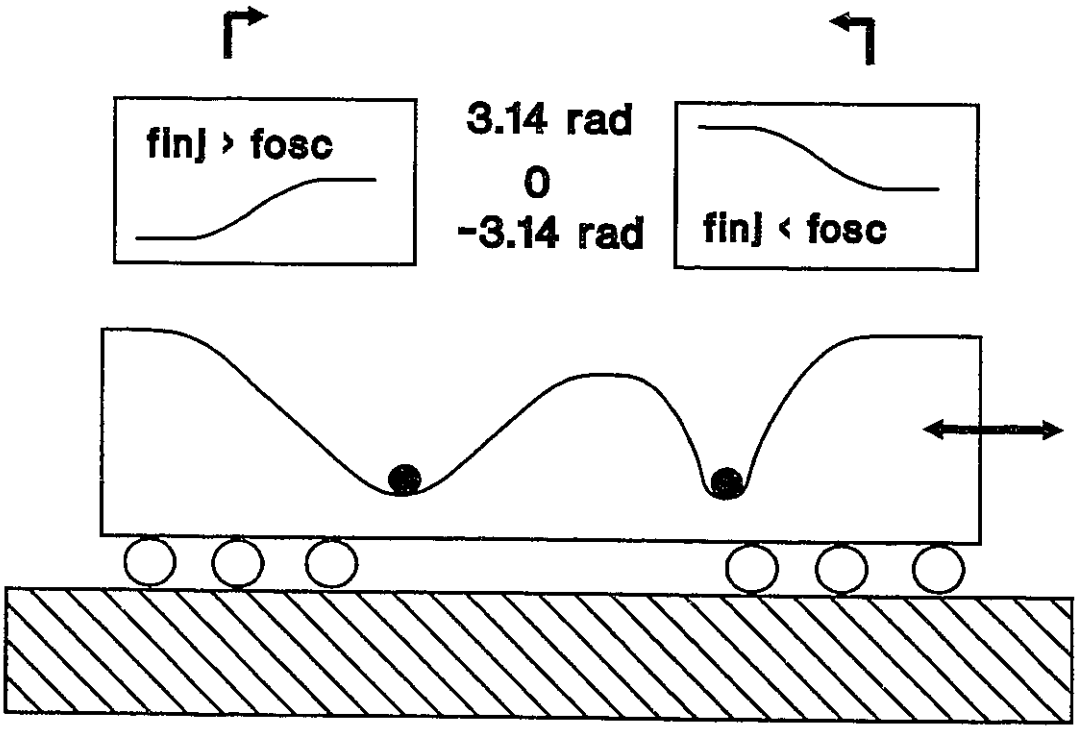

Figure 5.4 A physical model of an unequal twin-well potential oscillator.

5.3 Experimental Results

A SAWR oscillator with a free-running frequency of 82.27000 MHz was used in the circuit of Fig. 5.1, with an output power of 0 dBm feeding into amplifier A2. The gain of loop amplifier A1 was then increased to produce an overdriven loop output of +5 dBm to the input of amplifier A2. The driven-unlocked injection frequency f_{inj} was 82.37400 MHz and the output amplifier A2 gain was set at 26 dB.

5.3.1 Pulse Generator

The photographs shown in Fig. 5.5 (a-d) illustrates the massive period doubling taking place at the output of amplifier A2 from Fig. 5.1. The period, T, between the nulls in Fig. 5.5a, would be $T = 1/\Delta f$, where Δf is the original offset between the free-running oscillator and the injected signal. The intermittent pulse of Fig. 5.5c, only occurs for a narrow range of injected powers. Figure 5.5d, illustrates the locked condition. Table 5.1 compares the injected power for each phase of the waveform.

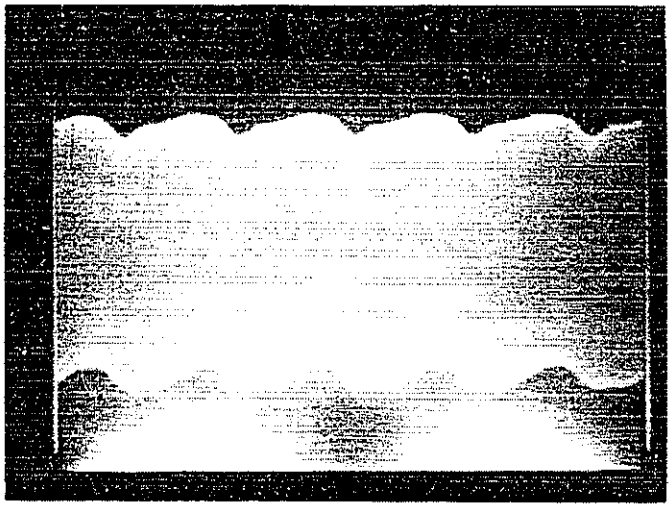

Figure 5.5a Beginning of the bifurcation process. Vertical scale is 0.1 volts per division and the horizontal scale is 5.0 μs per division.

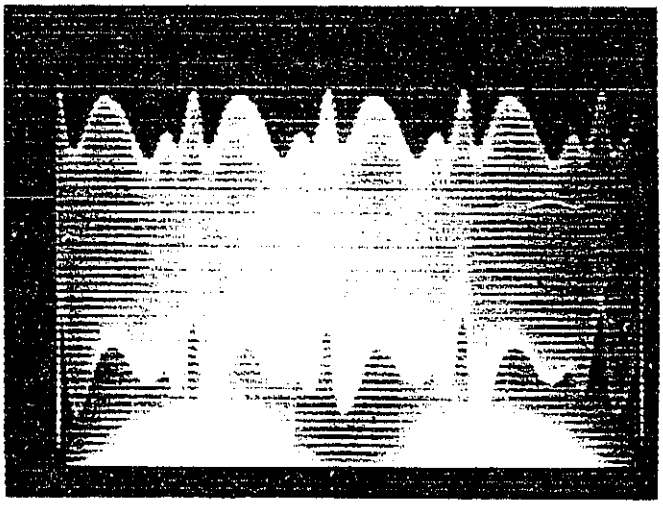

Figure 5.5b Continuation of the bifurcation process. Vertical scale is 0.1 volts per division and the horizontal scale is 5.0 μs per division.

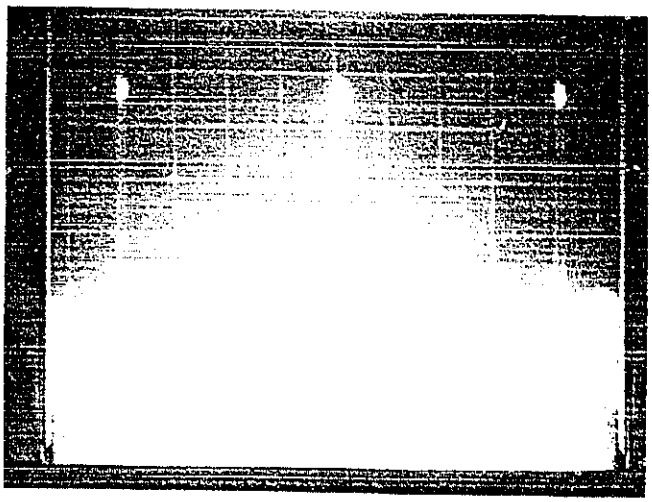

Figure 5.5c Photograph of an intermittent pulse condition. Vertical scale is 0.1 volts per division and the horizontal scale is 5.0 μs per division.

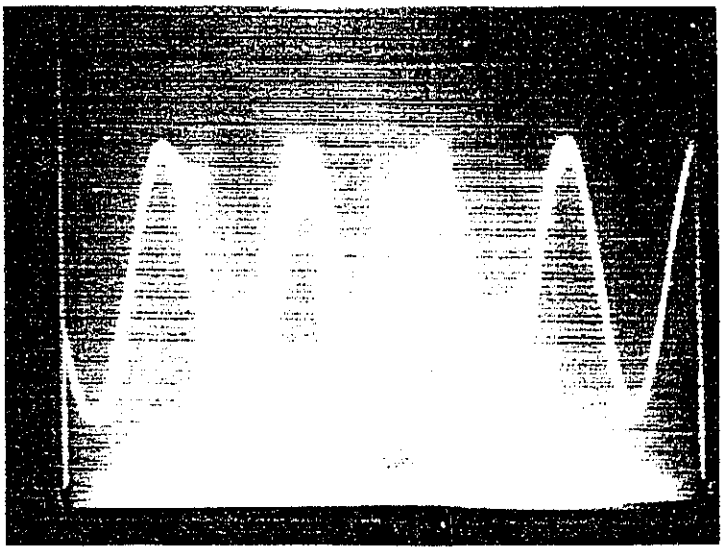

Figure 5.5d Photograph of the locked condition with the output signal now tracking the input signal. The vertical scale is 0.1 volts per division and the horziontal scale is 5 ns per division.

Table 5.1

Comparison of waveform bifurcations and injected powers

Figure number	Injected power dBm	Injected power μW
Figure 5.5 a	-16.0 dBm	25.0 μW
Figure 5.5 b	-13.0 dBm	50.1 μW
Figure 5.5 c , pulse	-11.9 dBm	64.5 μW
Figure 5.5 d , locked	-11.1 dBm	76.7 μW

A plot of measured period bifurcations (period-doublings) versus P_{inj} is shown in the Feigenbaum tree of Fig. 5.6. The vertical scale is in volts and the horizontal scale is P_{inj} in microwatts. This bifurcation process expands, then collapses when the SAW oscillator finally acquires injection-lock at about -11.1 dBm (76.7 μW).

It is interesting to note that the bifurcations producing the pulse, only occur at the output of the final amplifier A2 and not within the inner oscillator loop.

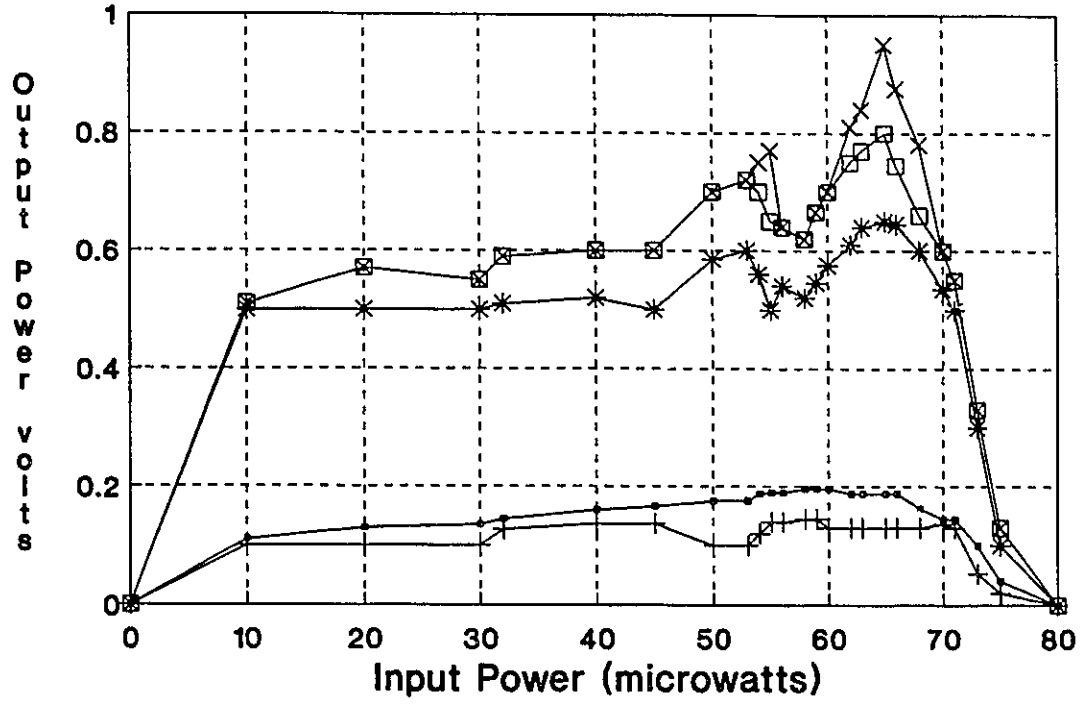

Figure 5.6 Feigenbaum tree with an incomplete period-doubling cascade.

5.3.2 Pulse Generator with Feedback

A modification to Fig. 5.1 was made to include a feedback element, with a variable attenuator, to connect the output of the final amplifier to the injection point. This circuit is shown in Fig. 5.7 with the injected power, P_{inj} held at - 18 dBm and f_{inj} = 82.3850 MHz.

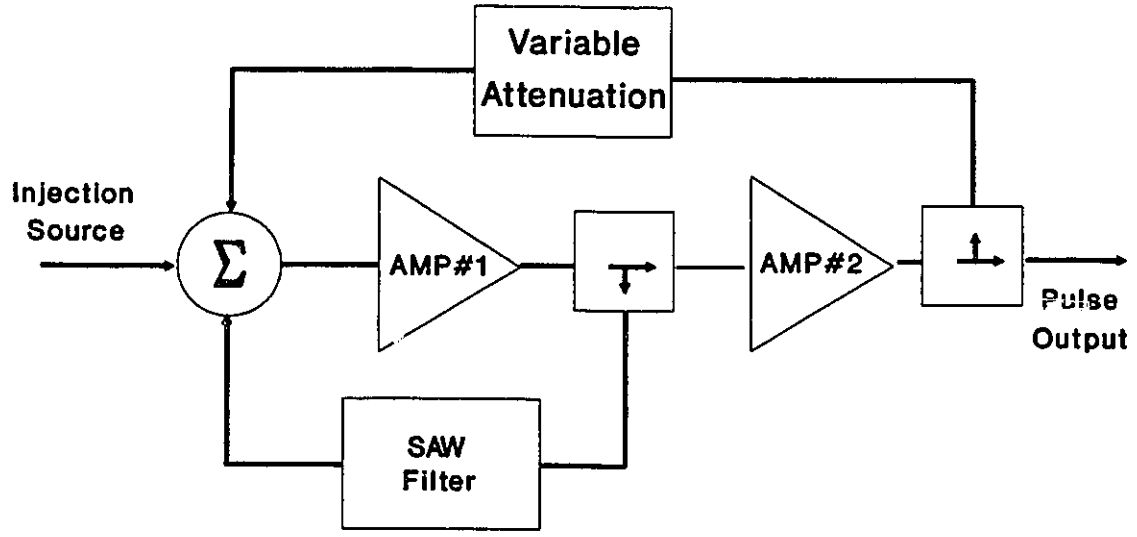

Figure 5.7 A non-linear dynamical system with variable feedback.

The effect of this modification appears in the sequence of photographs shown in Fig. 5.8 a-d. The pulse width is now variable as the attenuator is changed, which in effect changes the sharpness of the right-hand potential well of Fig. 5.4. The pulse changes approximately 0.1 μs in width for every 5-dB change in feedback attenuation. Table 5.2 summarize these results.

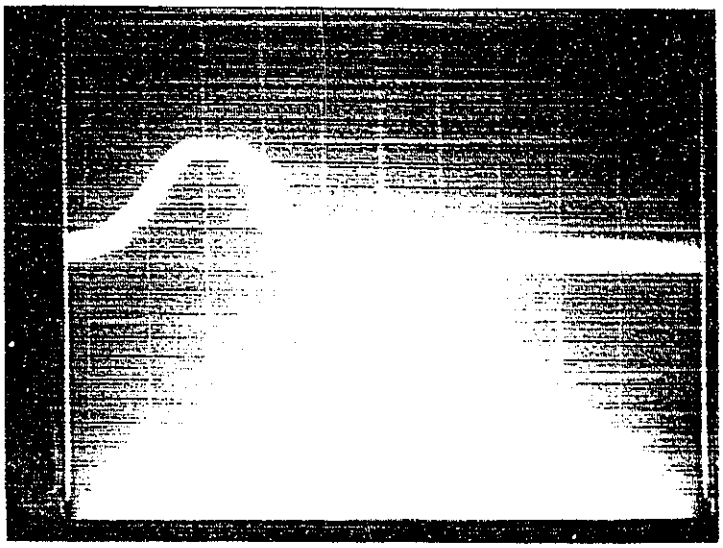

Figure 5.8a Beginning of the pulse widening. Vertical scale is 0.5 volts per division and the horizontal scale is 0.1 μs per division.

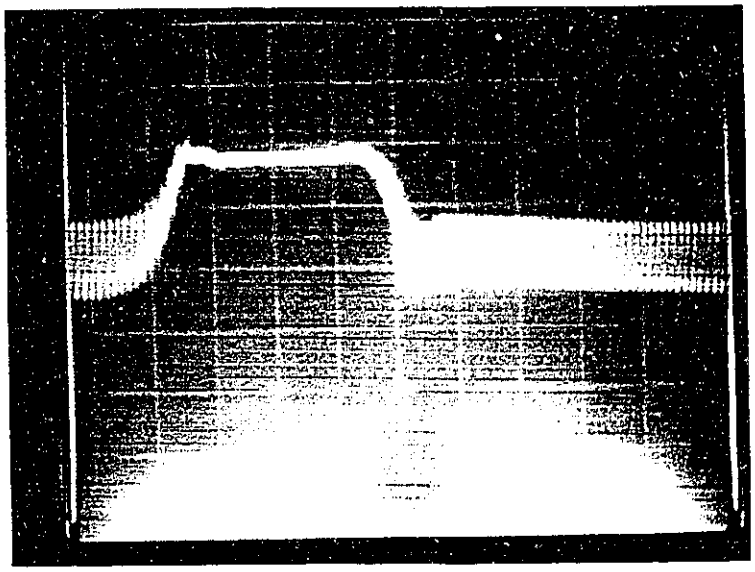

Figure 5.8b Continuation of the pulse widening. Vertical scale is 0.5 volts per division and the horizontal scale is 0.1 μs per division.

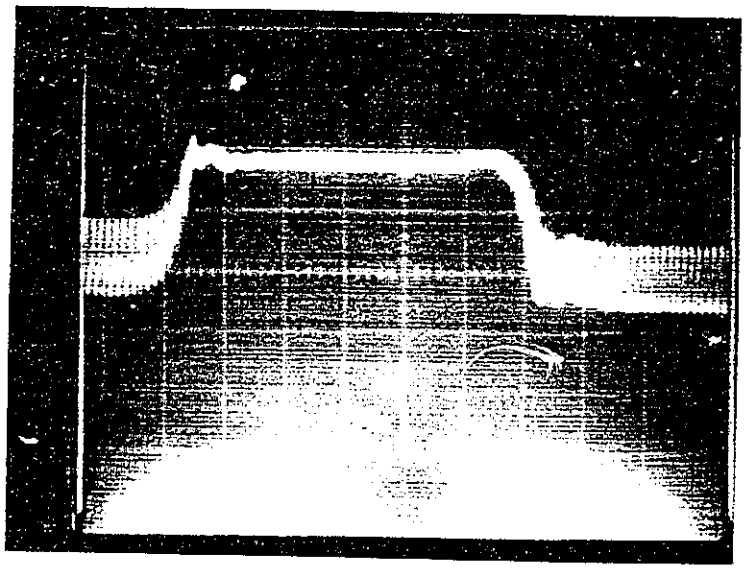

Figure 5.8c Further deepening of the pulse's potential well. Vertical scale is 0.5 volts per division and the horizontal scale is 0.1 μs per division.

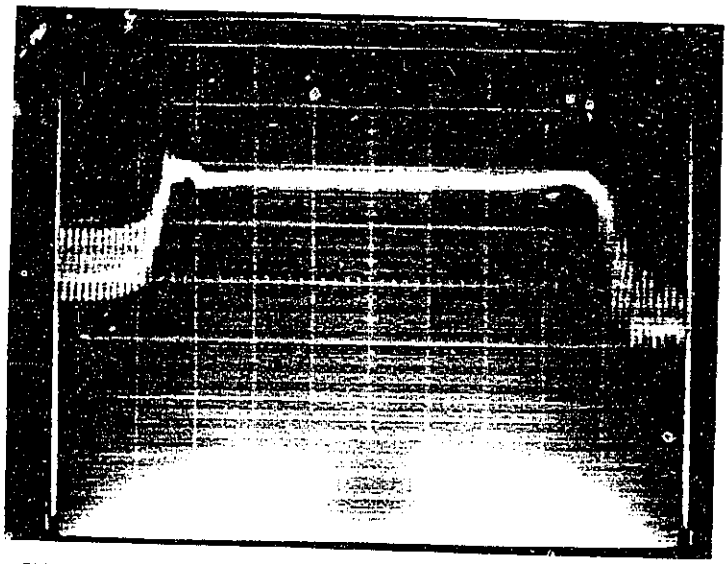

Figure 5.8d The flat top and the length of the pulse indicates a very sharp and deep well. Vertical scale is 0.5 volts per division and the horizontal scale is 0.1 μs per division.

Table 5.2

Summary of pulse width and the attenuation in the feedback loop

Figure Number	Attenuation	Pulse Width
Figure 5.8 a	52 dB	0.1 μs
Figure 5.8 b	47 dB	0.3 μs
Figure 5.8 c	42 dB	0.5 μs
Figure 5.8 d	35 dB	0.7 μs

PART II

COUPLING-OF-MODES STUDIES FOR SAW DEVICES

CHAPTER 6

DUAL-MODE LEAKY-SAW RESONATOR FILTERS

6.1 Introduction

For the past two years, there has been a growing interest in wideband SAW filters at the 900-MHz region for personal communication services (PCS). A popular design includes the three-IDT dual-mode leaky structure on 64° $LiNbO_3$ [5], [11], [41] and [42]. This filter has several benefits such as a 3% to 4% bandwidth capability, insertion loss < 4 dB when two are in cascade and a 50 Ω impedance match [11] and [41]. The three-IDT dual mode structure (DMS) filter is the most stable device when manufacturing tolerances in the fabrication processes are considered. Other filters structures such as the image impedance connection (IIC) and the interdigitated interdigital transducer (IIDT) that have been compared to the DMS in the above statement are illustrated in Fig. 6.1. The major disadvantage of these other two filters is the higher number of fingers that could be affected by etching abnormalities resulting in frequency shifts or catastrophic shorts.

Two contributing factors that govern the characteristics of the DMS filter are, the reflections caused by the input and output IDTs and the increased attenuation of the reflection coefficients of the grating and IDT structures above the reflection stopband . The self reflections within each of the input or output IDTs are a function of the fingers' metal height-to-wavelength ratio or film-thickness ratio (h/λ). It has been observed for

many years when dealing with simple two-port resonator structures that an increase in metallization will cause a downward shift in frequency of the radiation conductance. Almar et al have observed this reaction for the downward shifting of the passband as the film-thickness ratio (h/λ) was increased in an STW resonator filter structure [43]. The increase in the attenuation above the stopband of either the reflection or IDT gratings is due to the unique propagation characteristics of the leaky wave which is not completely horizontal to the surface of the substrate, resulting in an increase in the loss factor of the gratings [44].

6.2 Radiation Conductance in the Presence of Finger Reflections

The radiation conductance for an IDT can be expressed as previously shown in chapter 2 with eqns (2.3), (2.5) and (2.6), without any consideration of finger edge reflections. For the analysis of the leaky-DMS filter using the COM program the radiation conductance again without any consideration for finger reflections can be expressed as a reiteration of eqn (2.3)

$$G_a = 8 \cdot N_a^2 \cdot G_o \cdot [\frac{\sin(x)}{x}]^2 . \qquad (6.1)$$

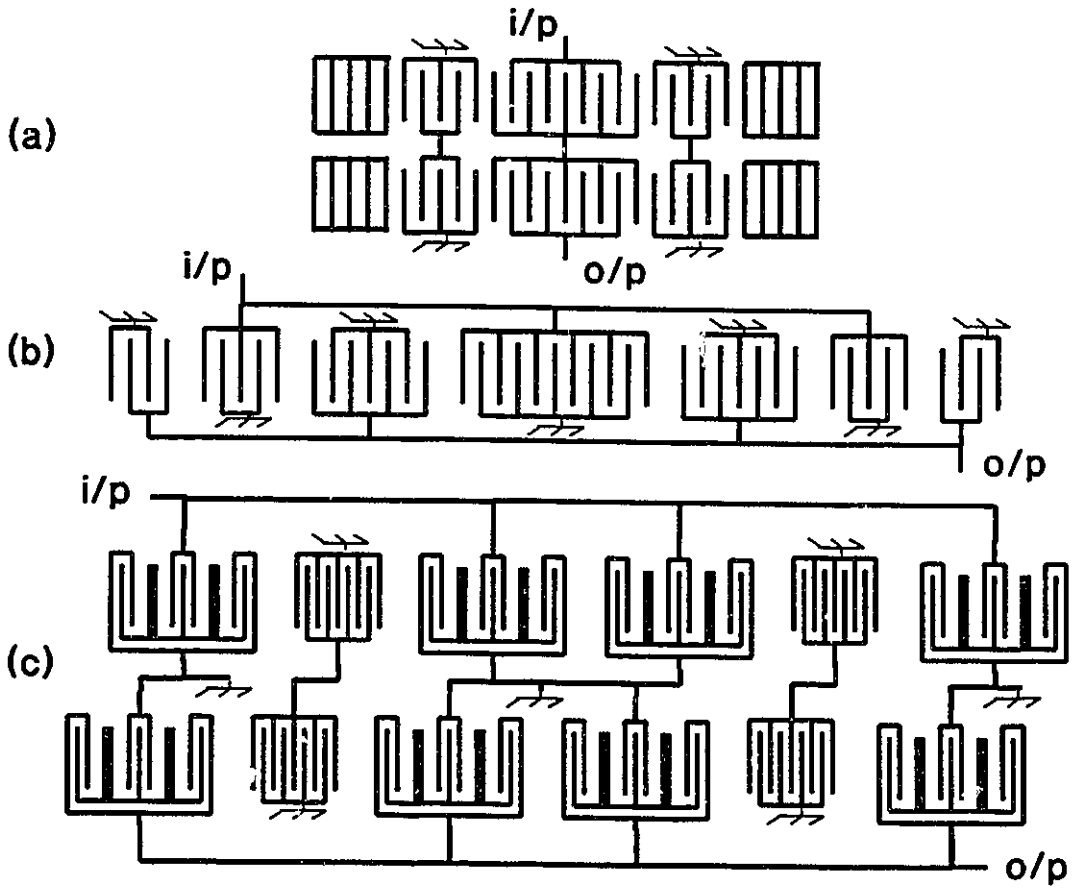

Figure 6.1 Structural layout of (a) DMS filter, (b) IIDT filter and (c) IIC filter.

Figure 6.2 illustrates the radiation conductance for both the input and output IDT of the leaky-DMS filter. Both responses are centred at 86.25 MHz, with the input IDT having N_{pair} = 9.5 and the output IDT having N_{pair} = 16.5 finger pairs.

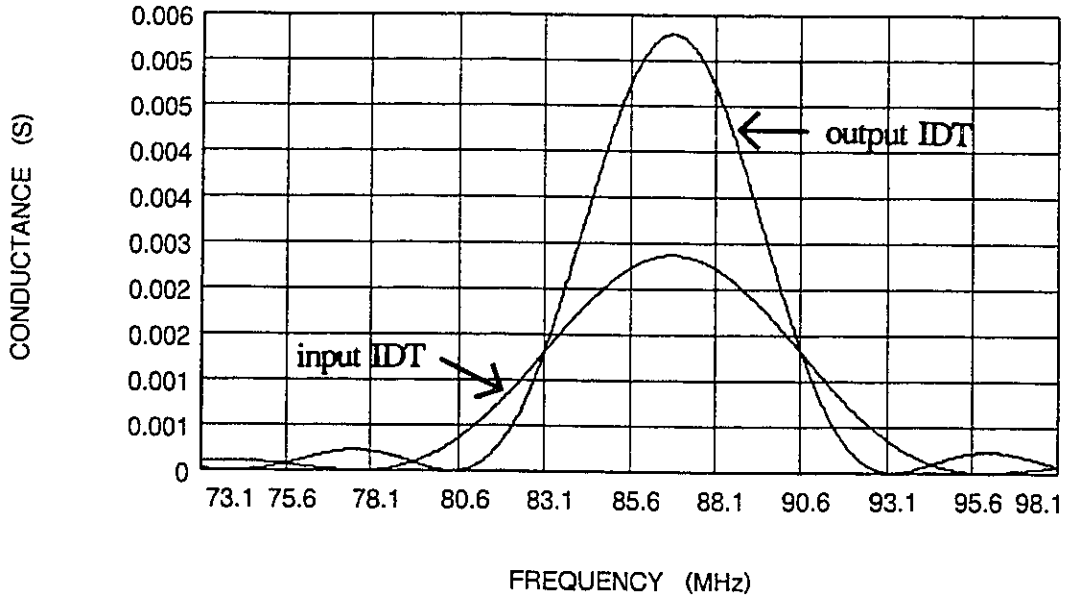

Figure 6.2 The theoretical plot of both the input and output IDT's radiation conductance. The higher curve is that of the output IDT with more finger strips (31).

The new effective radiation conductance G_{eff} , that will compensate for the internal finger reflections, is derived by simply multiplying the normal non-reflective radiation conductance G_a from eqn (6.1), by a shape factor first reported by Uno [43], as

$$G_{eff} = G_a \cdot ShapeUno \ . \qquad (6.2)$$

The ShapeUno factor is a modification to the COM equations of Cross and Schmidt [45] to provide for the leaky-SAW propagation and IDT reflection characteristics above the Bragg frequency. Equations (6.3) through to (6.9) derive this ShapeUno function.

The frequency deviation for narrow-band approximations about the centre frequency f_o is,

$$deltaUno = 2 \cdot \pi \cdot (f - f_o) \cdot \frac{10^6}{v_o} \quad . \qquad (6.3)$$

This frequency deviation must then be modified to include the effects of the film-thickness ratio of the metal strips and for the leaky substrate material, 64° Y-X $LiNbO_3$. The coupling parameter $\varkappa = \varkappa_{12}$ is then modified [41] as,

$$\kappa_{12} = (0.0091 + 0.48 \cdot Filmratio) \cdot (\frac{2 \cdot \pi}{\lambda_o}) \quad , \qquad (6.4)$$

and the velocity shift parameter K11 also from [41] as,

$$K11 = [(0.052 + 0.18 \cdot Filmratio) + 1.4 \cdot (Filmratio^2)] \cdot (\frac{2 \cdot \pi}{\lambda_o}) \quad , \qquad (6.5)$$

to produce the final frequency deviation term Unobeta as,

$$Unobeta = \sqrt{(deltaUno + K11)^2 - (\kappa_{12})^2} \quad . \qquad (6.6)$$

A plot of Unobeta is shown in Fig. 6.3 that is centred about 86.85 MHz.

The work of Plessky and Hartmann [47] and [48] has shown that, above the grating stopband, the leaky-SAW energy at different localization depths has different amplitudes. This affects the attenuation of the leaky-SAW above the Bragg frequency. To compensate for this increase in attenuation an empirical change to the frequency deviation function Unobeta is performed as,

$$Puno = \frac{Unobeta - (deltaUno + K11)}{\kappa_{12}} \quad . \tag{6.7}$$

Figure 6.4 illustrates the results of eqn (6.7).

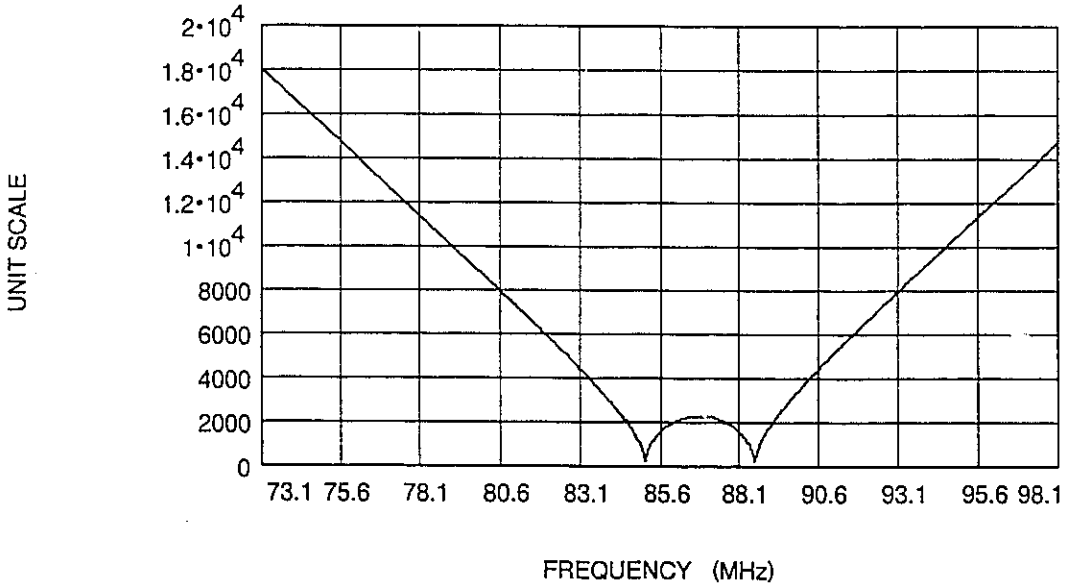

Figure 6.3 Plot of the modified frequency deviation Unobeta.

The transit angle, θ_t from eqn. (89) of Cross and Schmidt [45] is used in the calculation of the sinc function to derive the radiation conductance shown previously in eqn. (6.1). The function, Unotheta is the modified transit angle derived as,

$$\boldsymbol{Unotheta = \frac{Unobeta \cdot N_{pair}\ \lambda_o}{2}} \quad . \tag{6.8}$$

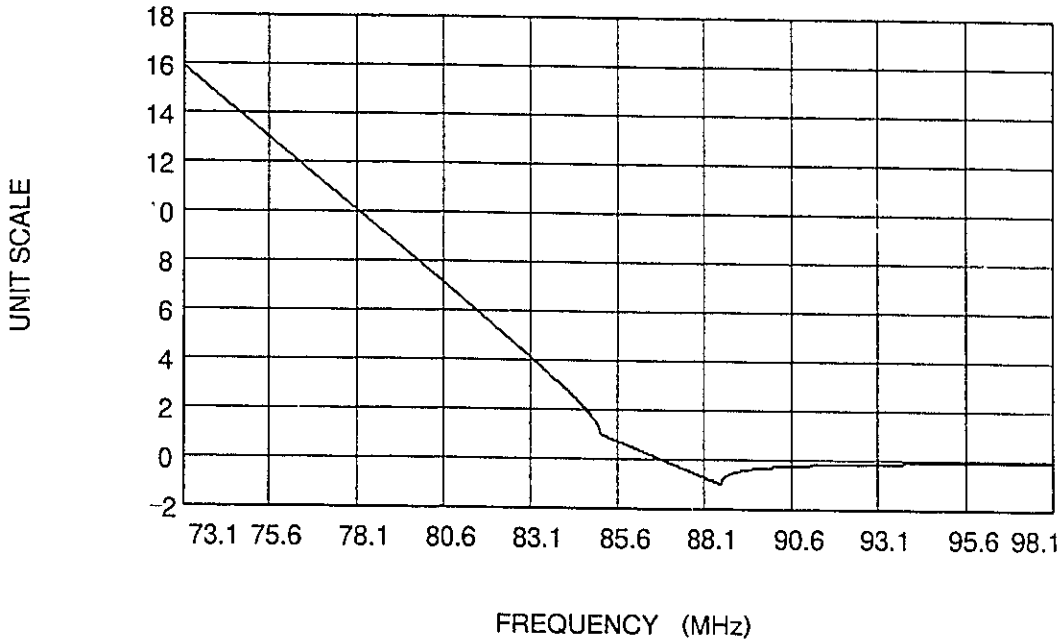

Figure 6.4 Plot of the modified frequency deviation Puno to account for the higher attenuation above the Bragg frequency.

The ShapeUno factor can then be derived using the above Puno and Unotheta functions, from Uno and Jumonji [46],

$$ShapeUno = \left[\left| \frac{1 + Puno}{e^{(j \cdot Unotheta)} + Puno \cdot e^{(-j \cdot Unotheta)}} \right| \right]^2 \quad . \qquad (6.9)$$

Figure 6.5 illustrated the Shapeuno function for both the input (N_{pair} = 9.5) and output (N_{pair} = 16.5) IDTs.

The results of the effective radiation conductance defined by eqn. (6.2) are shown in Fig. 6.6 for both the input and output IDTs. The G_{eff} has shifted down in frequency due to the internal reflections of the IDTs. The fewer the number of fingers, (as in the input IDT, N_{pair} = 9.5), the greater the frequency shift of the peak. This positioning of

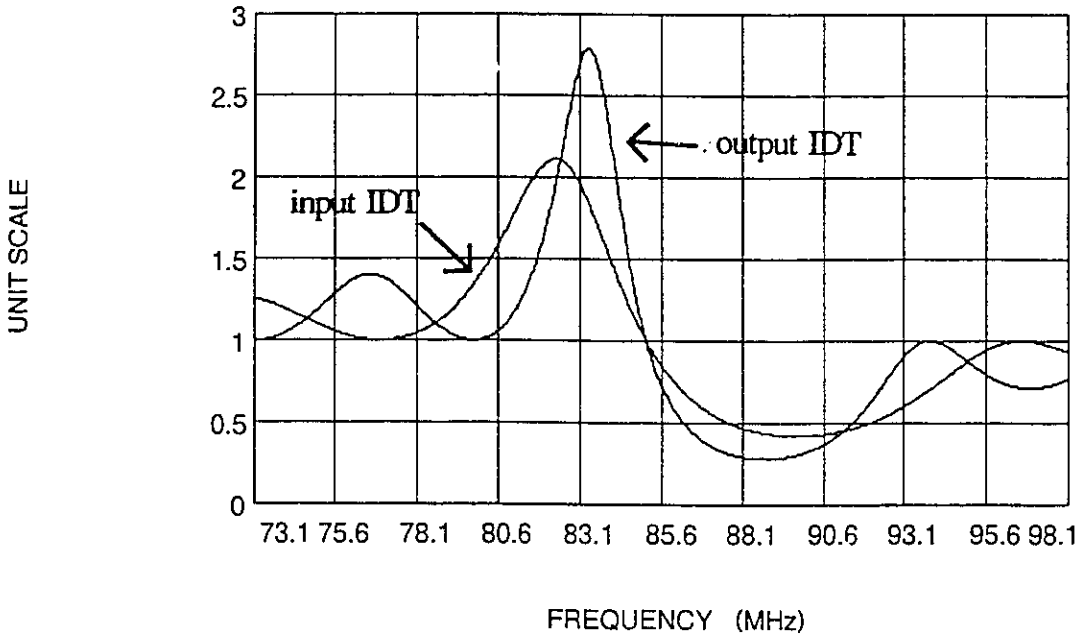

Figure 6.5 ShapeUno functions for the input IDT (lower peak) and output IDT (higher peak)

the peak with respect to frequency can be illustrated by observing the reflection coefficient of the IDT. The peak of the ShapeUno function follows the first null of the reflection coefficient as illustrated in Figure 6.7. At low film-thickness ratios this null is pushed very far down in frequency. At higher film-thickness ratios the null pulls in closer but is still offset down from the centre frequency.

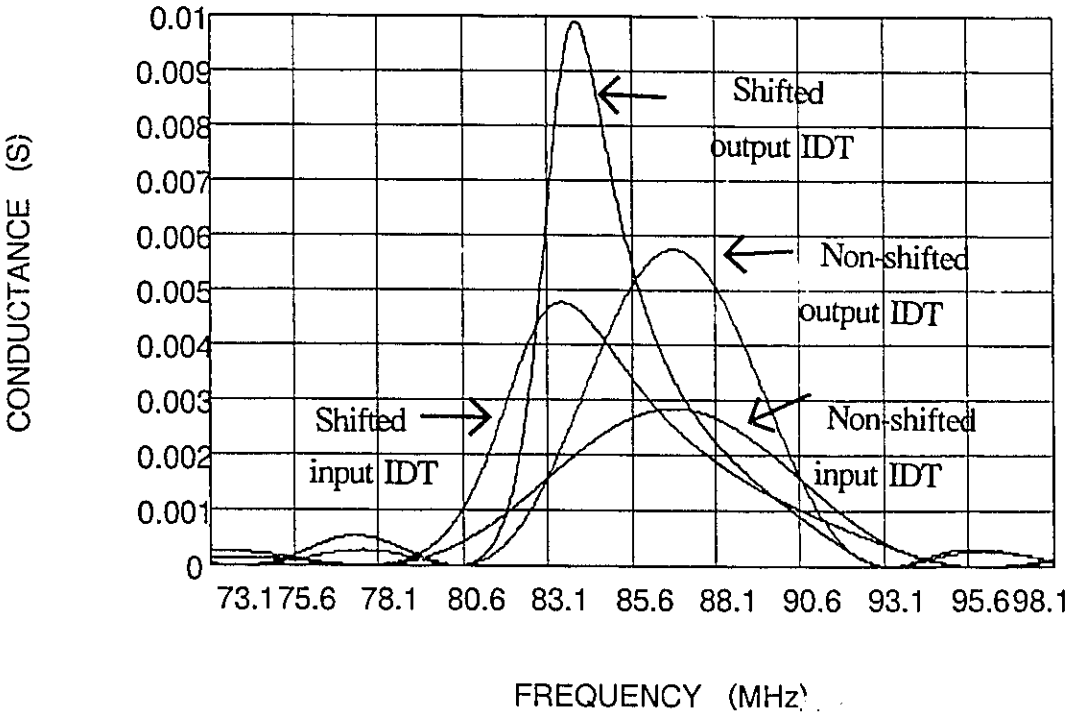

Figure 6.6 Modified theoretical radiation conductance due to finger reflections for both input and output IDTs compared with non-shifted radiation conductance.

An alternative method of calculating the effective radiation conductance G_{eff} is by applying phased-array antenna theory [11]. The parameter N_{pair} of the IDT, relates to the number of elements in the phased array while the frequency response of the IDT is related to the spatial pattern of the antenna beam and sidelobes. A full description of this alternate method is described in the authors' paper [11] and reproduced in its entirety in Appendix C of this thesis.

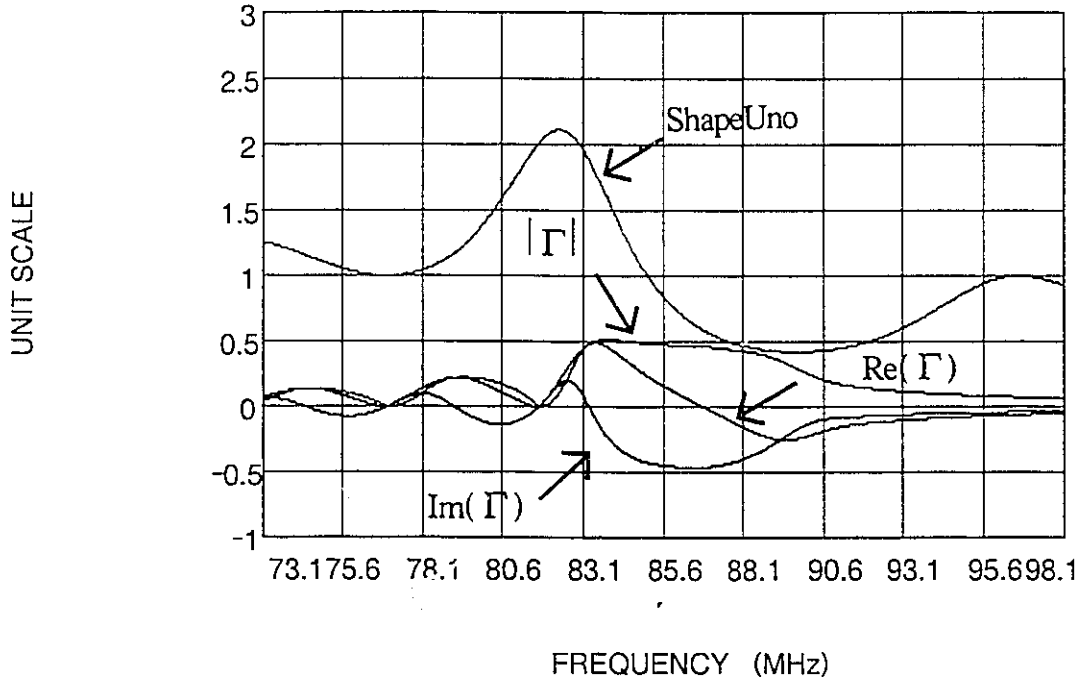

Figure 6.7 A plot of the ShapeUno function and the components of the input IDT reflection coefficient.

6.3 Modification to the Reflection Coefficients of Leaky-SAW Structures

The grating parameters have a major influence on the frequency response of the leaky-SAW resonator-filter. The radiation conductance, discussed previously, shifted down in frequency when the internal finger reflections of each IDT was considered. One other aspect of the reflection coefficient to be considered is the increased attenuation above the reflection stopband [47]-[48]. This increased attenuation is evident in the Fig. 6.7, where the sidelobes on the higher frequency band above the Bragg frequency are greatly reduced.

A derivation of a 2 x 2 transmission matrix using the COM theory was accomplished by Cross and Schmidt [45] to account for the SAW reflections within periodic grating structures using shallow groves. A modification to the parameters of the matrix will allow this fundamental COM theory to be expanded for leaky-SAW structures. Using this approach, the transmission matrix for a reflection grating is [3], [43],

$$| G | = C \cdot \begin{vmatrix} G_{11} & G_{12} \\ G_{21} & G_{22} \end{vmatrix} , \tag{6.10}$$

with the elements

$$G_{11} = \left(\frac{\sigma}{\kappa_{12}} + j(\frac{\delta - j\alpha}{\kappa_{12}}) \cdot \tanh(\sigma L) \right) \cdot e^{j\beta L} , \tag{6.11}$$

$$G_{21} = -je^{j\theta} \cdot \tanh(\sigma L) \cdot e^{-j\beta L} , \tag{6.13}$$

$$G_{12} = je^{-j\theta} \cdot \tanh(\sigma L) \cdot e^{j\beta L} , \tag{6.12}$$

$$G_{22} = \left(\frac{\sigma}{\kappa_{12}} - j(\frac{\delta - j\alpha}{\kappa_{12}}) \cdot \tanh(\sigma L) \right) \cdot e^{-j\beta L} , \tag{6.14}$$

where

$$\sigma = \sqrt{\kappa_{12}^2 - (\delta - j\alpha)^2} \tag{6.15}$$

$$\delta = 2 \cdot \pi \cdot (f_n - f_o) \cdot \frac{10^6}{v_o} + K11 \tag{6.16}$$

with, α = attenuation constant (cm^{-1}), L is the length of the reflecting structure (cm), β = ω_0 / v_0 , is the unperturbed phase constant (rad/cm) and θ = reference phase. The coupling coefficient κ_{12} and the velocity shift parameter K11 are modified to account for the film-thickness ratio of the electrodes as previously shown in eqns (6.4) and (6.5).

The reflection coefficient is defined from the grating parameters as

$$\rho = \frac{G_{21}}{G_{11}} \quad . \tag{6.17}$$

Figure 6.8 illustrates the three different reflection coefficients for the input and output IDTs and the reflection grating for a **non-leaky-SAW** structure. The reflection grating was offset downwards in frequency by about 2.5% from the centre frequency of the IDTs to compensate for the downward shift of the radiation conductance of the IDTs. The sidelobes appear on each side of the Bragg frequency as the attenuation parameter α remains constant.

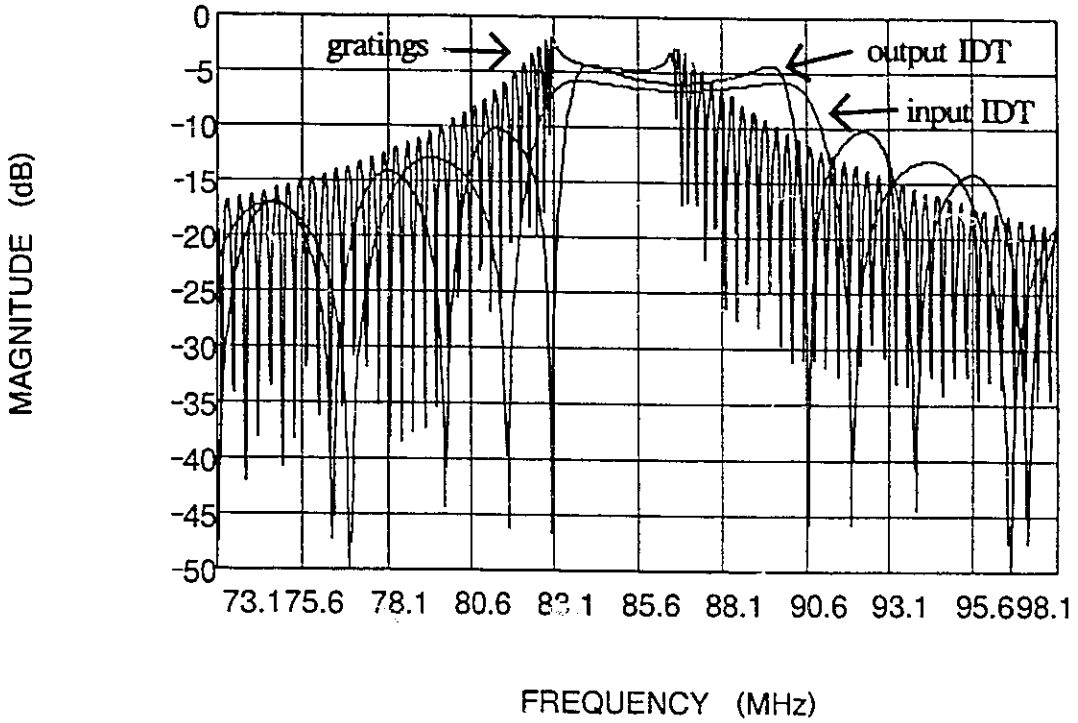

Figure 6.8 Illustration showing both the input and output IDT's calculated reflection coefficient. The grating's reflection coefficient is offset downward in frequency.

The attenuation constant α was then modified to account for the changes for the leaky-wave propagation characteristics [49]-[53]. Below the stopband frequency of the grating structures, these characteristics such velocity dispersion, scattering, reflection and attenuation remain constant. Above the stopband frequency the leaky-SAW effect will modify the amplitude response by the addition of bulk-wave scattering. Both the leaky-SAW and the bulk shear-waves have similar velocities. Above the Bragg frequency there is a conversion of leaky-SAW to bulk shear-waves within the substrate, this increases the grating attenuation constant and modifies the above equations to produce a smoother more attenuated response [47]-[48]. Figure 6.9 illustrates this effect on the reflector gratings

with 251 shorted reflectors, also shifted down in frequency, input IDT "gratings" with N_{pair} = 9.5 and output IDT "gratings" with N_{pair} = 16.5 .

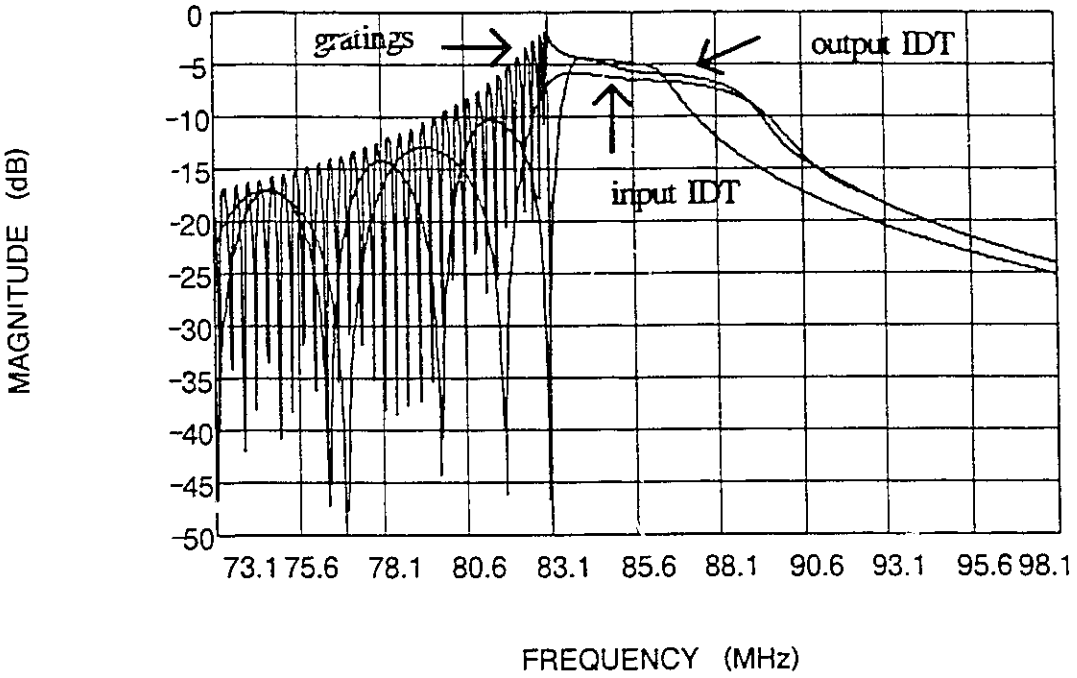

Figure 6.9 The effect on the calculated reflection coefficent of the increased attenuation due to leaky-SAW conversion into bulk shear-waves above the Bragg frequency.

6.4 Scattering Parameters

The effects of the leaky-SAW above the grating stopband also modifies the scattering matrix that is required to compute the IDT matrix elements. The phase response above the Bragg frequency of a leaky-SAW reflection grating will also differ from that of ordinary SAW propagation. Plessky has reported [44], that for shear-horizontal-type SAW propagation in periodic gratings the phase of the reflection coefficient is not $-\pi/2$ at the centre (as for SAW gratings with open metal strips at a $\lambda/8$ reference axis), but

approaches -π/4 at mid-band. Plessky made these observations for grooves, *open* metal strips and dielectric strips. The modified acoustic reflection coefficient S_{11}, the acoustic transmission coefficient S_{21} and the acousto-electric conversion factor S_{13} are shown in the following three equations (6.18-20) respectively.

$$S_{11} = Re(\rho)^2 + \left(- \frac{G_{eff}}{Y_t} \cdot \sqrt{1 - |Im(\rho)|^2} \right) \cdot e^{-jN\frac{\lambda}{4}\delta} , \qquad (6.18)$$

$$S_{13} = \frac{\sqrt{2 \cdot G_{eff} \cdot (1 - |Im(\rho)|^2) \cdot Y_L \cdot e^{-jN\frac{\lambda}{4}\delta}}}{|Y_t|} , \qquad (6.19)$$

$$S_{21} = \sqrt{1 - |S_{13}|^2 - |S_{11}|^2} \cdot e^{-jN\cdot\frac{\lambda}{4}\cdot\delta} , \qquad (6.20)$$

where the reflection grating reflection coefficient ϱ and the radiation conductance G_{eff} are derived in the previous eqns (6.17) and (6.2) respectively and the number of strips N = 2 x N_{pair}. Y_L is the load admittance and $Y_t = (Y_L + 1/ Z_{in})$, where Z_{in} is the IDT input impedance. Figure 6.10 illustrates the three scattering parameters from the above equations, across the frequency range of study. For this study, only the leaky-SAW components will be considered and the sum of the S-parameters ($S_{11}^2 + S_{21}^2 + S_{13}^2$),

should equal unity across the frequency range, if all the parameters have been correctly chosen, as displayed in Fig. 6.10 showing a flat line at the unity value.

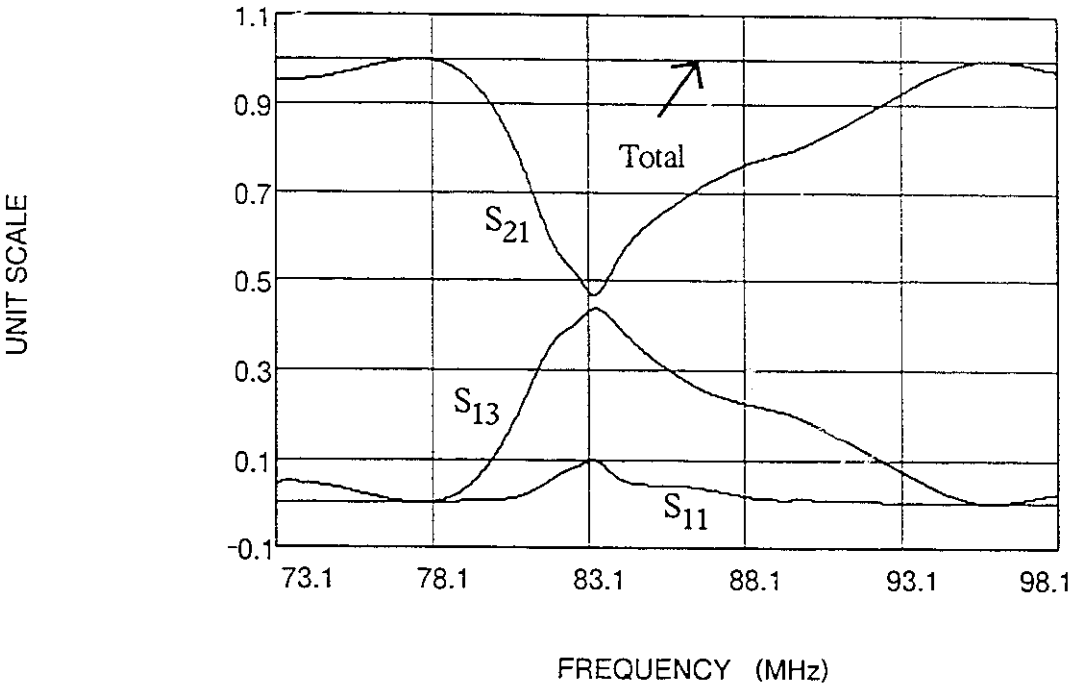

Figure 6.10 Calculated scattering parameters for the input IDT.

6.5 Experiment

Three sets of DMS filters were constructed at a centre frequency of 85.6 MHz following the fabrication procedures outlined in Appendix A. Each set had a modification of a critical parameter that produced prominent changes.

6.5.1 Gap Separation

As referred to previously, Plessky [44] modified his phase shift parameter for *open* metal strips to a value $\approx -\pi/4$ at midband. For these sets of experiments, *shorted* metal strips were utilized. To compound this problem of selecting a correct phase shift parameter the resonator cavity has been changed from normal periodic strips (modelled as open for the IDTs and shorted for the gratings) to some strips that are touching in the IDTs as previously shown for a DMS in Fig. 2.9 when dt = 0. This change will affect the $\lambda_o/8$ reference axis offset from the metallized strip edges, chosen for each COM matrix [3] as shown in Fig. 6.11. The important geometric parameters are then the two spacings dt and dg, (with reference to Fig. 2.9 and Fig. 6.11), for the IDT and grating separation respectively. Figure 6.12 illustrates both the theoretical and measured responses when the parameters of Table 6.1 are implemented.

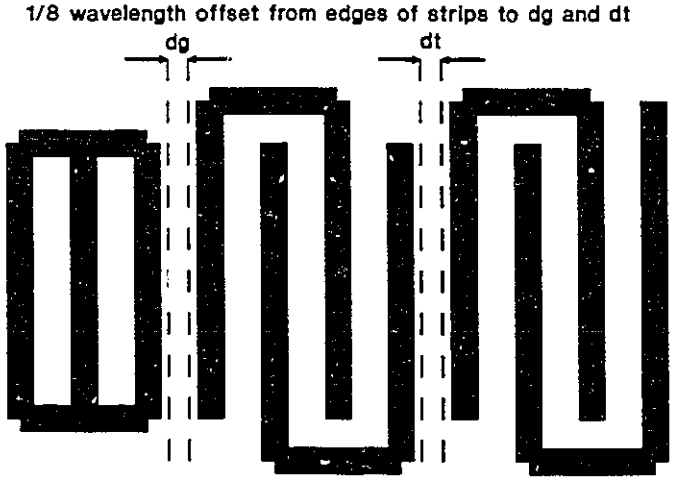

Figure 6.11 Diagram to illustrate the $\lambda_o/8$ reference axis offset from the metallized strip edges.

The theoretical prediction accurately represents the behaviour of the device. The amplitude levels and position of the sidelobes indicated that COM model was reasonable with the exception of an improper choice of an unknown parameter that failed to produce a normally flat passband response. The extremely low insertion loss (IL) of about 1.39 dB demonstrates that the leaky-SAW has, when compared to Rayleigh waves, a stronger coupling to the electric fields [44]. Figure 6.13 illustrates two identical electrically-cascaded filters that again exhibit a low IL of approximately 3.9 dB.

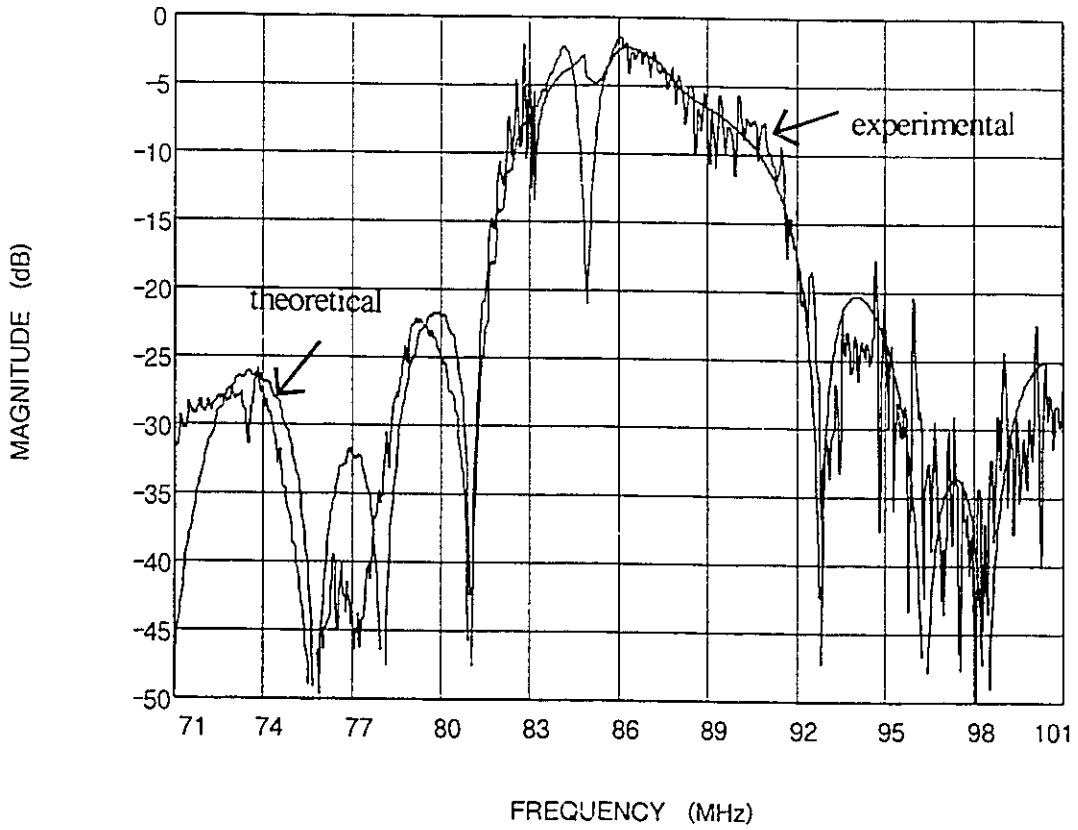

Figure 6.12 Both the theoretical and experimental frequency response of a single leaky-SAW resonator filter.

Table 6.1

Design parameters for the leaky-SAW devices fabricated at McMaster University

Parameter	Actual Values
Substrate	64^{o} Y-X $LiNbO_3$
Velocity of leaky wave	4742 m/s
Centre frequency	92.4 MHz
Wavelength (λ_o)	51.32 microns
Aperture width	40 λ_o (2.05 mm)
Film-thickness ratio (h/λ_o)	0.4 % (2050 Angstroms)
Number of reflectors (each end)	251
Number of IDT strips (input # , output #)	(19, 31)
Spacing between IDTs (dt)	-0.25 λ_o (12.83 microns)
Spacing between IDT and reflectors (dg)	0.25 λ_o (12.83 microns)

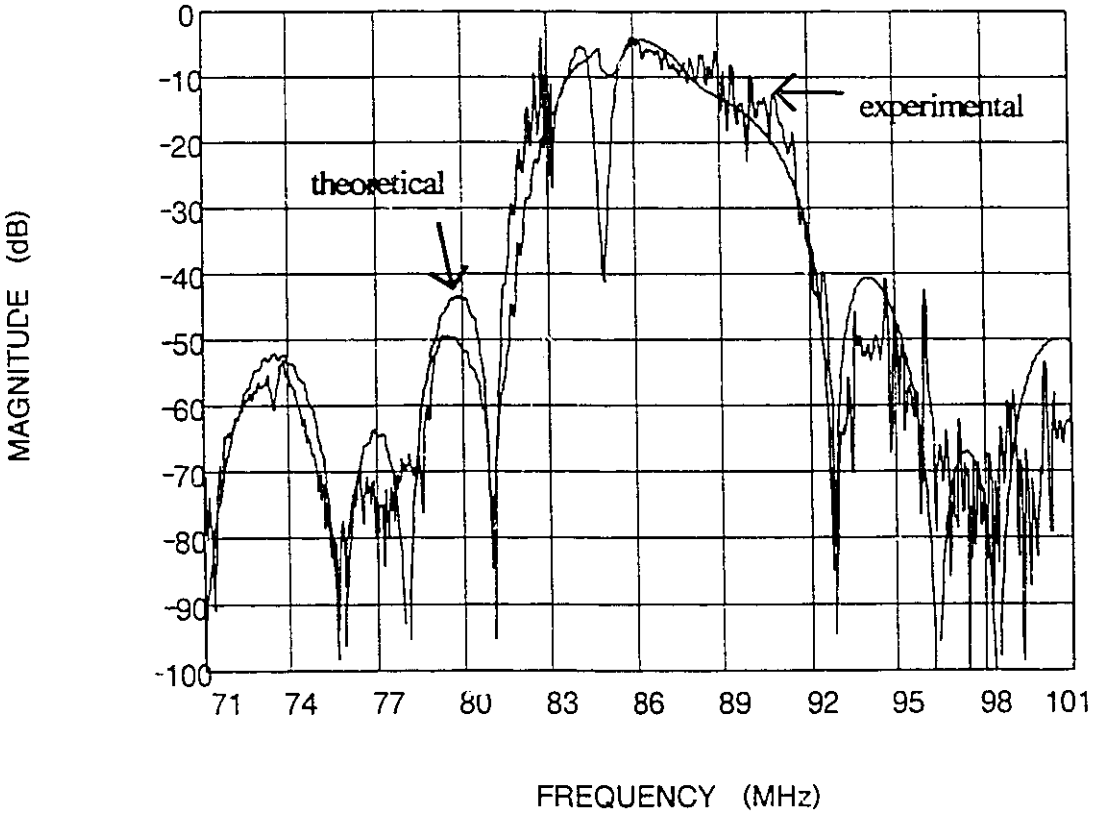

Figure 6.13 Both the theoretical and experimental frequency response of two single leaky-SAW resonator filters in cascade.

6.5.2 Gap-Separation Modification

The solution of the "notch" response was found by adjusting the phase-shift term for the grating structures of the scattering parameter equations of (6.18,20). A second device was constructed with the exact parameters of Table 6.1 with the exception of the gap distance dg. The previous mask for device #1, had the total edge-to-edge distance d $= \lambda_o /8 + dg + \lambda_o /8 = 0.5\ \lambda_o$.

Device #2 was modified to account for the different phase shift parameter, by changing dg = $0.375\lambda_o$ and introducing a phase-shift-reduction parameter of $3\lambda_o/8$ to compute the distance dg = $\lambda_o/8 + dg + \lambda_o/8 - 3\lambda_o/8 = 0.25\,\lambda_o$. The results of this successful bandpass circuit can be observed in Appendix C. Figures 5 and 6 of Appendix C show the theoretical and experimental results for both a single and two cascaded filters respectively.

6.5.3 Film-Thickness Ratio Modification

The final modification to be tested is to maximize the bandwidth of the resonator filter. Morita [41], states that for optimum-mode splitting, the main two critical parameters are, the distance between IDTs dt = $-0.25\,\lambda_o$ and the film-thickness ratio h/λ. Device #3 was then constructed with the same mask as was used for device #2 with the exception that the film-thickness ratio was now $h/\lambda = 3\%$. Figure 7 of [11] illustrates the improved passband response with both the theoretical and experimental results. Figure 6.14 illustrates the predicted response of the *first* and *third* modes within the DMS resonator filter. These two modes differ by their phase with respect to each other by $\pi/2$ rad. They are simply added together to obtain the final response. The high sidelobes in both of the modes at about 90.6 MHz are attributed to the distortion of the radiation conductance due to the internal reflections of the IDTs. A wideband theoretical and experimental response of the same filter is shown in Fig 6.15. The experimental waveform had higher far-out sidelobes due to electro-magnetic feed-through between the connectors.

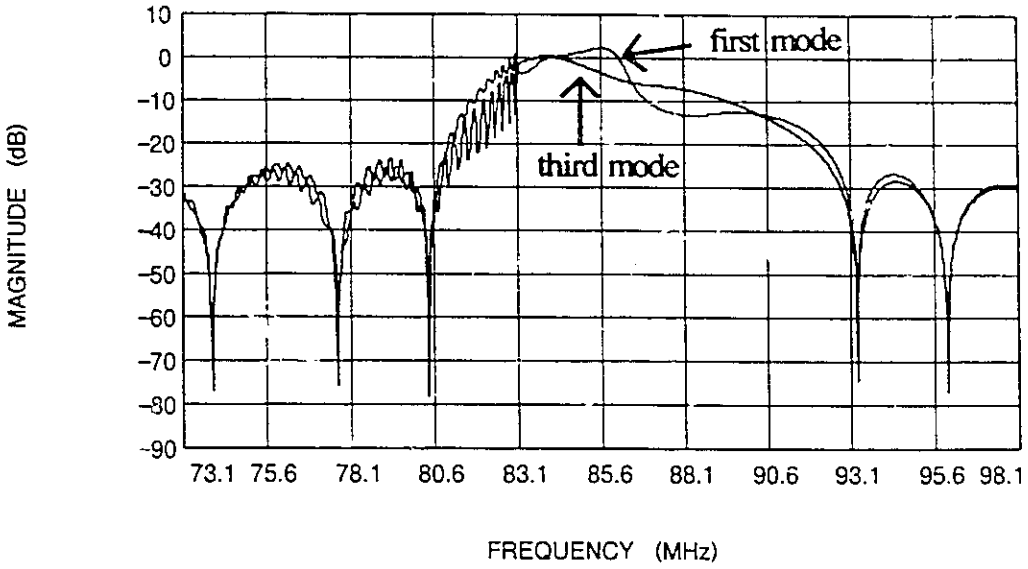

Figure 6.14 Predicted uncorrected response of the *first* and *third* modes within the DMS resonator filter. The *first* mode has the higher amplitude peak at the higher frequency.

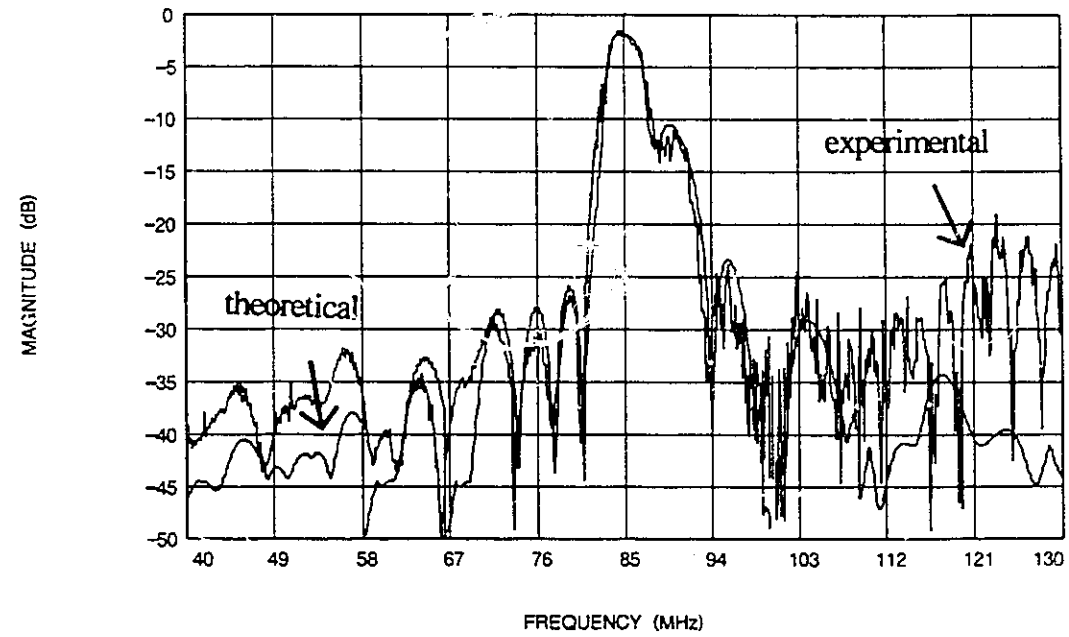

Figure 6.15 A wideband theoretical and experimental response of device #3.

6.5.4 Group Delay and Impulse Measurements

The group delay of a DMS resonator filter provides insight to any possible phase distortion that a channel within the passband will acquire. A flat group delay within the passband will minimize the phase jitter of a digital signal [21]. The impulse response is also helpful in the verification of propagating modes on SSBW and leaky-SAW substrates [54]. The calculated group delay of Fig. 6.16 illustrates the relative flatness near centre frequency and increasing values near the edge of the upper band. These small peaks at the edges of the passband are due to the impedance mismatch that is beginning to occur at the extremities of the Bragg frequency.

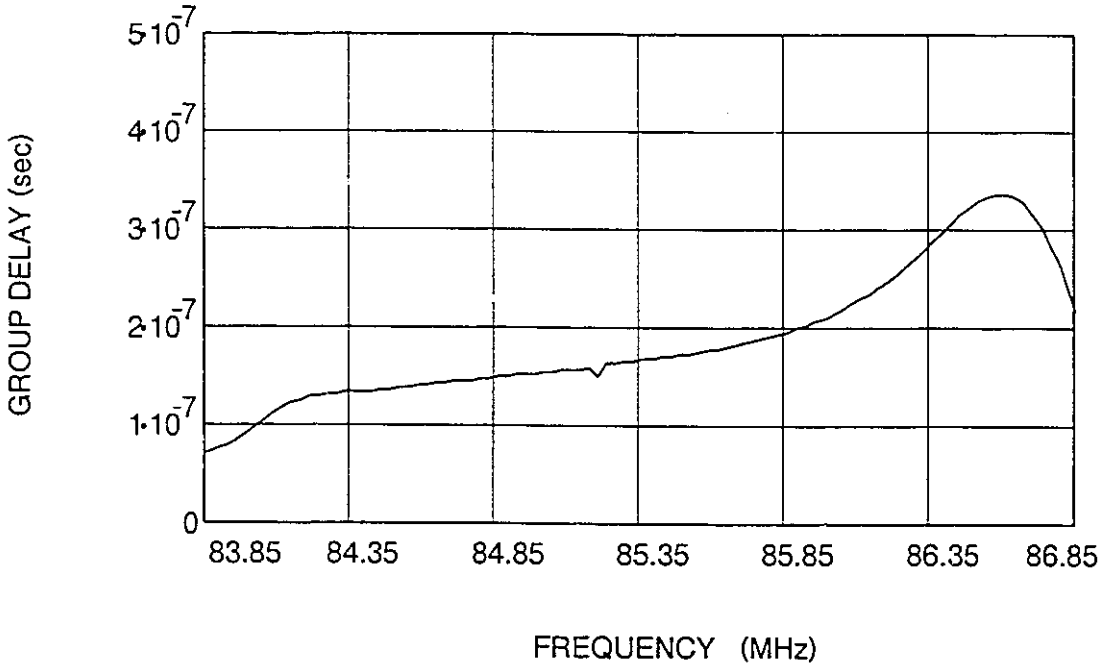

Figure 6.16 Predicted group delay of device #3.

The measured group delay was performed on a Hewlett Packard Network Analyzer, HP-8505A and is displayed in Fig. 6.17. The limits of the delay (about 120 ns) match reasonably well with Fig. 6.16.

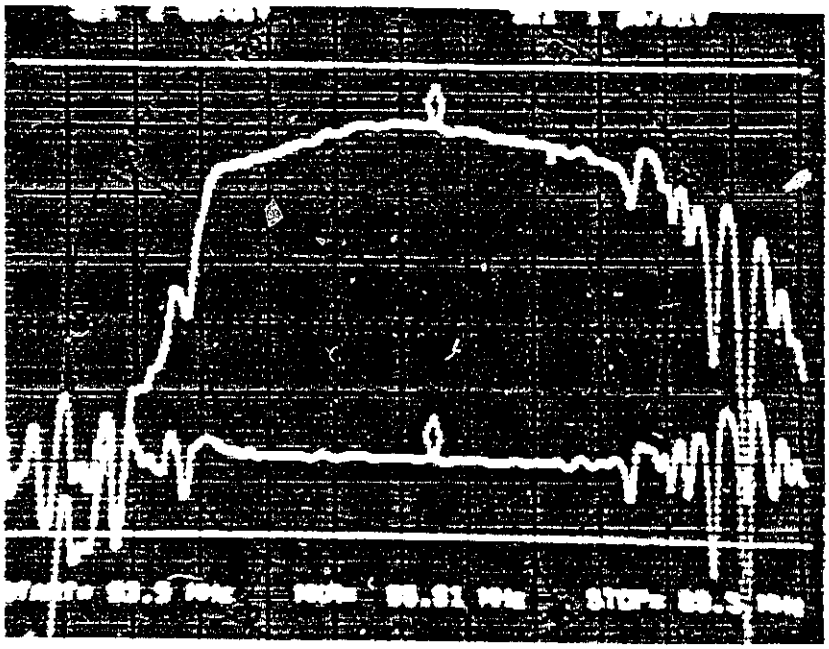

Figure 6.17 Measured group delay of device #3 (lower trace). Horizontal scale, start 83.5 MHz, stop, 89.5 MHz; vertical scale is 100 ns / div.

The final test was to measure the impulse response using a Hewlett Packard model HP 8510 network analyzer displayed in Fig. 6.18. The main impulse peak of 121.74 ns should be compared to the flat line of Fig. 6.17 of approximately 120 ns. This peak can be approximated by the amount of time the leaky-SAW wave takes to travel from the

centre-to-centre distance between the IDTs. Since finger reflections are considered in the calculation of the IDT radiation conductance, these reflections in effect reduce the distance travelled by the leaky-SAW and in effect reduce the delay time . The second impulse peak of Fig 6.18 at approximately 250 ns represents the time of travel into the reflectors and back to the IDTs.

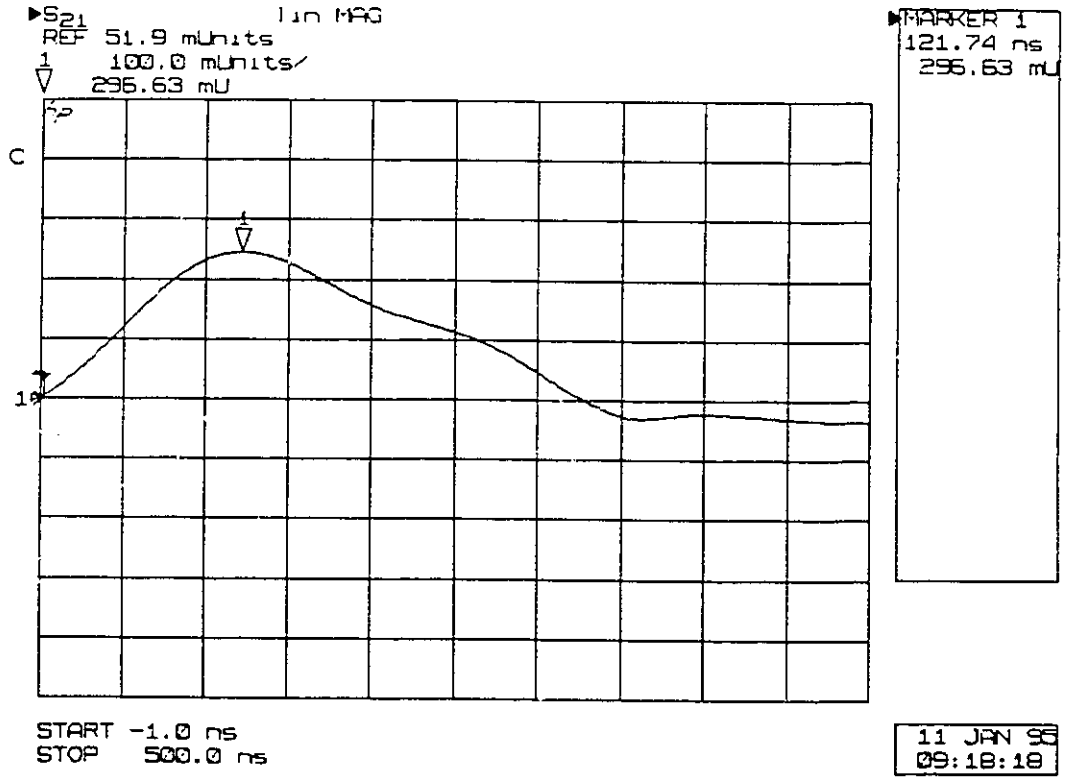

Figure 6.18 Impulse response of a single DMS leaky-SAW resonator filter. Horizontal scale, 50 ns / div; vertical scale, 100 milliunits / div.

CHAPTER 7

SUMMARY AND CONCLUSIONS

7.1 Summary

This thesis has presented a study of coupling-of-modes effects on both oscillator systems and resonator filters that utilized the surface acoustic wave phenomena. It was shown that the versatility of the applications due to these effects are numerous and atypical.

Part I of this thesis, incorporating Chapters 3, 4 and 5, dealt with the coupling effects of injected SAW oscillators. Chapter 3 described the condition of an oscillator constructed with an 85-MHz SAW SPUDT device as the feedback element of an amplifier. This oscillator had an input signal injected into the feedback loop, which could be up to 4 or 5 orders of magnitude smaller than the output of the free-running oscillator. The amazing phenomenon is that if the stability of the injected signal is superior to that of the oscillator, then the oscillator will track and eventually lock onto this signal. This phenomenon is referred to as an injection locked oscillator and is very similar to that of a phase locked loop. A SAW device with a lower quality factor in the feedback loop would produce an unstable free running oscillator output signal. The lower the quality factor the faster the signal will reduce in amplitude due to its damped response. If the injected signal can maintain its damped signal within the loop longer than the SAW then

the higher quality signal will be sustained within the loop. The applications of this condition can pertain to tracking a signal and therefore amplifying it by 4 to 5 orders of magnitude. To the best of the author's knowledge this work was the first to incorporate SAW devices in this configuration to reproduce both single and multiple neural conditions.

The approach in Chapter 4 was to modify both the quality factor of the SAW device and to limit the injected signal within the oscillator loop. These conditions prevent the oscillator from achieving a locked condition and retains the circuit in the vicinity of lock-in. The higher quality factor STW resonator at 1012 MHz replaces the lower quality factor SAW SPUDT as the feedback element. The phase conditions of the loop were then studied to observe that, with a locked condition the phase difference between the injected signal and the output of the oscillator was $\pm \pi/2$, depending on whether the frequency of the injected signal was above or below the free running frequency of the oscillator. By observing this phase slope, the circuit provided a form of memory to test whether the previous injected signal was above or below a certain threshold. This technique was then expanded to provide a carrier-recovery circuit for BPSK signals without any phase ambiguity problems. The concept of observing the frequency difference between the injected signal and the oscillator output produced the idea of an analog-to-digital converter. This difference frequency changes from the original maximum difference to zero as the injected signal is increased to a locked condition. A frequency counter connected to the loop then tracks this change of frequency with respect to the injected signal.

The single neuron circuit of Chapter 3 was expanded for Chapter 5, by adding substantial non-linearity to the loop amplifier and an additional output amplifier. This resulted in a dynamical system that can be studied using Chaotic theory. Massive period doublings were observed as the injected stimulus was increased, that produced an intermittent pulse before the system collapsed to a lock condition.

Chapter 6 encompassed the whole of Part II and was a treatise on dual-mode leaky-SAW resonator-filters. These were fabricated on 64° Y-X $LiNbO_3$ substrates and produced a very low insertion loss of 1.39 dB with approximately 3 % bandwidth. These exceptional achievements are due to the large electro-mechanical coupling coefficient of the leaky-SAW. The coupling-of-modes reflection-grating equations and the IDT S-parameters were modified to cater for the increased attenuation above the Bragg frequency. This chapter studied the irregular phase-response mechanisms associated with the leaky-SAW reflection gratings utilizing shorted-metal strips.

7.2 Conclusions

The novel circuits and devices that were investigated in this Thesis were all dependent on the coupling-of-modes theory. This technique expanded the use of simple ILOs into dynamic, memory-oriented, decision capable circuits. For the leaky-SAW resonator-filters, the modified COM equations provided insight into their behaviour. The analytical COM model provided excellent theoretical agreement with the measured data in all of the experiments completed within the scope of this Thesis.

APPENDIX A

FABRICATION OF DEVICES

A.1 Substrate Preparation and Metal Deposition

Once a design has been finalized, the construction of the surface wave device begins. These devices are a simple form of thin film planar electronics and can be readily fabricated using conventional photolithographic techniques.

As previously mentioned in Chapter 2, a SAW device demands a suitable metal conductor deposited onto a piezoelectric substrate. The essence of a good durable SAW device begins with a fastidious treatment of the substrate to ensure proper adhesion with the metal conductor.

The substrates were purchased from a supplier, Crystal Technology of Palo Alto, California, and delivered as three-inch (75 mm) diameter wafers with a thickness of 0.020 inches. The wafers have two distinct features about them. First, they are not perfectly circular, but instead have a "flat" cut across an edge. This is to indicate the orientation of the propagation axis that must be considered when fabricating the device to ensure lower second order effects. Secondly, one side of the wafer appears smoother and polished compared to the other. This polished side is the top side of the device where the metal conductors are placed. The rough side is fixed down on to a suitable package and will assist in scattering and suppressing bulk waves.

The following steps will outline the procedures required to fulfil the requirements of the substrate preparation and metal deposition. It will be assumed that in all of these steps, a clean room or at least controlled conditions and proper hand gloves and non shedding clothing attire are used.

1) Dicing of the 75 mm wafer to a suitable substrate size.

This method of cutting the wafer, requires that the wafer be mounted on a slab of insul-brick and attached to the brick with ample amounts of quick-setting liquid glue. The brick is then mounted on the horizontal bed of a cutting saw. Proper alignment with the flat of the wafer to a vertically positioned carbide saw blade is made. The horizontal bed with the brick attached moves through the rotating cutting saw, controlled by an automatic feed. A generous amount of lubricant/coolant is continuously applied over the cutting surface.

2) Substrate cleaning.

The diced substrates, that measure about 25 mm by 12 mm, are removed from the brick by dissolving the glue with acetone. The glue and other contaminating debris are removed by soaking and rinsing with trichloroethylene. A visual inspection with a microscope provides verification that no scratches occurred during the cutting process.

Each substrate then in turn is placed onto a Headway Research Inc. Photo Resist Wafer Spinner and held by a vacuum chuck. Cleaning of the substrate involves flushing the area with various liquids and drying such as;

i) flush with trichloroethylene
ii) spin dry at 4000 RPM for 30 seconds
iii) flush with acetone
iv) spin dry
v) flush with ultra-clean (18 MΩ) water
vi) spin dry
vii) flush with Methanol
viii) spin dry for one minute

The substrate is then carefully removed from the spinner and placed in a clean petri-dish container. This dish is then placed in an oven at 80°C, for any solvent degassing, for at least 30 minutes..

3) Metal Deposition

Depending upon the application either a thin or thick layer of aluminum is deposited onto the substrate. A thin layer is defined as consisting of 0.2 μm or 2000

Angstrom units (Å) and a thick layer is considered greater than 1.0 μm or 10,000 Å. This process takes place within a vacuum, to ensure that the deposition retains good adhesion and little or no contamination. The equipment used to produce a vacuum of approximately 10^{-6} mbar is an Edwards High Vacuum Coating Unit Model 12E3/947 for a thin film and an Edwards High Vacuum Electron Beam Coating Unit, Model E12E, for a thick film. The aluminum is 99.99% pure and is used for two reasons. It is a good conductor with a specific resistance of 17 ohms per mil-foot, compared to copper at 10 ohms. As well, aluminum is lighter in weight than other conductors and minimizes any mass loading effect of the piezoelectric substrate. Figure A.1 illustrates in the foreground the Model 12E3/947 coating unit.

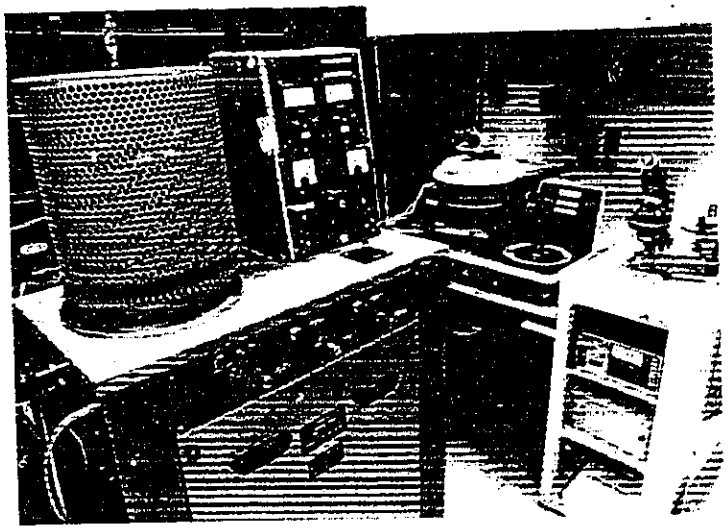

Figure A.1 Photograph of the SAW facilities at McMaster University. In the foreground is a Model 12E3/947 metal deposition unit. In the background is the Kasper 2001 mask aligner.

A.2 Computer Generated Artwork

The circuit pattern that will eventually appear on the aluminum conductor, must first be generated off the substrate by using certain photoreproduction techniques.

The IDTs and reflectors are really geometric patterns that have a set of planar X and Y coordinates, for the thickness Z of the pattern is determined by the conductor thickness. These X and Y positions are determined from the geometrical design by such factors as; finger widths, spacings, number of fingers, aperture and size of the bus bars.

A simplified method of producing the artwork utilized a Auto-Cad package that produces HPGL files that are sent via a storage disk to a commercial photolithography house that returns a twenty times negative of the SAW patterns.

A.3 Mask Photoreduction

The SAW circuit negative is now further reduced 20 times by a Microkon 1700 camera, with a resolution of 200 line pairs and a f stop of 4.0 at 92 mm. The final film is really a 2" x 2" x 0.060" Kodak High Resolution glass plate type 1A. On this plate is transformed a positive photographic circuit called a mask, of the same dimensions as the final electrical circuit. Exposure of the plates is for 18 seconds and processing is as follows;

i) soak in Kodak High Resolution Developer for 45 seconds.

ii) rinse in a distilled water bath.

iii) soak in Kodak plate fixer with hardener for 5 minutes.

iv) rinse under de-ionized water for 5 minutes.

v) air dry for 30 minutes.

A.4 SAW Circuit Generation from a Mask

The mask (2" x 2" glass plate) contains the same geometrical pattern as the final surface wave device. To reproduce this pattern onto an aluminum pattern on the crystal substrate the following procedures are taken.

1) Application of Photoresist onto the Crystal.

The crystal substrate is carefully removed from the oven and placed back onto the spinner. Sufficient drops of prefiltered Shipley Microposit Photo Resist 1400-17, are placed on the crystal. The substrate is then spun for one minute at 4000 RPM to produce a coating of about 2000 Angstroms. A critical post-baking period is required for 30 minutes at 80°C. Since the photoresist is sensitive to all but yellow light, precautions must be taken so not to damage the qualities of the photoresist.

2) Surface Wave Pattern Exposure.

A Kasper 2001 Mask Aligner, shown in fig. A.1, with a collimated Ultra Violet

light source transfers the pattern of the mask onto the photo sensitive coating of the substrate. Exposure is for 13 seconds at a power density of about 4 mW/cm^2. After exposure the aligner ejects the substrate safely to allow further processing.

3) Development of the photoresist.

Areas not exposed to the light source are washed away in the development process, therefore leaving the aluminum uncoated. The substrate is placed in a Shipley Microposit Developer for 40 seconds. The coating is now desensitized and further processes could take place in normal light.

4) Etching of the Aluminum Pattern.

The crystal substrate is placed into an acid etch that is composed of;

25 parts Phosphoric acid	H_3PO_4
5 parts Acetic acid	$C_2H_4O_2$
1 part Nitric acid	HNO_3

The process is slow, taking from 1 to 3 minutes depending upon the freshness of the etch and the thickness of the fingers. Periodic visual checking must take place to ensure that just the proper amount of etching occurs. Too much etching can occur quite rapidly as the surface wave devices within the scope of this thesis had finger widths that varied from about 8 μm to 10 μm. A rinse in water to remove any acid and then a rinse

in acetone to remove the photoresist covering the aluminum. Finally the substrate is flushed with 18 MΩ water for 5 minutes to remove any remnants of acids or other contaminants. The substrate is blown dry with nitrogen and placed in a clean container.

A.5 Packaging of the Device

The substrate at this point has an aluminum circuit on its surface and can be suitably packaged to properly interface with the required electronics. One such package that is well suited for both the size of the substrate and excellent compatibility with the electronics, is the Dual In Line Airpax microcircuit container.

These containers are 3.5 cm x 2 cm x 0.5 cm in size. They only have the four corner pins of a 24 pin configuration (pins 1, 12, 13 and 24) protruding from the package that will be connected to the input, ground, output and ground respectively.

Apiezon vacuum grease provides adhesion between the substrate and container. The grease also absorbs bulk wave interaction occurring at the bottom of the crystal. The interdigital transducers (IDTs) are connected to their pins via # 38 AWG copper wire and held securely with a conductive Silver Print adhesive.

A lid is fixed in place and held by an adhesive. The SAW device is now protected from outside contaminates and Electro Magnetic Interference (EMI).

APPENDIX B

DERIVATION OF THE COUPLING-OF-MODE EQUATIONS AS APPLIED TO INJECTION-LOCKED OSCILLATORS

B.1 Introduction to the Coupling of Waves Study

The concept of two systems coupling to each other is an interesting one. Every undergraduate student who studies physics is introduced to the proposal of *action-at-a-distance* due to both Newton and Coulomb's Laws. The suggestions that one mass or charge could affect another mass or charge without being physically connected and the similarity of the two formulae prompted further study into an area of field theory. The rigor of studying fields in motion would normally break down into three formulations of equations;

(1) the Newtonian, in the analysis of mechanical structures, such as bridges.

(2) the Hamiltonian, in the analysis of quantum mechanics.

(3) the Lagrangian, for the analysis of quantum electodynamics.

There does exist another formulation of equations in the study of motion that is closely related to the Hamiltonian, which is called the *normal-mode form*. For this method, a system of motion can be described by two coupled first-order differential equations.

A simple example will be considered in the development of the *normal- mode form* of the equations of motion. Figure B.1 illustrates an electrical LC oscillator circuit. The Hamiltonian form of the equations of motion for these devices is given by [55]

$$\frac{dI}{dt} = -\frac{1}{L} V \qquad \textbf{(B1.a)}$$

$$\frac{dV}{dt} = \frac{1}{C} I, \qquad \textbf{(B1.b)}$$

where I is the current, V is the voltage, L is the inductance and C is the capacitance.

The Hamiltonian equations of (B1) are comprised of two coupled first-order differential equations. The voltage is coupled to the current parameter in eqn (B1.a) and the current is coupled to the voltage parameter in eqn (B1.b). The coupling coefficients are -1/L in eqn (B1.a) and +1/C in eqn (B1.b). The difference in sign is most significant. A periodic solution exists for cases when the signs are different. For the same signs, the solutions will either decay or grow exponentially.

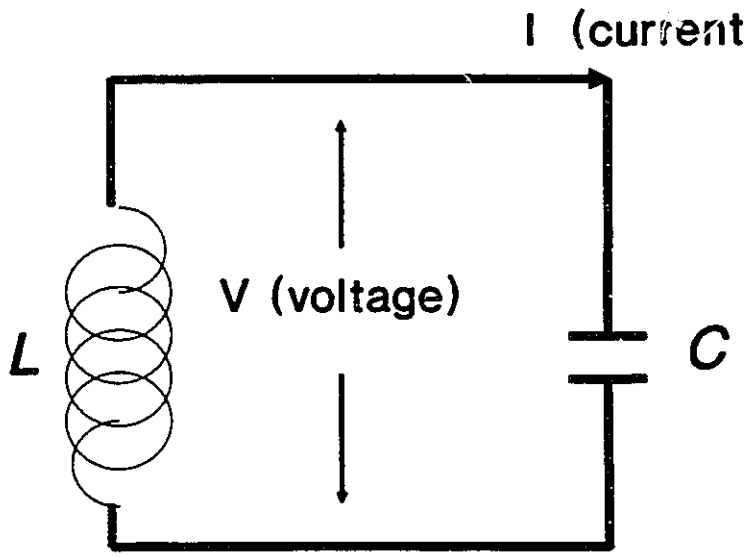

Figure B.1 Simple electrical LC circuit.

An oscillating electrical system has two forms of energy and there is a periodic transfer of energy between the two forms. For the LC circuit the two forms are, magnetic energy ($LI^2/2$) stored in the inductor's magnetic field and electric energy ($CV^2/2$) stored in the dielectric of the capacitor. Following the same analogy for the signs of the coupling coefficients, the energy of the system will periodically transfer between the inductor and the capacitor.

The Lagrangian form of the equations of motion for an oscillating system can be derived by substituting eqn (B1.b) into equ (B1.a). This results in a second-order differential equation known as the Newtonian form of the equations of motion;

$$\frac{d^2V}{dt^2} = -\frac{1}{LC} V \qquad \text{(B2.a)}$$

$$\frac{dV}{dt} = \frac{1}{C} I \qquad \text{(B2.b)}$$

The solution of eqns (B2.a) and (B2.b) involves two arbitrary constants of integration that are usually the initial condition of the current and voltage. Therefore both of equations, (B2.a) and (B2.b) must be used to achieve a proper solution.

Another equal description of Fig. B.1 involves two decoupled first-order differential equations. This is the *normal-mode form* of the equations of motion. To derive this form, a linear combination of the Hamiltonian equations of eqns (B1) is used. Equation (B1.b) is multiplied by an arbitrary constant Y and added to eqn (B1.a) to give;

$$\frac{d}{dt}(I + Y*V) = \frac{Y}{C} (I - \frac{C}{LY}*V) \ . \qquad \text{(B3)}$$

If Y is chosen such that

$$Y = \pm j\omega C \qquad \text{(B4.a)}$$

and

$$\omega = + \frac{1}{\sqrt{LC}} \qquad \text{(B4.b)}$$

then the previous eqn (B3) can now be written as

$$(\frac{d}{dt} - j\omega)a = 0 \qquad \text{(B5.a)}$$

$$(\frac{d}{dt} + j\omega)a^* = 0 \ , \qquad \text{(B5.b)}$$

where

$$a = \frac{1}{2}\sqrt{L}\ (I + j\omega CV) \qquad \text{(B6.a)}$$

$$a^* = \frac{1}{2}\sqrt{L}\ (I - j\omega CV) \ . \qquad \text{(B6.b)}$$

The vector quantities a(t) and a*(t) are referred to as the *normal-mode amplitudes* that are equal in amplitude but rotate opposite to each other. Equations (B5.a and b) are two first-order decoupled equations of motion that can equally describe the events of Fig. B.1. The total energy of the system can be written as;

$$E = \frac{1}{2}(CV^2(t) + LI^2(t)) \qquad \textbf{(B7.a)}$$

$$E = |a(t)|^2 + |a^*(t)|^2 \qquad \textbf{(B7.b)}$$

The solutions of the *normal-mode equations* of eqn (B.5) are

$$a(t) = a(0)e^{j\omega t} \quad , \qquad \textbf{(B8.a)}$$

$$a^*(t) = a^*(0)e^{-j\omega t} \quad , \qquad \textbf{(B8.b)}$$

where a(0) and a*(0) are constants of integration.

The two different *normal modes* of equations (B8.a and B8.b) illustrates the concept of mode division and offers the advantage of visualizing equ (B8.a) and equ (B8.b) as two counterrotating vectors. However, if two modes rotate in the same direction and are weakly coupled, then these modes will couple more efficiently than modes of

opposite sense. An injection-based oscillator is an example of this. The counterrotating vector concept will also assist in understanding the coupling phenomenon within a distributed-feedback structure [11], [56]. Equations (B8) can be modified to describe two waves of constant phase constant β travelling in opposite directions of z and $-z$ as shown below.

$$a(t) = a(0)e^{j\beta z} \quad , \tag{B9.a}$$

$$a^*(t) = a^*(0)e^{-j\beta z} \quad . \tag{B9.b}$$

APPENDIX C

PREPRINT

Proceedings of 1994 IEEE Ultrasonics Symposium
Cannes, France, 1-4 November 1994

Radiation Conductance and Grating Reflectivity Weighting Parameters for Dual Mode Leaky-SAW Resonator Filter Design

P. J. Edmonson and C. K. Campbell

Department of Electrical and Computer Engineering
McMaster University, Hamilton, Ontario, Canada, L8S 4L7

Abstract — Antenna theory is applied to model the radiation conductance of thick-film interdigital transducers (IDTs) in dual mode wideband leaky-SAW resonator-filters on 64° Y-X $LiNbO_3$ employing a three-IDT structure. As well, SAW coupling-of-modes reflection-grating equations and IDT S-parameters are modified to cater for increased leaky-SAW attenuation above the Bragg frequency. Theoretical frequency response computations are in excellent agreement with experimental results obtained for several 85-MHz structures fabricated with metallization film thickness ratios (h/λ) of up to 3 %.

INTRODUCTION

For the past two years, there has been a growing interest in low-loss, wideband SAW filters operating in the 900 MHz region for personal communication services (PCS). A popular design includes the three-IDT dual-mode leaky-SAW structure on 64° Y-X $LiNbO_3$ [1]. Benefits of this filter type include a 4% fractional bandwidth capability, with insertion loss (IL) < 2 dB, and input-output impedance-matching capability.

The frequency response of this leaky-SAW filter type is governed by the IDT film metallization ratio ($(h/\lambda) \approx 3$-4 % for aluminum films), as well as by the attenuation of the leaky-SAW above the Bragg frequency. The second factor results in a ripple-reduced response (and increased attenuation) above the grating stopband [2]. As sketched in Fig. 1, leaky SAW propagation into the piezoelectric substrate is at an angle (ψ) down into the crystal. This increases the grating (and IDT) attenuation [3]. As well, and as noted by Plessky [2], the phase of the grating reflection coefficient deviates from that of a SAW grating, and thus will effect the choice of IDT distances dg and dt in Fig. 1 for the required flat-band response.

This paper demonstrates how phased-array antenna modelling can be applied to obtain the distortion of the IDT radiation conductance by thick-film metallization. As well, modifications of the grating coupling-of-modes (COM) equations of Cross and Schmidt [4] are applied to cater for leaky-SAW propagation and reflection characteristics above the Bragg frequency. They are applied to the end-grating and internal IDT reflection coefficients and to the S-parameters of the IDTs. As also shown, theoretical frequency responses obtained are in excellent agreement with experimental results for such dual-mode resonator-filters with minimum 1.39-dB insertion loss, and about 4 % fractional bandwidth, fabricated for experimental convenience at 85 MHz on 64° Y-X $LiNbO_3$.

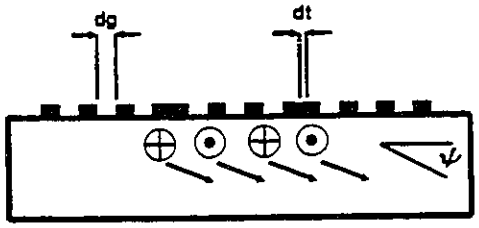

Figure 1 Acoustic wave motion and polarization for a leaky SAW.

THEORY

In this paper, individual reflection grating matrices (as modified for leaky-SAW) are applied to the end reflection gratings as well as to the center and lateral IDTs of differing finger-pair number. In the design exemplified here we employed dual parallel-connected lateral IDTs with $N_L = 19$ single-electrode fingers in each, in conjunction with a center IDT with $N_C = 31$ single-electrodes fingers. As well, we incorporated end reflection gratings with $N_G = 251$ shorted reflector strips. Each is important in the finalization of the overall response. Part A of the paper relates the effect of IDT finger reflections on radiation conductance, while Part B highlights the modifications applied to SAW COM grating equations [4], to incorporate the modifying effects of leaky-SAW propagation, reflection, and attenuation.

A. Antenna Array Modelling

Antenna theory has been previously applied by Lewis to model the propagation of surface skimming bulk waves on an isotropic substrate [5]. In the present paper the authors relate the number of fingers in an IDT to the elements of a phased-array antenna, while the frequency response of the IDT is related to the spatial pattern of the antenna beam and sidelobes.

The lobe pattern A(θ) of an antenna array, as a function of a rotational angle (θ), can be derived from [6] as;

$$A(\theta) = \frac{\sin(N \cdot E(\theta))}{N \cdot \sin(E(\theta))} \qquad (1)$$

where

$$E(\theta) = 2 \cdot \frac{\pi}{\lambda} \cdot d \cdot \cos(\theta) + \phi \cdot \frac{\pi}{180} \qquad (2)$$

and λ = wavelength, d = element separation N = number of array elements, and ϕ = phase shift between the element excitations. When ϕ = 0°, the spatial lobe pattern (after squaring) is analogous to that of an IDT sinc-function radiation conductance response, as depicted in Fig. 2.

For ϕ > 0°, we represent the equivalent antenna response function C(θ) as

$$C(\theta) = (A(\theta, \phi=0) \cdot A(\theta, \phi>0) \cdot \sqrt{N})^2 \qquad (3)$$

where N = number of fingers of the particular IDT. Note that (3) is the square of the product of "perturbed" (non-sinc function) and "unperturbed" (sinc function) antenna responses.

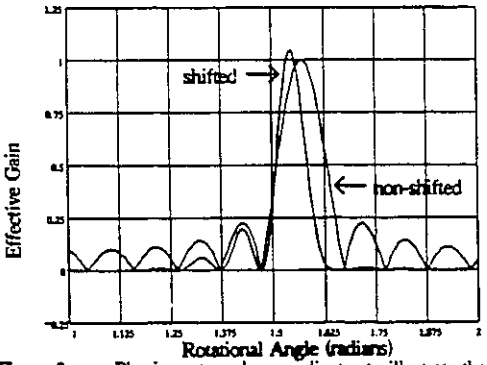

Figure 2 Plot in rectangular coordinates to illustrate the new shifted radiation antenna pattern as compared to the sinc shaped non-shifted one.

In a similar manner we obtain the distorted radiation conductance of an IDT as the product of perturbed and unperturbed functions, together with an empirical weighting factor W(f) given by

$$W(f) = \frac{1}{\sqrt{1 - |\rho|}} \qquad (4)$$

where | ρ | in (4) is the magnitude of the reflection coefficient of an IDT. Here, | ρ | is obtained from the 2 x 2 SAW reflection-grating equations of Cross and Schmidt [4] as

$$\rho = \frac{G_{21}}{G_{11}} \qquad (5)$$

in terms of grating matrix parameters

$$G_{21} = -je^{j\theta} \cdot \tanh(\sigma L) \cdot e^{-j\beta L} \qquad (6)$$

$$G_{11} = \left(\frac{\sigma}{\kappa} + j\left(\frac{\delta - j\alpha}{\kappa}\right)\tanh(\sigma L)\right)e^{j\beta L} \qquad (7)$$

$$\sigma = \sqrt{\kappa^2 - (\delta - j\alpha)^2} \qquad (8)$$

with, α = attenuation constant, L = grating length, $\beta = \omega_o / v_o$ = unperturbed phase constant and θ = reference phase. Here, $\kappa = K_{12}$ = mode-coupling parameter [1]. As well, frequency-deviation parameter δ is

$$\delta = \frac{2\pi(f - f_o)}{v} + K_{11} \qquad (9)$$

in terms of self-coupling factor K_{11} [1].

The IDT radiation conductance $Gin_{ant}(f)$ for each input IDT, as distorted by finger reflections, is represented here as

$$Ant(f) = (Re(1 + (W(f) \cdot \rho)) \cdot e^{-j\frac{\pi}{4}})^2 \qquad (10)$$

$$Gin_{ant}(f) = Gin_a(f) \cdot Ant(f) \quad (11)$$

where Gin_a = unperturbed sinc-function radiation response of IDT in the absence of finger reflections, and Ant(f) represents the perturbation due to such reflections. Note that the phase angle term in (10) is included to account for such reflections from *finger edges*. (A similar equation applies to the perturbed radiation conductance $Gout_{ant}$ of the output IDT).

The distorted radiation conductances thus obtained using this antenna method are shown in Fig. 3 for the center IDTs. For comparison, Fig. 3 also shows the radiation conductance obtained using the parameters of Uno and Jumonji applied to SAW resonators on quartz [7]. The standard sinc function radiation conductance without finger reflections is also shown for comparison. Fig. 3 also shows the computed imaginary component of the IDT reflection coefficient. It is interesting to note that the location of the shifted radiation conductance peak corresponds to the first null of this imaginary component.

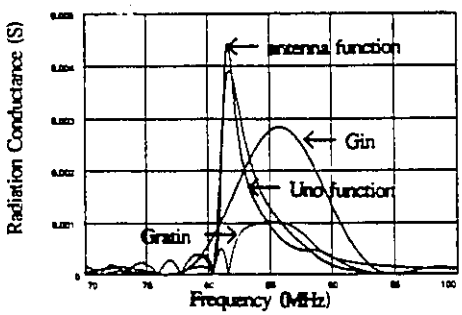

Figure 3 Input IDT radiation conductance with, (a) no finger reflections, Gin, (b) the Uno function, Gunin, (c) the antenna function, Ginant and the imaginary component of the reflection coefficient, Gratin.

B Modification to the COM equations for a SAW Reflection Grating.

The SAW reflection grating parameters in (5),(6) and (7) were next modified to cater for leaky-SAW propagation, reflection and loss. Fig. 4 illustrates the modified reflection coefficient responses above the Bragg frequency for an 85-MHz end grating (with N_G = 251 shorted reflector strips) and a lateral IDT (N_L = 19 single-finger electrodes), both with film thickness ratio (h/λ) = 4%. The modified reflection coefficient ρ for the IDTs were employed in the IDT scattering matrix relationships, defined here as

$$S_{11} = Re(\rho)^2 + \left(\rho\sqrt{1-|Im(\rho)|^2}\right) \cdot e^{-jN\frac{\lambda}{4}\delta} \quad (12)$$

$$S_{21} = \sqrt{1-|S13|^2-|S11|^2} \cdot e^{-jN\cdot\frac{\lambda}{4}\cdot\delta} \quad (13)$$

$$S_{13} = \frac{\sqrt{2\cdot G\cdot(1-|Im(\rho)|^2)\cdot Y}\cdot e^{-jN\cdot\frac{\lambda}{4}\cdot\delta}}{|Y|} \quad (14)$$

The phase terms in (12),(13) and (14) were used to accomodate for the leaky-SAW propagation characteristics.

The S-matrix parameters were converted to transmission T-matrix representations [8], for computation of the overall frequency response, following the method of Ref. [4].

Here, we employed two transmission-matrix computations to obtain the overall frequency response of the dual mode resonator leaky-SAW resonator-filter. In the second computation, (which was combined with the first), an additional phase-shift term was included between the spacings dg and dt to cater for the 180° phase shift between the two modes.

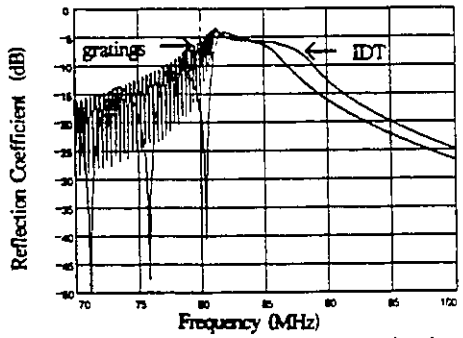

Figure 4 Reflection coefficient components using the modified COM equations for the input IDT and end gratings.

EXPERIMENTAL

Several devices were fabricated at McMaster University on 64° Y-X $LiNbO_3$ for a centre frequency of 85 MHz with various film thickness ratios (h/λ). Significant parameters of these fabrications are the separations between the center and lateral IDTs (dt) and the gap offsetting the shorted end reflectors from the IDTs (dg) shown previously in Fig. 1. The gap separations were chosen as, dt = 0.0λ which was realized by touching the two grounded electrodes of the input and output IDT and dg was 0.25λ, or synchronously spaced. Fig. 5 illustrates both the calculated and measured response of a single dual mode leaky-SAW filter. The IDT and end grating

parameters were $N_C = 31$, $N_L = 19$ and $N_G = 251$. The film thickness ratio was only 0.4 % which limited the widening of the passband (2 % fractional bandwidth) and suppression of the above band ripples. The lower film thickness did not affect the insertion loss, measured as 1.39 dB at 85.6 MHz. Two of these filters were cascaded together and are shown in Figure 6. The combined insertion loss of devices #1 and #2 were 3.9 dB at 85.6 MHz and a measured fractional bandwidth of about 1.8 %. Several regions of Rayleigh wave conversion can be observed at 74 MHz and between 88 to 96 MHz.

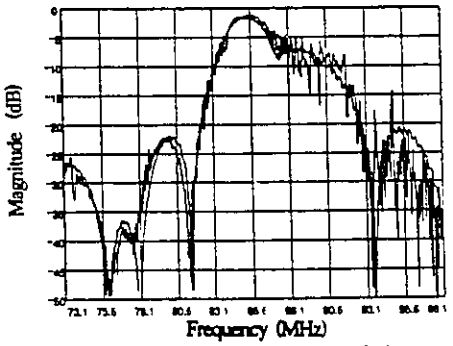

Figure 5 Frequency response showing both the theoretical and measured values of a single filter with a centre frequency of 85.5 MHz. Scales are 73.1 - 98.1 MHz and 5 dB/div.

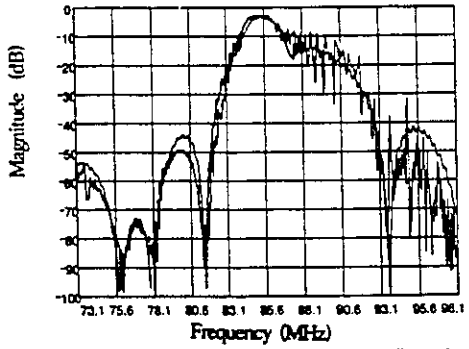

Figure 6 Frequency response of two identical filters in cascade. Both the theoretical and measured are displayed. Scales are 73.1 - 98.1 MHz and 10 dB/div.

The film thickness ratio of device #3 was increased to 3 %. The IDT and end grating parameters were $N_C = 29$, $N_L = 19$ and $N_G = 251$. Fig. 7 depicts both the calculated and measured response of this dual mode leaky-SAW filter, showing that the fractional bandwidth has now increased to 4.4 % and the IL remaining low at 1.6 dB.

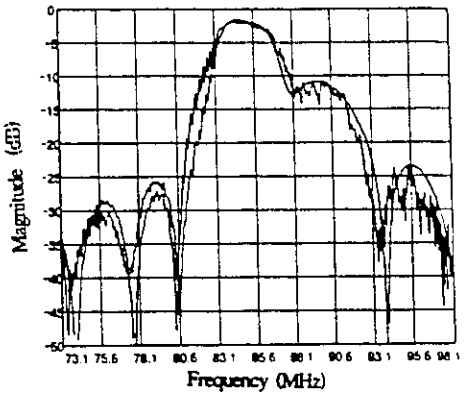

Figure 7 The theoretical and measured frequency responses of a single filter whose film thickness ratio has been increased to 3 %. Scales are 73.1 - 98.1 MHz and 5 dB/div.

Finally an experiment was conducted to observe the propagation of the acoustic waves within these devices [9]. The direct path Rayleigh wave travels in a nominal straight path horizontal to the surface between the transducers. The results of this wave are seen at about 74 MHz which is the same ratio with respect to the centre frequency as the ratio of velocities for non-leaky 128° Y-X $LiNbO_3$ and leaky 64° Y-X $LiNbO_3$. The other Rayleigh waves may be attributed here to interference patterns in a convergence zone path such as in sonar reflections. In such a zone, multiple ray paths add or combine coherently to reinforce the presence of acoustic energy.

This device was subsequently covered with water, to observe the suppression of Rayleigh wave conversions. Fig. 8 shows the device response with an IDT-air interface, while Fig. 9 shows that for the device with an IDT-water interface.

CONCLUSION

An antenna array technique developed here for modelling the distorted radiation conductance of an IDT with finger reflections shows good agreement with other modelling methods. As well a transmission and scattering approach used here for modelling the frequency response of low-loss wideband leaky-SAW dual mode resonator filters has yielded excellent agreement with experiment.

ACKNOWLEDGEMENTS

This work was supported by a research grant from the Natural Sciences and Engineering Research Council of Canada.

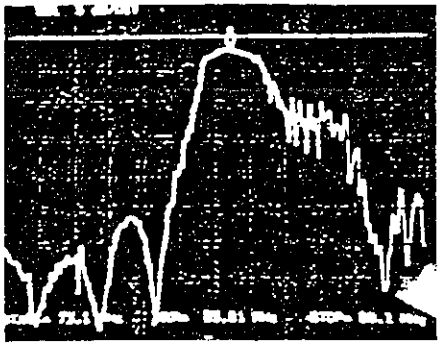

Figure 8 Measured frequency response before surface contamination to illustrate the Rayleigh conversion for both the direct and convergence zone paths. Horizontal scale, Mkr=85.6 MHz, 25 MHz span, vertical scale 10 dB per div.

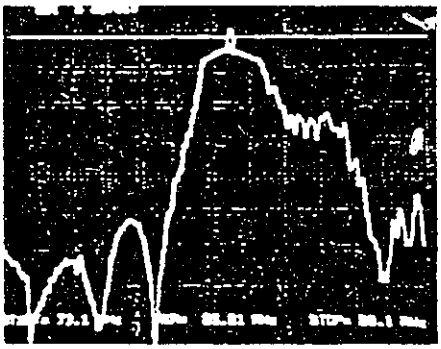

Figure 9 Measured frequency response after surface contamination that suppresses the Rayleigh conversion. Horizonal scale, Mkr = 85.6 MHz, 25 MHz span, vertical scale 10 dB per div.

REFERENCES

[1] T. Morita, Y. Watanabe, M Tanaka and Y. Nakazawa, "Wideband low loss double mode SAW filter," *Proc. IEEE Ultrasonics Symp.* 1992, pp. 95-104.

[2] V.P. Plessky, "A two-parameter coupling-of-modes model for shear horizontal type SAW propagation in periodic gratings," *Proc. 1993 IEEE Ultrasonics Symp.*, vol. 1, pp. 195-200.

[3] K. Yamanouchi and M. Takeuchi, "Applications for piezoelectric leaky surface waves," *Proc. IEEE Ultrasonics Symp.* 1990, pp. 11-18.

[4] P.S. Cross and R.V. Schmidt, "Coupled surface-acoustic wave resonators," *Bell System Technical Journal*, vol 56, pp. 1447-1482, October, 1977.

[5] M. Lewis, "Surface skimming bulk waves, SSBW," *Proc. IEEE Ultrasonics Symp.* 1977, pp. 744-752.

[6] D. Pozar, *Antenna Design Using Personal Computers*, Artech House, Inc. Dedham, MA., pp. 63-67, 1985

[7] T. Uno and H. Jumonji, "Optimization of quartz SAW resonator structure with groove gratings," *IEEE Trans. Sonics and Ultrasonics*, vol. SU-29, pp. 299-310, November, 1982.

[8] C.K. Campbell, "Scattering and transmission matrix analysis of SAW resonator filters with long-pair IDTs and triple composite modes on quartz," *Proc. IEEE Ultrasonics Symp* 1994., (to be published).

[9] C.S. Hartmann and V.P. Plessky, "Experimental measurements of propagation, attenuation, reflection and scattering of leaky waves in AL electrode gratings on 41°, 52° and 64° - $LiNbO_3$," *Proc. IEEE Ultrasonics Symp.* 1993, pp. 1247-1250.

APPENDIX D

SAW Injection Locked Oscillators: Dynamic Behaviour and Application to Neural Networks

P.J. Edmonson, P.M. Smith and C.K. Campbell
Dept. of Electrical and Computer Engineering
McMaster University, Hamilton, Ontario, Canada, L8S 4L7

ABSTRACT

The characteristics of an injection-locked oscillator are examined in two parts. Part A covers the dynamic behaviour of a surface acoustic wave injection-locked oscillator and its similarity near lock-in to that of an acousto-optic modulator. It is shown that a reflective wave component travels between the injected source and the oscillator resulting in periodic locking and unlocking of the system. These reflected waves are responsible for the classical modulation sidebands near lock-in.

In part B a SAW based neural network that can associate, categorize and store input stimuli is presented. The network can be modelled as a modified Kohonen self-organizing feature map.

INTRODUCTION

Part A: The dynamic behaviour of an ILO

Injection techniques are often used to stabilize a large amplitude, but unstable, oscillator signal with a much smaller signal that is more stable. Most applications of surface acoustic wave (SAW) injection-locked oscillators (ILOs) employ the locked condition [1-3] in which the oscillator output tracks the injected signal. More recently, interest has developed in the condition just prior to lock-in [4-5].

The schematic of an ILO, shown in Fig. 1, contains two signal components travelling along a transmission line connecting the two oscillators [6]: the external injected forward signal S_+ travelling towards the oscillator and a resulting reflected signal S_-. The reflection will result from the mismatch of circuit parameters such as frequency and quality factor (Q) of the injecting source and the oscillator.

The equation for the oscillator mode amplitude, using a coupling-of-modes in time (COMT) formalism for a resonant cavity with an unloaded quality factor $Q_0 = (\omega_0\tau_0)/2$ and sufficient gain medium, is [6]

$$\frac{da}{dt} = a\left(j\omega_0 - \frac{1}{\tau_0} - \frac{1}{\tau_e} + \frac{1}{\tau_g}\right) + \sqrt{\frac{2}{\tau_i}}\,S_+ \qquad (1)$$

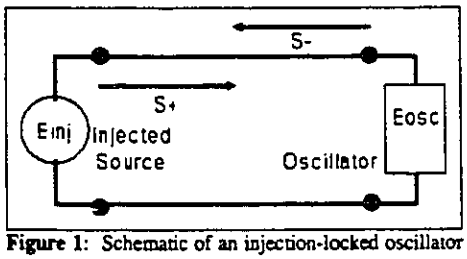

Figure 1: Schematic of an injection-locked oscillator

where a = mode amplitude, ω_0 = free running angular frequency, $1/\tau_0$ = oscillator cavity decay rate due to internal loss, $1/\tau_e$ = escape rate out of the cavity, $1/\tau_g$ = rate of growth of mode amplitude with the oscillator and S_+ = injected wave mode amplitude at angular frequency ω_{inj}. The injected wave coefficient $\sqrt{(2/\tau_i)}$ is the coupling factor into the oscillator. The circuit will oscillate, in a steady-state at ω_0 with no driving source S_+, provided $1/\tau_g = 1/\tau_0 + 1/\tau_e$.

In this paper, we will develop an equation to predict the dynamic amplitude of the oscillator just prior to lock-in. The beat frequencies introduced by the travelling waves will lead to an output signal containing frequencies $\omega_{out} = \omega_{inj} \pm m\Delta\omega$, where $\Delta\omega$ is the frequency offset between the oscillator and the injected signals and m is a large integer.

Part B: Applications of an ILO to Neural Networks

Neural networks that identify and classify input signals can be thought of as mapping networks. The Kohonen model of such a map consists of nerve fibres running horizontally across a spatial distance to distribute input signals. These inputs excite a layer of neurons via synaptic connections. Interaction between neurons limit the reaction to a limited excitation zone. The layer then acts as a topographical feature map, for the excitation zone varies in a localized way depending upon the nature of the stimulus input signal [7]. The formation of these topographical excitation clusters are self-organized and do not require any supervision or reinforcement training.

Kohonen's Self Organized Feature Map (SOFM) displays two important characteristics. The first is that the network tends to concentrate its activity into local clusters or bubbles. The second is that location of the clusters are

1051-0117/93/0000-0131 $4.00 © 1993 IEEE

determined by the nature of the input stimulus signals.

A modified SOFM is shown in Fig. 2, where instead of a two-dimensional spatial topographical map, a one-dimensional map similar to a frequency spectrum is illustrated. The number of neurons in the layer will determine the resolution or the width of each cluster. The selection of a "frequency cluster" follows the same algorithm as presented by Kohonen [8] as:

Step 1) *Initialization*: All input weights can be either initialized to zero or randomly set.

Step 2) *Choice of Stimulus*: Allow a sensory signal to be the stimulus to all neurons.

Step 3) *Response*: Determine the corresponding excitation cluster.

Step 4) *Adaptation Step*: Carry out a learning step by modifying the synaptic strengths and continue with step 2.

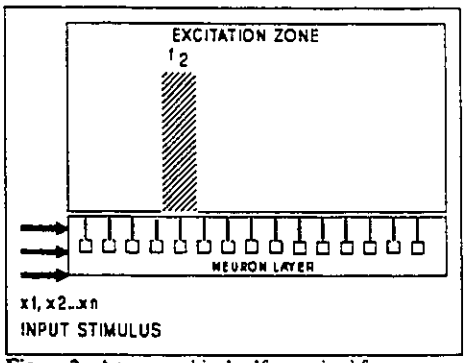

Figure 2: A topographical self organized feature map.

The input signal x_2 is the stimulus to all of the neurons in the layer below the excitation zone of Fig. 2. Only the localized neurons beneath f_2 will respond because of the favourable excitation between the stimulus and the neurons. Within several time durations the cluster f_2 will build to a maximum and all other possible clusters $f_1, f_3, \ldots, f_n$ will be suppressed. The signal x_2 is therefore mapped onto the feature map of f_2.

In this paper, we will show that an injection locked oscillator employing a single multimode SAW device can be used to implement the scheme shown in Fig. 2. This approach has the additional advantage that it will retain the classification even when the input signals have been removed.

THEORY

Injection-Locked Oscillators

The equations governing the stationary phase angle α_{ss} between oscillator and injected signals in an injection-locked oscillator (ILO) employing a tuned-circuit feedback element may be given as [2]

$$\sin(\alpha_{ss}) = 2Q_0 \frac{E_{osc}}{E_{inj}} \frac{\Delta\omega}{\omega_0} \qquad (2)$$

for $+90° \le \alpha_{ss} \le -90°$, where Q_0 = tuned resonator quality factor, E_{osc} = oscillator voltage, E_{inj} = injected signal voltage, ω_0 = free-running oscillator frequency, and $\Delta\omega = (\omega_{inj} - \omega_0)$, where ω_{inj} = injection signal frequency. The locking bandwidth B can be used to define a lock parameter K

$$K = 2Q_0 \frac{E_{osc}}{E_{inj}} \frac{\Delta\omega}{\omega_0} = \frac{\Delta\omega}{B} \qquad (3)$$

where $|K| < 1$ for lock. The dynamic behaviour of the ILO can be described in terms of the phase angle $\alpha(t)$

$$\alpha(t) = 2\arctan\left[\frac{1}{K} + \frac{\sqrt{K^2-1}}{K} \tan\left(B \frac{(t-t_0)}{2} \sqrt{K^2-1}\right)\right] \qquad (4)$$

Part A: ILO Near Injection Locking

We can define a reflection coefficient Γ to describe the dynamics of an oscillator at various levels of injected amplitude S_+ and reflected amplitude S_- [9, 10]

$$\Gamma = \frac{S_-}{S_+} \qquad (5)$$

When the injected signal power is not quite sufficient to produce locking, a phenomenon occurs within an ILO that is similar to the summation of signals that produces sidebands within an acousto-optic modulator (AOM) [11]. Within the ILO, the mode amplitude is the sum of the oscillator signal and the injected and reflected signals S_{+m} and S_{-m}, where

$$S_{+m+1}(t) = \Gamma S_{+m} e^{(+j\omega_0 t)} \qquad (6)$$

and

$$S_{-m-1}(t) = \Gamma S_{-m} e^{(-\gamma\omega_m)} \qquad (7)$$

A plot of the dynamic mode amplitude versus time is shown in Fig. 3. The frequency response of this composite waveform is illustrated in Fig. 4 where the classic cascading sidebands inherent to the vicinity of lock-in are apparent.

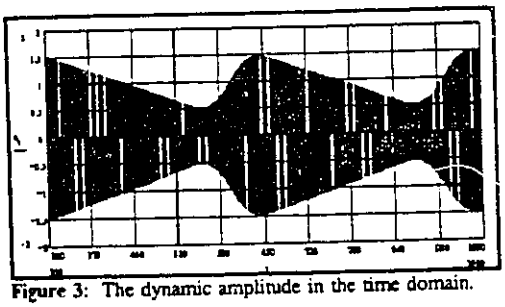

Figure 3: The dynamic amplitude in the time domain.

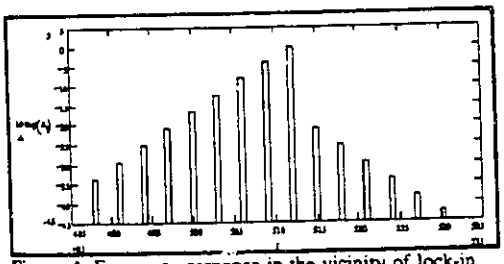

Figure 4 Frequency response in the vicinity of lock-in.

Part B: SAW-based self-organised feature map

The Kohonen SOFM is a network that consists of two layers, an input layer of source nodes and a competitive layer made up of a two-dimensional flat grid. Fig. 5 illustrates a schematic of a Kohonen network where lateral feedback occurs. Two types of connections, namely the *forward* and *lateral feedback* connections, are distinguished in this type of network. The forward connections are coupled from the input source nodes to the individual competitive neurons. The coupling weights κ_{ij} provide a selective response to the input stimulus. The lateral feedback connections are internal to the computational neuron layer. These feedback connections c_{ij} produce an excitatory or inhibitory effect depending upon the spatial distance of the originating j_{th} neuron to the destination i_{th} neuron of the feedback connection. A "mexican hat" function is often used to describe the three distinct interaction areas caused by the lateral feedback connections c_{ij} as [12]:

1) Short range lateral excitation region.
2) Penumbra of inhibitory action area.
3) Area of relatively weak excitation.

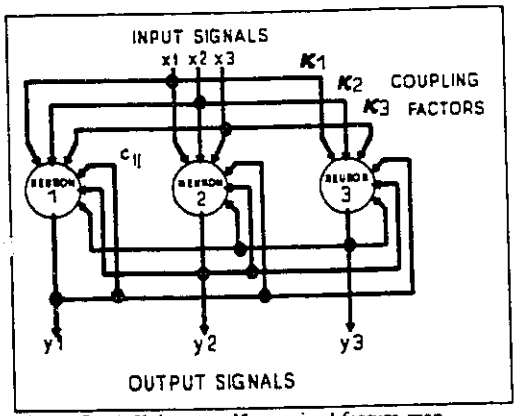

Figure 5 A Kohonen self-organized feature map.

The idea of using an oscillator as a neuron was developed by Hoppensteadt, who showed that a voltage controlled oscillator (VCO) employing a PLL can be viewed as a voltage controlled oscillator neuron (VCON) [13]. The nonlinear equations describing an ILO (equations 2, 3 and 10) are identical to those for a PLL [14].

The Kohonen network shown in Fig. 5 can be modified by introducing a bank of parallel resonators to map a one-dimensional frequency plane [8]. A similar approach is shown in Fig. 6, where the equivalent parallel resonators are replaced with a multimode SAW single phase unidirectional transducer (SPUDT) in a feedback oscillator circuit. This circuit will behave as a multimode injection-locked oscillator when subjected to an input stimulus [3].

An injection locked oscillator neuron (ILON) has the advantages, when compared with other approaches (digital or VCO-based) of fewer components, a much higher natural loop frequency and of operating well into the gigahertz range. For each separate comb oscillator operating at a modal frequency f_i, with a bandwidth BW_i, an ILON exists that will localize a cluster at any one of modal frequencies y_1, y_2 and y_m, provided that the coupling κ_{ij}, loop gain and phase conditions are met.

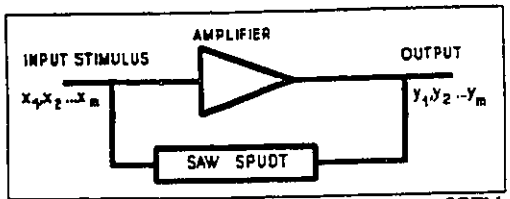

Figure 6 SAW SPUDT configured as a Kohonen SOFM.

The shorted grating reflectors positioned between the interdigital transducers of the SPUDT perform a bandwidth limiting function on each of the modal peaks. This narrowing function is similar to the "mexican hat" function that determines the resolution of the topology map in conventional neural networks [13]. The frequency, bandwidth and spacing of these clusters are determined by the parameters set within the SAW SPUDT device.

EXPERIMENT

Part A; Dynamic Behaviour of an ILO

A injection-locked oscillator having a multimode SPUDT was constructed. Its free running frequency was 82.095 MHz and it produced -5.8 dBm of output power.

To study its behaviour, a signal of -10.2 dBm at 82.145 MHz was injected. This power level was insufficient to lock the oscillator and resulted in the time response given in Fig. 7a, which shows a periodic lock and loss of lock in the circuit. The high amplitude instances correspond to the locked condition, while during the lower amplitude the circuit momentarily becomes unlocked. The unlocking duration is about twice the group delay of the SPUDT device. The period of this process is about 45.46 μs, which corresponds to the 22 kHz sidebands of the frequency response shown in Fig 7b. Here, the lower frequency sidebands are associated with the oscillator signal S_- from equation (7) and the upper sidebands conform to the injecting signal S_+ of equation (6). The reason the upper sidebands have a lower amplitude is because they are associated with the smaller injected signal.

In order to measure the instantaneous output signal frequency as a function of time, an ILO having a pulsed injected signal was used. In this case, the ILO had f_{osc} = 82.084 MHz and f_{inj} = 82.100 MHz, while P_{inj} was 1 dB below lock. The output from an HP 5373A modulation analyzer is given in Fig. 8 and shows that the circuit initially locks in to f_{inj}, but then periodically loses lock. One interesting feature is that during this unlocking process, the frequency does not return to f_{osc}, but extends beyond that frequency.

Part B: Application to a Neural Network

An experiment was devised to produce mode selection and control of a multimode SAW oscillator employing a low-loss SAW comb filter in the oscillator feedback loop. Mode selection was accomplished by a circuit containing an up-chirp and a down-chirp dispersive delay lines, each activated by a delayed (ΔT) impulse. The chirp signals are then mixed to produce a temporary injection stimulus at a desired modal frequency. A schematic of this circuit is shown in Fig. 9. Following the injection, free-running oscillations were observed at each of the M modal frequencies within the overall comb response. The processing time for this SOFM to determine a new ΔT between pulses was extremely low, with modal switching times of under 2 μs.

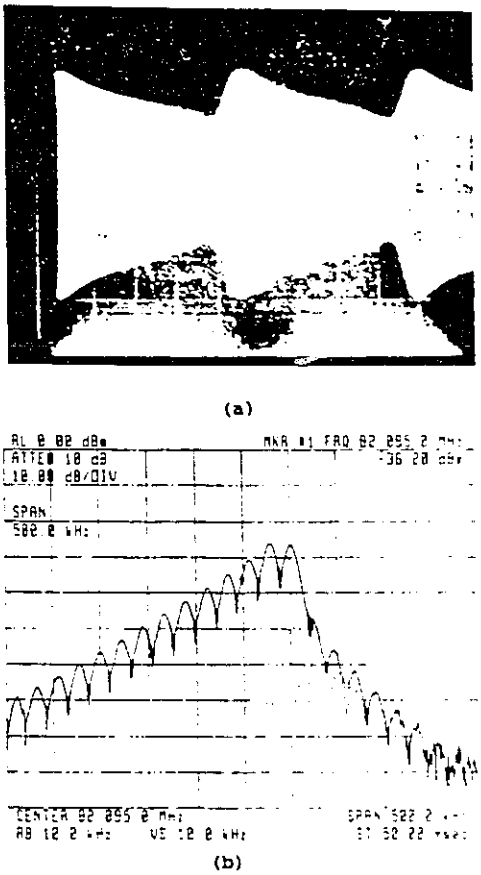

Figure 7 Output signal from ILO in the vicinity of lock-in:
(a) Time response (Horiz: 10 μs/div, vert: 0.1 mV/div)
(b) Spectrum

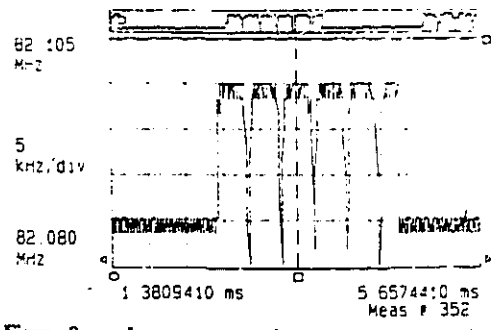

Figure 8 Instantaneous frequency versus time response of the ILO in the vicinity of lock-in.

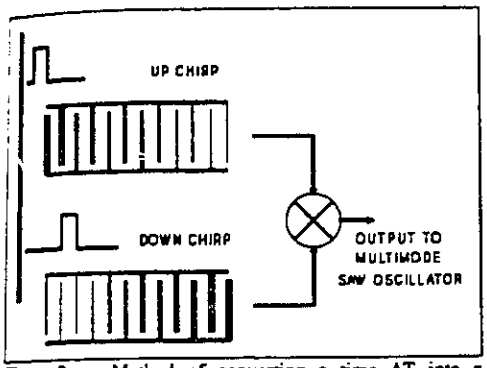

Figure 9 Method of converting a time ΔT into a frequency stimulus.

The mixer output is shown in Fig. 10 and contains, in addition to the desired injection stimulus, numerous intermodulation products. These included the sum and difference frequencies as well as the "fundamental" frequencies produced by the chirps. Despite the fact that the desired signal was 15 dB above the spurious "noise", the network identified the correct modal frequency.

The signals from the mixer thus provide the *forward connections* to the neural network with the appropriate coupling factors (weights of their respected amplitudes) κ_{ij}. The temporal spacing τ of the IDT fingers and the reflectors within the SAW device provide the *lateral feedback connections* "c_{ij}" to determine the excitatory or inhibitory effects.

CONCLUSIONS

The dynamic behaviour of the output signal of an injection-locked oscillator in the viscinity of locking has been explained. Experimental results showing the output signal as a function of time, the corresponding steady-state frequency response, and dynamic instantaneous frequency response have been presented. They show that the oscillator in this mode periodically loses and regains lock.

Pulse separation classification by mode selection of a multimode surface acoustic wave injection-locked oscillator has also been demonstrated. This process has parallelism with the Kohonen self-organized feature mapping techniques for neural networks. The SAW-based Kohonen self-organized neural network (SONN), behaving as a multiple neuron identifier by transforming a desired measurement ΔT to a frequency stimulus and distinguishing this signal onto a feature map, was demonstrated.

REFERENCES

1. C. Campbell, *Surface acoustic wave devices and their signal processing applications*, Academic Press, 1989.
2. R. Adler, "A study of locking phenomena in oscillators," *Proc. IRE*, vol 34, no. 6, pp. 351-367, June 1946.

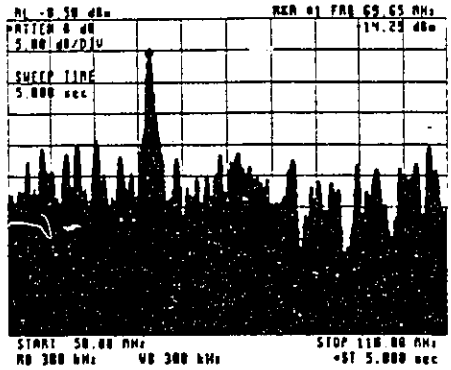

Figure 10 Frequency spectrum of the input to the neuron layer, showing a S/N ratio of about 15 dB.

3. C.B. Saw, P.M. Smith, P.J. Edmonson and C.K. Campbell, "Mode selection in a multimode SAW oscillator using FM chirp mixing signal injection," *IEEE Trans. on UFFC*, vol 35, no. 3, pp. 390-395, May 1988.
4. P.J. Edmonson, P.M. Smith and C.K. Campbell, "SAW-based carrier recovery without phase ambiguity for 915 MHz BPSK wireless digital communications," *Proc. 1992 Ultrasonics Symp.*, Tucson, AZ, pp. 241-244, October 1992.
5. C.K. Campbell, P.J. Edmonson and P.M. Smith, "Effect of amplifier saturation on one-sided beat spectrum of driven unlocked oscillator," *Electronics Letters*, vol 28, no.12, pp. 1121-1122, June 1992.
6. H.A. Haus, *Waves and fields in optoelectronics*, Prentice-Hall, New Jersey, 1984, pp. 207-210.
7. H. Ritter, T. Martinetz and K. Schulten, *Neural computation and self-organizing maps*, Addison-Wesley, Massachusetts, 1992.
8. T. Kohonen, "Self-organized formation of topologically correct feature maps," *Biological Cybernetics*, vol 43, pp. 59-69, 1982.
9. C.K. Campbell, "Beat frequency spectra in a driven unlocked multimode SAW comb oscillator," *Proc. 1987 Ultrasonics Symp.*, Denver, CO, pp. 69-71, 1987.
10. M. Armand, "On the output spectrum of unlocked driven oscillators," *Proc. IEEE*, vol. 57, pp. 798-799, 1969.
11. F. Heismann, "In-line electro-optic frequency translator for fiber-optic sensors," *Proc. SPIE*, vol. 517 Integrated Optic Circuit Engineering, pp. 206-211, 1984.
12. M. Caudill, "Neural networks primer part IV," *AI Expert Magazine*, vol. 3, no. 8, pp. 61-67, August 1988.
13. T. Khanna, *Foundations of neural networks*, Addison-Wesley, Massachusetts, 1990, pp. 158-167.
14. L.W. Couch, *Digital and analog communication systems*, MacMillan, New York, 1990.

APPENDIX E

IEEE TRANSACTIONS ON ULTRASONICS, FERROELECTRICS, AND FREQUENCY CONTROL, VOL. 39, NO. 5, SEPTEMBER 1992

Injection Locking Techniques for a 1-GHz Digital Receiver Using Acoustic-Wave Devices

Peter J. Edmonson, *Member, IEEE*, Peter M. Smith, *Member, IEEE*, and C. K. Campbell, *Fellow, IEEE*

***Abstract*—The use of surface-transverse-wave (STW) resonator-based oscillators as amplifiers and as carrier recovery elements is discussed. It is demonstrated that these oscillators can amplify phase-shift-keyed signals with very little added noise, while providing a constant output power. Their performance in carrier recovery applications is analyzed. Experimental results showing the amplification with more than 80 dB of dynamic range of a 2 Mb/s BPSK signal and the carrier recovery of a 8 Mb/s signal with a 1-GHz STW oscillator are shown.**

I. Introduction

THE PROCESS by which an oscillator tracks a weak injected signal of similar frequency, known as injection locking, was first studied in detail by van der Pol [1] in the 1920's. His work triggered intense research in the area, and led to the classic paper by Adler [2], in which the requirements for small-signal injection locking were established and an analysis of the locking process was presented. Paciorek [3] and Kurokawa [4] extended these results and produced dynamic analyses of the locking process for both small- and large-signal injection. Kurokawa [4] also studied the resulting stability and noise.

Injection-locked oscillators (henceforth referred to as "locked") can be used to perform a wide range of tasks, including amplification with limiting [5], [6], frequency up-conversion and multiplication [7], frequency and phase modulation and demodulation [8], and phase shifting. In fact, an entire receiver can be built solely with the use of locked oscillators.

Surface-acoustic-wave (SAW) resonators have also been found to have very useful properties in UHF oscillator applications [9], [10]. They lead to good phase noise performance and, in contrast to bulk crystal resonators, can be used to generate a stable UHF signal without the need to frequency-multiply. In addition, their small size, ruggedness and relatively low cost make them ideal for mobile applications. While some work has been done on locked SAW oscillators [11], the area has remained largely unexplored.

Surface-transverse-wave (STW) resonators offer many of the same advantages as their SAW counterparts [12]. Since they employ bulk waves that propagate just below the surface, they offer a higher frequency of operation and lower sensitivity to surface defects. However, they usually have a higher insertion loss and a lower quality factor.

Manuscript received November 4, 1991; revised and accepted March 23, 1992.

P. J. Edmonson is with the Department of Electrotechnology, Mohawk College Hamilton, ON, L8N 3T2 Canada.

P. M. Smith and C. K. Campbell are with the Department of Electrical and Computer Engineering, McMaster University, Hamilton, ON, L8S 4L7 Canada.

IEEE Log Number 9201916.

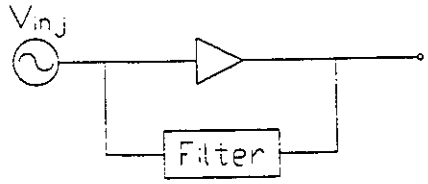

Fig. 1. Block diagram of injection locked oscillator circuit.

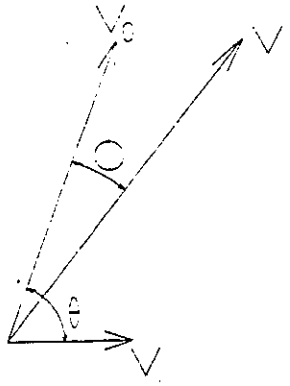

Fig. 2. Phasor diagram showing the output signal V as the sum of the injected signal V_i and the free-running signal V_0.

In this paper, we present results from a study on locked STW oscillators as automatic gain controlled amplifiers and as carrier recovery elements in binary phase-shift-keyed (BPSK) systems. We show that a locked oscillator can alleviate the very stringent requirements placed on the front-end amplifier stages [13] and provide carrier recovery without the very high-power requirements of traditional UHF phase-locked loop systems [14].

II. Theory

An oscillator can be represented by the circuit in Fig. 1. It contains a nonlinear gain element and a frequency-selective feedback element with a quality factor Q. If left undisturbed, the circuit will oscillate at a frequency ω_0 for which the loop gain is equal to 1 and the loop phase is a multiple of 2π rad.

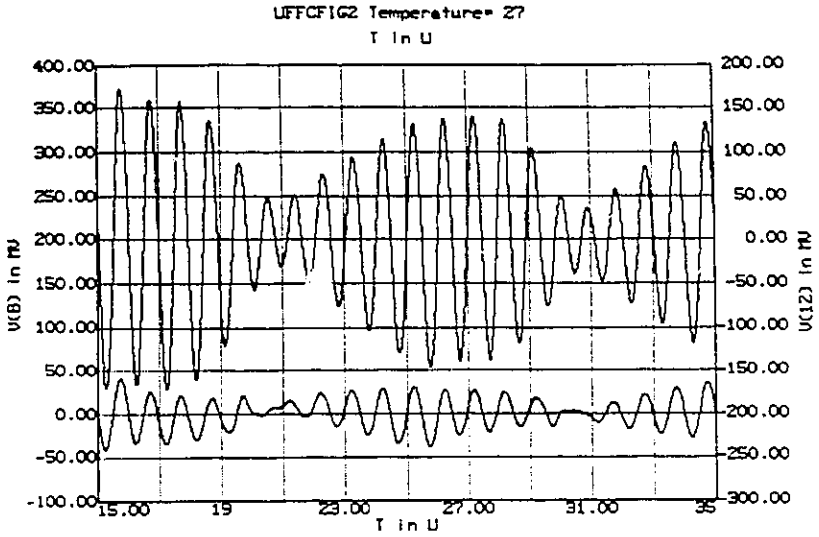

Fig. 3. SPICE simulation illustrating amplification of a BPSK signal. Lower trace is the input to the oscillator. Upper trace is the oscillator output.

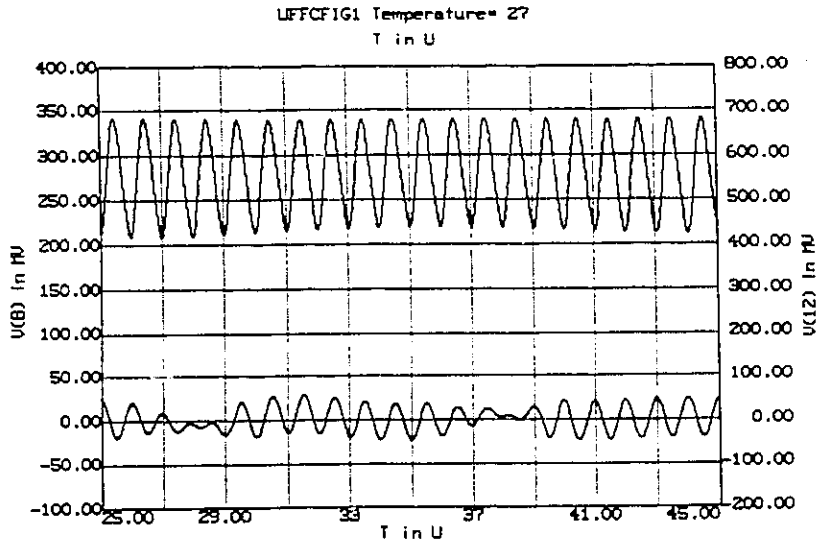

Fig. 4. SPICE simulation illustrating carrier recovery for a BPSK system. Lower trace is input to the oscillator. Upper trace is the oscillator output.

When an independent signal of frequency ω_i is applied to the loop, it will add vectorially to the free-running oscillatory signal. This is illustrated by the phasor diagram in Fig. 2 in which V_0 represents the free-running oscillator voltage, V_i is the injected signal voltage and V is the resulting voltage. A locked oscillator will be characterized by a constant angle θ.

Paciorek [3] showed that, based on the previous phasor analysis, the rate of change of θ can be written as

$$\frac{d\theta}{dt} = \Delta\omega_0 - \left(\frac{\omega_0}{2Q}\frac{V_i}{V_0}\right)\frac{\sin\theta}{1+\frac{V_i}{V_0}\cos\theta} \quad (1)$$

where $\Delta\omega_0 = |\omega_i - \omega_0|$ is the initial frequency difference between the injected and the free-running signals.

If $\Delta\omega_0$ is assumed to be small, then the angle θ can be shown [3] to be

$$\theta \simeq \theta_0 e^{-\frac{V_i}{V_0}\frac{\omega_0 t}{2Q}} \quad (2)$$

for low injection levels ($V_i \ll V_0$), and

$$\theta \simeq \theta_0 e^{-\frac{\omega_0 t}{2Q}} \quad (3)$$

otherwise, where θ_0 is the initial phase difference between the free-running and the injected signals.

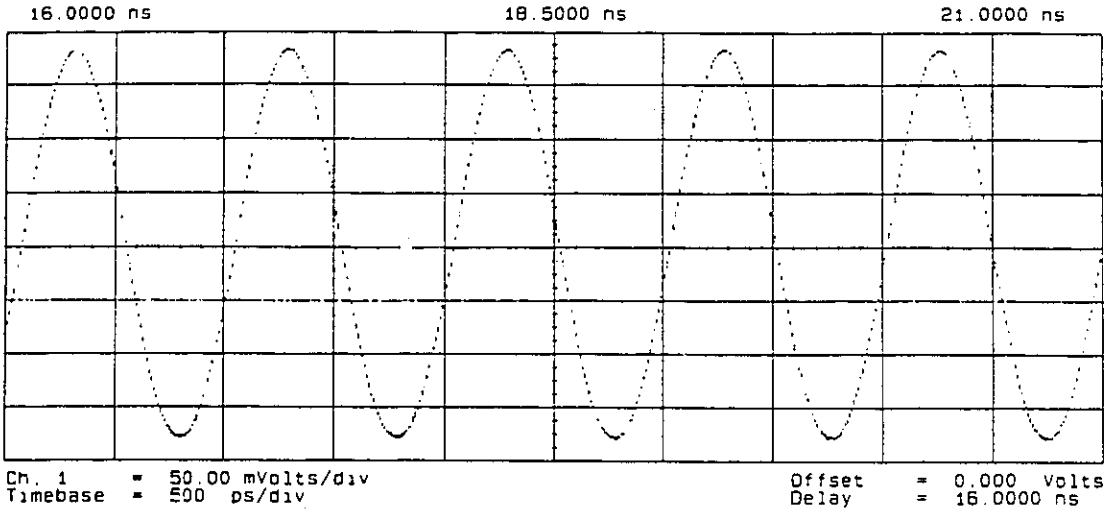

Fig. 5. Sampling oscilloscope plot of the oscillator output with a +16-dBm injected signal. No distortion is evident.

The locking range $\Delta\omega_{0\,max}$ can be found by first differentiating θ with respect to time to obtain the difference frequency $\Delta\omega_0$, and then differentiating the latter with respect to θ and solving for a maximum [3]. We get

$$\Delta\omega_{0\,max} = \frac{\omega_0}{2Q}\frac{V_i}{V_0}\frac{1}{\sqrt{1-(V_i/V_0)^2}} \tag{4}$$

which indicates that, as expected, the locking bandwidth is a function of both the quality factor of the resonant element and the voltage of the injected signal. Equation (4) can be rewritten to obtain P_i, the power required to injection lock an oscillator:

$$P_i = P_0\left(\frac{\Delta\omega_0}{\frac{\omega_0}{2Q}}\right)^2. \tag{5}$$

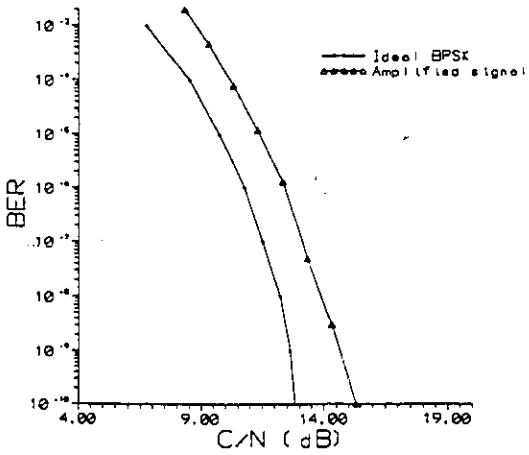

Fig. 6. BER performance of synchronous NRZ 2 Mb/s signal amplified with locked oscillator.

A. Amplification

In general, there are three modes in which an oscillator with an injected signal will operate [6].

1) *Injection-Locked*: The injected signal is within the injection locking bandwidth of the oscillator, as defined by (4). The oscillator therefore tracks the input signal and its output is an amplified version of the latter. An oscillator in this mode can provide more than 50 dB of automatic gain control with no signal saturation. This is the desired mode of operation.

2) *Threshold*: The (weak) injected signal interacts with the oscillator's free- running signal and beat frequencies form about ω_0.

3) *Free-Running*: The power in the injected signal is insufficient to affect the oscillator. Only the free-running signal is present.

A locked oscillator will track a frequency or phase modulated input signal, subject to the injection bandwidth constraints. For a binary phase-shift-keyed (BPSK) signal, the symbol duration T must be sufficient for a 180° phase change to occur in the oscillator. This gives us a minimum symbol duration of

$$T_{min} > \frac{\pi}{\Delta\omega_{0\,max}} = \frac{1}{2\Delta f_{0\,max}}. \tag{6}$$

Fig. 3 shows a SPICE simulation illustrating the amplification of a BPSK signal. The simulation was performed at a lower frequency by using an LRC resonant circuit to represent the STW device. The lower part of the figure shows a 1-MHz carrier, modulated with an alternating 50 kHz bit sequence that is fed into the oscillator. We see that the output, shown in the upper part of the figure, tracks the input signal and provides a 15-dB gain.

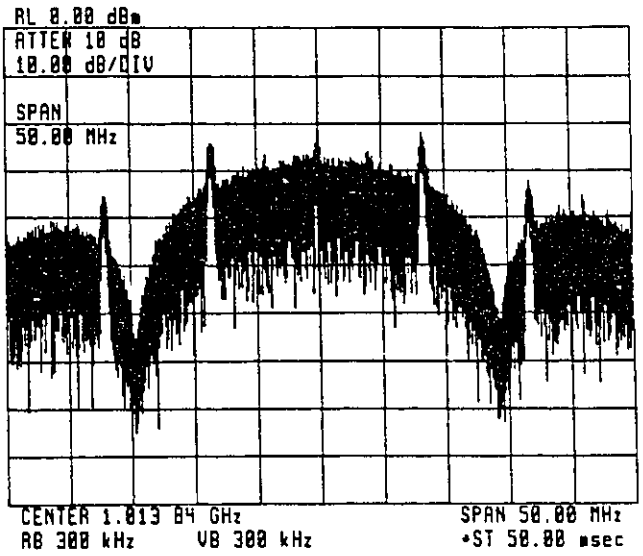

(a)

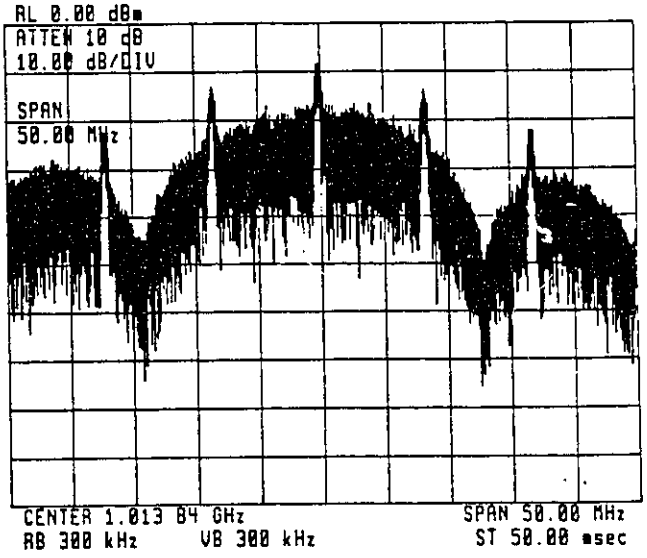

(b)

Fig. 7. Carrier recovery of 8 Mb/s RZ signal using locked oscillator. (a) Spectrum of signal at input of oscillator. (b) Spectrum of signal at output of oscillator.

B. Carrier Recovery

If the bandwidth requirements for the signal are not met, the locked oscillator will no longer be able to track the message in the input signal. It settles instead at a "mean" frequency that serves surprisingly well as a carrier recovery signal, and behaves in the same way as a phase locked loop. This behavior is illustrated in Fig. 4 with a SPICE simulation showing a BPSK input signal and the oscillator's output waveform under this condition.

Robins [15] studied the effect of noise in a phase-locked-loop (PLL) carrier recovery system. He showed that, for a typical coherent demodulation system using a PLL, the noise contains contributions from the local oscillator required to down-convert the signal to an intermediate frequency, and from thermal noise. Assuming a local oscillator with a noise to carrier ratio $(2N_{0p}/C)_{lo}$, a bit rate b, and a PLL natural frequency of f_n, the oscillator noise contribution [15] is

$$V_{lo}^2 = k_d^2 \left(\frac{2N_{0p}}{C}\right)_{lo} \left(b - \frac{f_n}{2}\right) \tag{7}$$

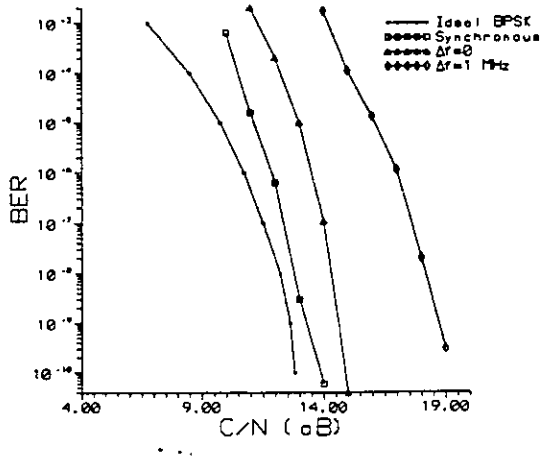

Fig. 8. BER performance of 8 Mb/s RZ BPSK signal under different carrier recovery conditions. These include (a) Ideal BPSK system, (b) synchronous BPSK system, (c) carrier recovery with oscillator with fixed carrier signal, and (d) carrier recovery with oscillator under frequency modulated carrier (Δf = 1 MHz) conditions.

where N_{0p} is the phase component of the oscillator noise, and k_d is the phase detector gain constant. The thermal noise contribution, assuming an input thermal noise-to-carrier ratio of $(N0/C)_{th}$ and a PLL phase noise slope of f^{-3} up to f_n, [15] is

$$V_{th}^2 = k_d^2 \left(\frac{N_0}{C}\right)_{th} \left(b - \frac{4}{5} f_n\right). \tag{8}$$

In the case of a locked carrier recovery oscillator operating at the signal frequency, no down- conversion is necessary, which removes the first contributor to noise. If we assume that the same expression for the thermal noise can be used for our oscillator, the higher natural frequency of the locked system will cause the second contributor to be smaller than for the PLL. The overall effect should be a carrier recovery scheme with lower noise.

III. Experimental Results

A. Amplification

STW devices usually have a lower Q than comparable SAW devices, and therefore provide a wider injection locking bandwidth. This makes them better suited to amplifier applications. In our measurements, we employed a STW resonator with a nominal center frequency of 1.012 GHz and a Q of 300 [12].

The locked amplifier exhibits inherent gain control [6]. At all injection levels above a −40-dBm threshold, the output power is in the −2- to 0-dBm range. This remains the case even when the injected signal exceeds the oscillator output power by as much as 48 dB. This behavior can be attributed to saturation in the loop amplifier.

This saturation does not, however, cause output signal distortion in constant envelope signals since the STW "cleans" the output spectrum. Fig. 5 shows the output waveform of the oscillator with a +16-dBm injected signal. Further examination on a spectrum analyzer determined that all harmonics were attenuated by at least 20 dB for this power level.

Conventional noise figure measurements cannot be performed on a locked oscillator because the process involves measuring the output with "hot" and "cold" noise sources. The signal level in both of these is usually insufficient to produce injection locking. One would expect, however, that the noise performance of the oscillator would be good since the gain control should prevent amplitude fluctuations from affecting the output. Similarly, the finite bandwidth of the locking process should limit the effect of any phase fluctuations.

In an attempt to obtain a measure of the noise contributions of the oscillator, it was placed at the end of a BPSK channel and the bit-error-rate (BER) was measured as a function of carrier-to-noise ratio for various additive white Gaussian (AWG) noise levels. In order to provide the injection locking bandwidth necessary to permit the use of the internal 2 Mb/s data generator in a HP 3764A digital transmission analyzer, the carrier power was increased to 7 dBm. The results for a $2^{15}-1$ bit pseudorandom bit sequence are shown in Fig. 6, which includes the curve for an ideal BPSK system. We see that the measurements closely follow the theoretical curve. In fact, replacing the locked oscillator with an HP 8447D amplifier had no noticeable effect of the BER. The points in Fig. 6 corresponding to carrier-to-noise ratios of 14.3 dB and 15.3 dB begin to deviate from the curve because their measurement required the deliberate injection of an error to remove a zero BER measurement.

B. Carrier Recovery

To demonstrate carrier recovery, the modulated input signal must exceed the injection locking bandwidth capabilities of the oscillator (the carrier must not). With reference to (5), this can be accomplished by increasing the Q of the feedback element in the oscillator, by reducing the signal power, or by increasing the data rate. The first alternative would require replacing the STW device with a higher-Q SAW resonator with the same center frequency. Our fabrication facilities did not permit us to do this. In our measurements, the other two techniques yielded similar results.

Fig. 7 shows the spectrum of a 8 Mb/s BPSK unipolar return-to-zero (RZ) pseudorandom sequence at the input and output of the locked oscillator. The input power is −15 dBm, which does not provide a sufficient injection bandwidth for the oscillator to track the data. The periodic peaks in the response are separated by the bit rate and are characteristic of unipolar return-to-zero (RZ) sequences. The center peak, corresponding to the carrier signal, is poorly defined at the input to the oscillator, and must be enhanced to be useful. This is accomplished very effectively at the output of the oscillator, where the carrier is enhanced by 9 dB. If this signal, with no additional filtering, is fed to the carrier input of the HP 3764A transmission analyzer, the BER can be measured as a function of the input carrier-to-noise ratio. This is shown in Fig. 8 along with the theoretical curve for an ideal BPSK system and the experimental curve for a synchronous system. Again

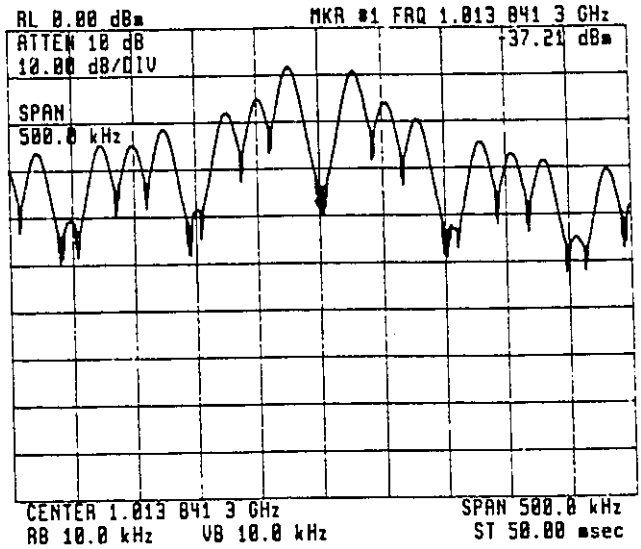

Fig. 9. Spectrum of 50 kb/s bipolar RZ QPSK signal after amplification with locked oscillator.

the measured points track the theoretical curve for BPSK, indicating good synchronization. The effective carrier-to-noise ratio is degraded by 1–1.5 dB over that of the synchronous system.

We also introduced a $\Delta f = 1$ MHz frequency modulation, at 1000 times per second, onto our carrier to examine the oscillator's ability to track the carrier. Examining Fig. 8, we note that this leads to an additional 3–4 dB loss in the effective C/N ratio.

IV. Discussion

The circuit is not limited to the amplification of BPSK signals, but can also be used to amplify quadrature phase-shift-keyed (QPSK) signals. Lack of equipment precluded a quantitative measurement of the circuit performance in this type of application. We were, however, able to assemble a CMOS circuit to generate bipolar RZ data streams for the in-phase (50 kb/s alternating bit sequence) and the quadrature (100 kb/s alternating bit sequence) channels of a QPSK system. These data were used to modulate a signal which was then fed into the oscillator for amplification. Fig. 9 shows the spectrum of the oscillator's output signal. It is clearly the sum of the spectrum of each of the channels, and indicates that the oscillator can be used to amplify QPSK signals.

The advantage of using a locked oscillator for carrier recovery is twofold. First, this technique eliminates the need for a phase-locked-loop, with its associated high-power consumption at UHF frequencies [14]. For an m-ary PSK system, the PLL must operate at the mth harmonic of the carrier in order to remove phase ambiguity [16], and this usually involves emitter-coupled logic (ECL). Second, the locked system has a lower probability of losing synchronization because it can react to carrier frequency changes several orders of magnitude faster than can PLL systems. While PLL time constants are usually in the tens of milliseconds [17], [18], the time constant of the STW oscillator is in the order of 10 μs. In fact, this limitation on PLL's is the major cause for the emergence of differential coding schemes [19] that do not require coherent carrier recovery, but that result in higher bit error rates.

V. Conclusion

This paper has discussed the use of STW resonator-based oscillators for low-noise amplification of binary phase-shift-keyed signals. We have shown that a locked oscillator, subject to data rate constraints, provides an almost constant 0-dBm output power for an input BPSK signal of between −40 and +48 dBm.

We have also demonstrated that the locked oscillator can provide carrier recovery of BPSK signals. This application has the potential of greatly reducing the complexity of conventional phase-locked loop systems. Experimental measurements confirm the validity of the technique.

Considerable work remains to be done on the subject of carrier recovery. In particular, a more rigorous analysis of the performance of a locked oscillator, specially for carrier recovery under fading conditions, is necessary.

Acknowledgment

We would like to thank Dr. Ivan D. Avramov, of the Institute of Solid State Physics, in Sofia, Bulgaria, for supplying us with the STW oscillator that was used in this study. This work was funded in part by grants from the Natural Sciences and Engineering Research Council of Canada.

REFERENCES

[1] B. van der Pol, "Forced oscillations in a circuit with nonlinear resistance," *Philosophical Mag.*, vol. 3, no. 13, pp. 65–80, Jan. 1927.
[2] R. Adler, "A study of locking phenomena in oscillators," *Proc. IRE*, vol. 34, no. 6, pp. 351–357, June 1946. (Reprinted in *Proc. IEEE*, vol. 61, no. 10, pp. 1380–1385, Oct. 1973.)
[3] L.J. Paciorek, "Injection locking of oscillators," *Proc. IEEE*, vol. 53, no. 11, pp. 1723–1727, Nov. 1965.
[4] K. Kurokawa, "Injection locking of microwave solid-state oscillators," *Proc. IEEE*, vol. 61, no. 10, pp. 1386–1410, Oct. 1973. (Contains more than 150 references on the subject.)
[5] C. W. Carnahan and H. P. Kalmus, "Synchronized oscillators as FM receiver limiters," *Electron.*, vol. 17, no. 8, p. 108, Aug. 1944.
[6] P. M. Smith, P. J. Edmonson, and C. K. Campbell, "An automatic gain controlled oscillating amplifier," *Electron. Letters*, vol. 27, no. 21, pp. 1919–1921, Oct. 1991.
[7] Y. Fukatsu and H. Kato, "Frequency conversion with gain through sideband locking of an IMPATT diode oscillation," *Proc. IEEE*, vol. 57, no. 3, pp. 342–343, Mar. 1969.
[8] C. L. Ruthroff, "Injection-locked-oscillator FM receiver analysis," *Bell Syst. Tech. J.*, vol. 47, no. 8, pp. 1653–1661, Oct. 1968.
[9] T. E. Parker and G. K. Montress, "Precision surface-acoustic-wave (SAW) oscillators," *IEEE Trans. Ultrason., Ferroelec., Freq. Contr.*, vol. UFFC-35, no. 3, pp. 342–364, May 1988.
[10] J. J. Gagnepain, "Rayleigh wave resonators and oscillators," in *Rayleigh-Wave Theory and Application*, E. A. Ash and E. G. S. Paige, Eds. New York: Springer-Verlag, 1985, pp. 151- 172.
[11] C. K. Campbell, P. J. Edmonson, and P. M. Smith, "The phase noise characteristics of a driven SAW oscillator in the threshold vicinity for injection locking," *Proc. 1985 IEEE Ultrason. Symp.*, San Francisco, CA, Oct. 16–18, 1985, pp. 283–286.
[12] I. D. Avramov, P. J. Edmonson, and P. M. Smith, "A surface transverse wave-based MSK system," *IEEE Trans. Ultrason., Ferroelec., Freq. Contr.*, vol. 38, pp. 194–198, May 1991.
[13] R. Groshong and S. Ruscak, "Exploit digital advantages in a SSB receiver," *Electron. Design*, vol. 39, no. 11, pp. 89–96, June 1991.
[14] S. Saito, Y. Tarusawa, and H. Suzuki, "State-preserving intermittently locked loop (SPILL) frequency synthesizer for portable radio," *IEEE Trans. Microwave Theory Tech.*, vol. MTT-37, no. 12, pp. 1898–1903, Dec. 1989.
[15] W. P. Robins, *Phase Noise in Signal Sources*. London: Peregrinus, 1982, pp. 246–275.
[16] L. W. Couch, *Digital and Analog Communication Systems*. New York: MacMillan, 1990.
[17] R. E. Best, *Phase-locked Loops*. New York: McGraw-Hill, 1984.
[18] S. Hao and Y. Puqiang, "A high lock-in speed digital phase-locked loop," *IEEE Trans. Commun.*, vol. 39, pp. 365–368, Mar. 1991.
[19] H. Leib and S. Pasupathy, "Trellis-coded differentially coherent (TCDC) MPSK with carrier-phase-noise," *IEEE Trans. Commun.*, vol. 39, pp. 877–886, June 1991.

Peter J. Edmonson (S'74–M'80) was born in Hamilton, ON, on August 8, 1951. He received the diploma in electronics technology from Mohawk College, Hamilton, ON, in 1973 and obtained the B.Eng. and M.Eng. degrees in electrical engineering from McMaster University, Hamilton, ON, in 1980 and 1989, respectively.

He was a Technologist in the SAW Device Laboratory at McMaster University from 1973 to 1979. From 1980 to 1982 he worked at ComDev Ltd., Cambridge, ON, where he was involved in the development of their SAW facilities. Since 1982 he has been engaged in research and development of SAW devices and applications at McMaster University. In 1983 he joined Mohawk College as a faculty member with the Department of Electrotechnology, and in 1991 he became a part-time lecturer at McMaster University.

Mr. Edmonson is a member of the Association of Professional Engineers of the Province of Ontario.

Peter M. Smith (S'80–M'88) was born in Belo Horizonte, Brazil, on December 15, 1959. He received the B.Eng.Mgt. degree in computer engineering and the M.Eng. and Ph.D. degrees in electrical engineering from McMaster University, Hamilton, ON, in 1983, 1985, and 1988, respectively. While in graduate school, he worked on phase noise in oscillators, on multiband and low-loss surface-acoustic-wave filters.

He has been an Assistant Professor with the Department of Electrical and Computer Engineering at McMaster University since 1987. His research interests are on the application of acoustic and heterojunction devices to microwave systems.

C. K. Campbell (M'56–SM'67–F'86), was born in St. Andrews, Scotland, in 1927. He received the Honors B.Sc. degree in electrical engineering in 1925 and the Ph.D. degree in low-temperature physics in 1960, from St. Andrews University, St. Andrews, Scotland, as well as the D.Sc. degree in engineering and applied science in 1984 from the University of Dundee, Dundee, Scotland. He attended the Massachusetts Institute of Technology, Cambridge, MA, twice on scholarships, including the Massachusetts Golf Scholarship, where he received the S.M. degree in electrical engineering in 1953 for a thesis on power and machines. As a graduate student in 1959 he was an Invited Member of the British research student delegation to the Meeting of Nobel Physics Prize Winners in Lindau, Germany.

He was with McMaster University, Hamilton, ON, Canada, from 1960 to 1989, where he was a Professor of Electrical and Computer Engineering. At McMaster University he received three citations for outstanding contributions to university teaching, including one from the Ontario Minister of Colleges and Universities. He is now an independent consultant based in Ontario. An experimentalist by training and inclination he has conducted research in a wide range of fields, including low-temperature superconductivity, masers, magnetic amplifiers, giant-pulse laser oscillators and amplifiers, dielectrics, VLSI, millimeter-wave instrumentation, power-transistor design, high-voltage ceramics, distributed-parameter devices, and SAW devices. He is the author of a 1989 textbook on SAW devices and SAW signal processing.

Dr. Campbell is a Fellow of the Royal Society of Canada, a Fellow of the Engineering Institute of Canada, a Fellow of the Royal Society of Arts (London), a Member of the Electromagnetics Academy, and a member of Sigma Xi. He holds "The Inventor" insignia from Canadian Patents and Development Ltd. In 1983 he was awarded the Eadie Medal of the Royal Society of Canada, for major contributions to engineering and applied science in Canada.

APPENDIX F

SAW-Based Carrier Recovery Without Phase Ambiguity for 915 MHz BPSK Wireless Digital Communications

P.J. Edmonson*, P.M. Smith# and C.K. Campbell#

* Dept. of Electrotechnology
Mohawk College, Hamilton, Ontario, Canada L8N 3T2

Dept. of Electrical and Computer Engineering
McMaster University, Hamilton, Ontario, Canada L8S 4L7

Abstract

This paper describes a SAW-based non-linear carrier recovery system for wireless digital communications employing a 915 MHz injection-locked SAW oscillator for demodulation of 2 Mb/s and 8 Mb/s Binary Phase Shift Keying (BPSK) input signals. The circuit does not permit the injection-locked SAW oscillator to follow the abrupt phase changes in the input BPSK signals, but assumes an output signal with a unique frequency signature that was dependent on the input phase transition. The paper includes measurements of the SAW oscillator phase noise, together with receiver input and output spectra and waveforms. As well, an indoor 915 MHz radio transmitter was used with this SAW-based carrier recovery circuit for measurements of bit-error-rate (BER) under fading and non-fading conditions, yielding BERs of less than 4×10^{-4} for 2 Mb/s and 8 Mb/s BPSK signals at 915 MHz, without differential encoding, using a digital transmission analyzer with 2^{15}-1 pseudo-random code length.

Introduction

As we approach the end of the twentieth century, it is becoming clear that the next generation of communication systems will be dominated by wireless personal communication systems linked to wideband fibre optic networks [1]. These personal systems will be digital in nature and will have to provide a great deal of flexibility in the transmission of both voice and data information. This poses significant challenges, particularly in view of the required low cost of consumer electronics.

One of the simplest digital modulation schemes involves Binary Phase Shift Keying (BPSK) the signal. BPSK systems employ a conventional Phase-Locked Loop (PLL) carrier recovery circuit in the receiver. This circuit first squares the modulated input to remove the phase transitions, and then uses the resulting signal as a reference for its internal Voltage Controlled Oscillator (VCO). The frequency of the output is then divided by two to produce a carrier.

PLL or Costas Loops (a special case of a PLL) exhibit very slow recovery after synchronization loss due to signal fading because their natural loop frequencies are in the order of about 2 kHz or less. In addition, the output carrier signal contains a 180° phase ambiguity that results from the squaring operation. This very serious problem is usually overcome by differentially encoding (DBPSK) the signal, thus providing the necessary memory element to correctly decode the data.

Injection-Locked Oscillators (ILOs) have been shown to perform a number of communication system functions. They are able to track and amplify BPSK waveforms if the bit rate is slow enough and the Q of the ILO is sufficiently low [2]-[3]. If the Q or bit rate are increased beyond a threshold, the ILO can no longer follow the abrupt phase changes and the output will retain information dependent on the initial phase transition that occured in the transmitter. This resulting memory allows the circuit to be used for carrier recovery without phase ambiguity.

This paper will outline the ILO theory and will explain the carrier recovery process. The application of ILO to the carrier recovery of a wireless signal will be described in a laboratory setting. Measured Bit Error Rates (BER) will demonstrate the performance capabilities of the circuit.

Theory

When a previously locked PLL is subjected to a small frequency change in the input signal, the loop goes through a re-locking process that results in a phase difference between the VCO and the input signal. This produces, at the output of a phase detector, an error voltage that is fed back to the VCO and sufficiently alters the frequency. The theory of VCOs is presented in most communications textbooks.

The nonlinear equations describing ILO are identical to those for a PLL [4], even though the circuit is quite different. In the case of an ILO, an independent signal is injected into the oscillator loop as shown in Figure 1. This independent signal is, in our case, a BPSK encoded waveform originating from a transmitter (TX).

The TX is comprised of a four-diode balanced mixer whose inputs are a data stream and a carrier. Here, the 0 to 1 transition is characterized by two of the diodes becoming forward biased and the two other ones becoming

1051-0117/92/0000-0241 $1.00 © 1992 IEEE

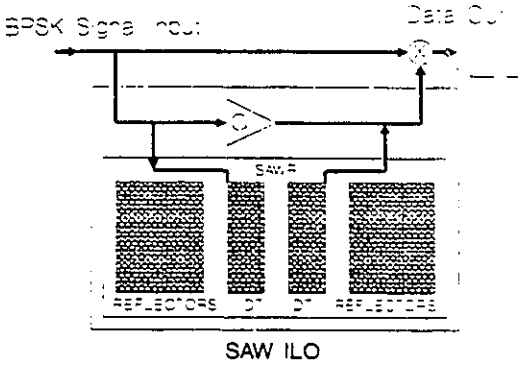

Figure 1: Block diagram of an Injected Locked Oscillator (ILO).

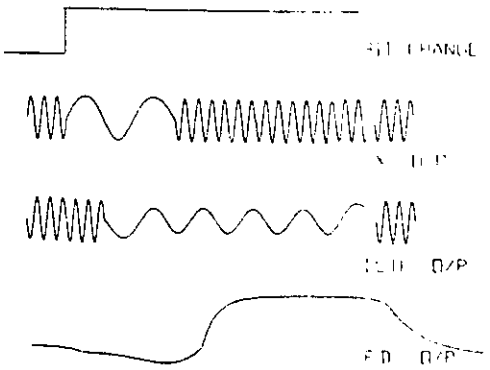

Figure 2: Inputs to and output from the receiver phase detector during 0 to 1 bit transition.

reverse biased. The 1 to 0 transition is characterized by the converse situation. These transitions are not the same, and this results in a unique frequency content signature for each of the transitions. In fact, the 0° to 180° transition will be characterized by a small increase in frequency and the 180° to 0° transition will cause a small decrease in frequency.

At the receiver, each bit transition subjects the ILO to this small positive or negative frequency change. If the parameters of the loop are suitably chosen, the loop partially looses synchronization but then re-locks itself within the bit period. During the transition time, Adler has demonstrated that the phase within the loop follows the relationship between the phase error α and time by [5]

$$\alpha(t) = 2\arctan\left[\frac{1}{K} + \frac{\sqrt{K^2-1}}{K}\tan\left(B\,\frac{(t-t_0)}{2}\sqrt{K^2-1}\right)\right]$$

where K is normalized frequency offset of the injected signal given by

$$K = \frac{\Delta\omega_0}{B}$$

in which B is the injection locking bandwidth

$$B = \frac{V_{inj}}{V_{osc}}\,\frac{\omega_0}{2Q}$$

As an example, a 0 to 1 transition in the transmitter will cause a small momentary decrease in the frequency of the carrier. When input into the ILO, this will result in a partial loss of synchronization during which time the phase of the ILO will slowly catch up with that of the signal as described by the equation for $\alpha(t)$ (see Figure 2). This will cause a voltage pulse at the output of the receiver mixer that will match the 0 to 1 transition. A similar behaviour will be observed with a 1 to 0 transition. Since the output of the receiver is a function of the signal transitions, and since the 0 to 1 and the 1 to 0 transitions are not the same, the circuit is able to correctly recover the data without ambiguity.

The ILO circuit also offers an advantage in terms of additive phase noise. Robins [6] studied the effect of noise in a PLL carrier recovery system for BPSK. He showed that the thermal noise contribution, assuming an input thermal noise to carrier ratio of $(N_0/C)_{in}$ and a PLL phase noise slope of f^{-3} up to the natural loop frequency f_n, is [6]

$$V_{in}^2 = k_d^2\left(\frac{N_0}{C}\right)_{in}\left(b - \frac{4}{5}f_n\right)$$

where k_d is the gain of the phase detector and b is the bit rate. The natural frequency of the SAW oscillator ($f_n > 50$ kHz) is two orders of magnitude larger than for a PLL and should therefore, give an ILO carrier recovery circuit a better noise performance [7].

Experiment

A communications channel consisting of a transmitter and a receiver connected to dipole antennas (see Figure 3) was constructed in order to evaluate the performance of the ILO circuit. The SAW oscillator that is used for carrier recovery is characterized by a Single Sideband (SSB) phase noise of -100 dBc/Hz at 1 kHz offset. An HP 3764A digital transmission analyzer generated a 2^{15}-1 pseudo-random code and monitored the decoded data to compute the bit-error-rate (BER). The wireless cell layout, which consisted of the Microwave Acoustics Laboratory at McMaster University, is shown in Figure 4. A non-line-of-sight signal path, in combination with a large number of metal obstacles within the cell, provided a good fading environment to test the system [8].

The 915 MHz return-to-zero (RZ) BPSK system in Figure 3 was first characterized synchronously by removing the SAW-based carrier recovery and connecting the HP 8662A synthesizer directly to the receiver mixer. The BER

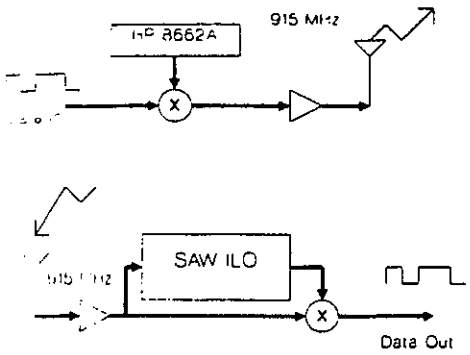

Figure 3: Transmitter and receiver circuits of communication system.

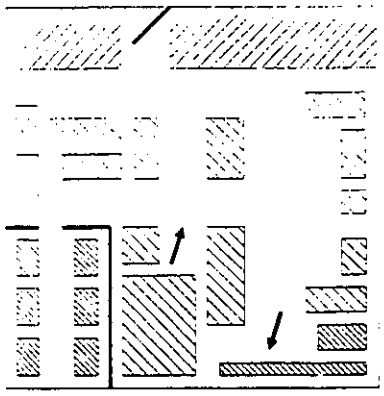

Figure 4: Wireless cell layout. Arrows indicate location of dipole antennas.

was measured to be 5×10^{-10}, and the connection to the HP 8662A was then replaced with the ILO.

The spectrum at the input to the receiver, with the characteristic spikes associated with unipolar RZ data, is shown in Figure 5 (a). Part (b) of the figure shows the output of the SAW ILO. A summary of the BER performance of the receiver employing a carrier recovered with the ILO is given in Table I for various coding and bit rate schemes. These results were obtained without the use of differential encoding.

Conclusions

We have demonstrated that a SAW injection-locked oscillator can be used to recover an unambiguous carrier of a 2 Mb/s and of a 8 Mb/s BPSK systems operating at 915 MHz under both fading and non-fading conditions. While

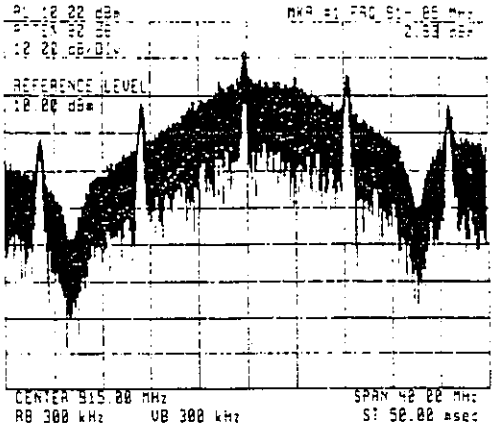

(a)

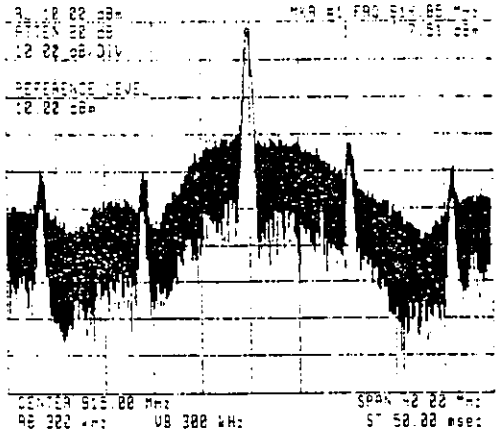

(b)

Figure 5: Spectrum (a) at input to ILO and (b) at output from ILO for 8 Mb/s RZ data.

certain transmitter diode mixer systems may cause the output bits from this receiver to be inverted, this can be easily corrected by placing a hardware inverter at the output of the receiver.

The ILO thus provides an alternative to phase-locked loop systems in fixed frequency data links. Its fast acquisition makes it suitable for time division multiple access (TDMA). In addition, the lower component count would save power while at the same time reducing costs.

Acknowledgements

This work was supported in part by grants from the Natural Science and Engineering Research Council of Canada. The authors would like to thank RF Monolithics, of Dallas, TX, for supplying the SAW resonators used in this study.

References

[1] K.A. Wimmer and J.Barclay Jones, "Global Development of PCS," *IEEE Communications Magazine*, vol. 30, no. 6, pp.22-27, June 1992.

[2] V. Uzunoglu and M.H. White, "The Synchronous Oscillator: A Synchronization and Tracking Network," *IEEE Journal of Solid-State Circuits*, vol. SC-20, no. 6, pp. 1214-1226, December 1985.

[3] P.J. Edmonson, P.M. Smith and C.K. Campbell, "Injection Locking Techniques for a 1-GHz Digital Receiver Using Acoustic-Wave Devices," *IEEE Trans. on Ultrasonics, Ferroelectrics and Frequency Control*, vol. 39, no. 5, pp. 631-637, September 1992.

[4] L.W. Couch, "A Study of a Driven Oscillator with FM Feedback by Use of a Phase-Lock-Loop Model," *IEEE Trans. on Microwave Theory and Techniques*, vol. MTT-19, no. 4, pp.357-366, April 1971.

[5] R. Adler, "A study of locking phenomena in oscillators," *Proceedings of the IRE*, vol 34, no. 6, pp.351-357, June 1946. Reprinted in *Proceedings of the IEEE*, vol 61, no. 10, pp. 1380-1385, October 1973.

[6] W.P. Robins, *Phase Noise in Signal Sources*, London: Peregrimus, 1982, pp. 246-275.

[7] C.K. Campbell, P.M. Smith and P.J. Edmonson, "The phase noise characteristics of a driven SAW oscillator in the threshold vicinity for injection locking," *1985 IEEE Ultrasonics Symposium Proceedings*, San Francisco, CA, pp. 283-286, 16-18 October 1985.

[8] K. Brayer (Ed.), *Data Communications Via Fading Channels*, IEEE Press, New York, 1975.

APPENDIX G

BASICS OF SURFACE ACOUSTIC WAVES AND PIEZOELECTRICITY

G.1 Introduction

The experimental acoustic wave devices that were used in this thesis all worked on a conversion process that transformed electromagnetic signals into acoustic wave energy and visa versa. The conversion process is attributed to a phenomena called piezoelectricity.

The creation of surface acoustic waves is achieved by applying an electromagnetic signal to the metal IDTs placed on the surface of a piezoelectric solid as was previously illustrated in Fig. 2.1 and Fig. 2.3. These surface acoustic waves are called Rayleigh waves [3] and are combinations of both longitudinal and shear (transverse) motions.

This appendix will briefly describe the essential properties of acoustic wave devices. The material, stress and strain parameters of acoustic waves are tensor quantities. A short study of these parameters will be contained here, further detailed descriptions of acoustic wave properties can be found in references [3], [57] - [63]. Finally, two of the most important practical properties relating to surface wave propagation on a piezoelectric substrate will be discussed. These are the SAW velocity v and the electromechanical coupling coefficient K^2 of the piezoelectric material.

G.2 Mechanical Motions of Acoustic Waves

To assist in characterizing the motion of acoustic waves, a thin rectangular slab of a nonpiezoelectric elastic solid is first considered. The length (x axis) is the long dimension and the thickness of the slab (y axis) is sufficiently small with respect to an acoustic wavelength but large when compared to the atomic spacing. The z axis is the width of the slab. This slab is then subjected to a force that is applied normal to the y-z plane unit area. Stress can be defined as the force F applied per unit area A of the slab. The stress, force and area relationship can be represented as vector quantities (bold face) such that $\mathbf{T} = \mathbf{F} / \mathbf{A}$. The units of stress are N/m^2 when force F is expressed in newtons (N). The strain parameter S, represents the fractional deformation of the slab due to force F, and can be expressed as $\mathbf{S} = \Delta / \mathbf{L}$ (dimensionless), where Δ is the fractional deformation of the slab of an axis of length L [3].

When applied within an elastic solid, stresses and strains can exist in compressional or shear form and can be related proportionally by Hooke's Law for elastic deformations. For simple compressional stress and strain along the same axis as shown in a grid diagram of Fig. G.1 for a longitudinal wave, this relationship can be written as

$$T = cS \quad , \tag{G.1}$$

where c = elastic stiffness coefficient, also known as Young's modulus (N/m^2) [3].

The longitudinal wave of Fig. G.1 is also referred to as a compressional wave and causes a change in the volume of the material. This can be seen as the number of nodes per unit volume will change as the compression wave travel along the X axis [60].

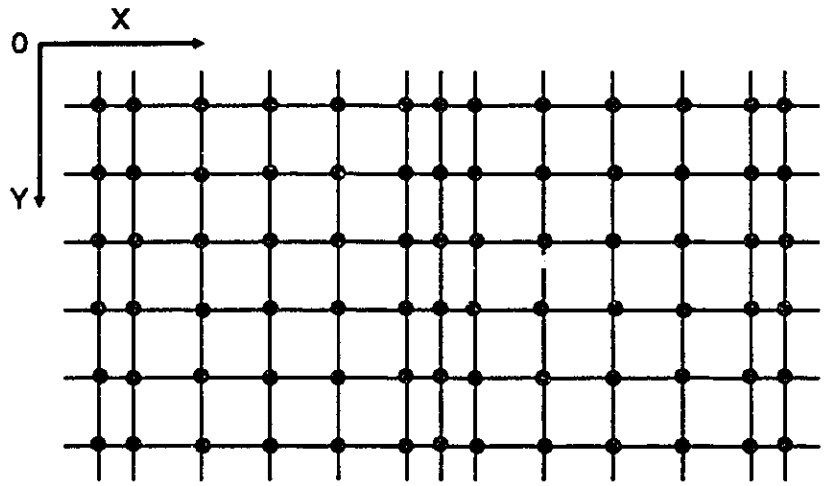

Figure G. 1 Longitudinal wave (compression wave)

The shear wave has a rotational propagation means. This involves a rotation of the material volume without actually changing the volume as depicted in Fig. G.2.

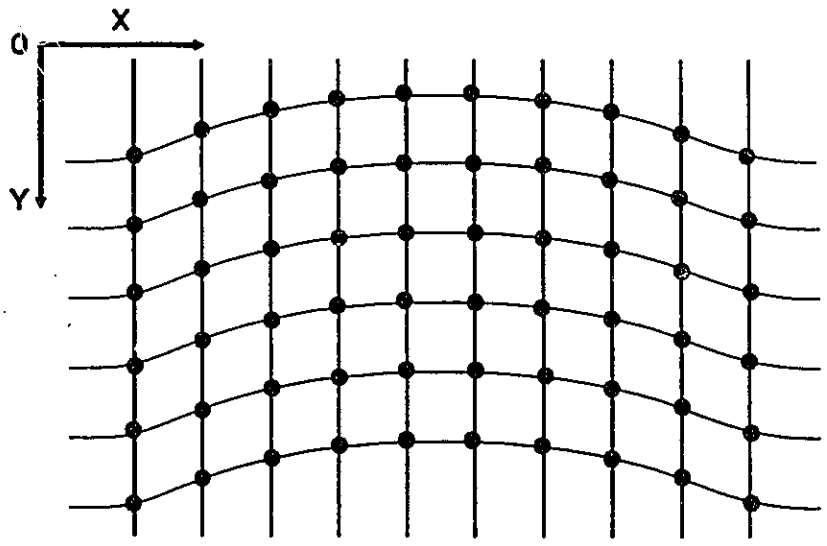

Figure G.2 Shear wave (rotational wave)

When the two longitudinal and shear waves of the previous two figures are combined and are coupled by a boundary surface, a Rayleigh or surface acoustic wave is produced. This wave is illustrated in Fig. G.3 and can propagate along the X axis. The amplitude decays quite rapidly in the Y direction to a very small value after a depth of a few acoustic wavelengths .

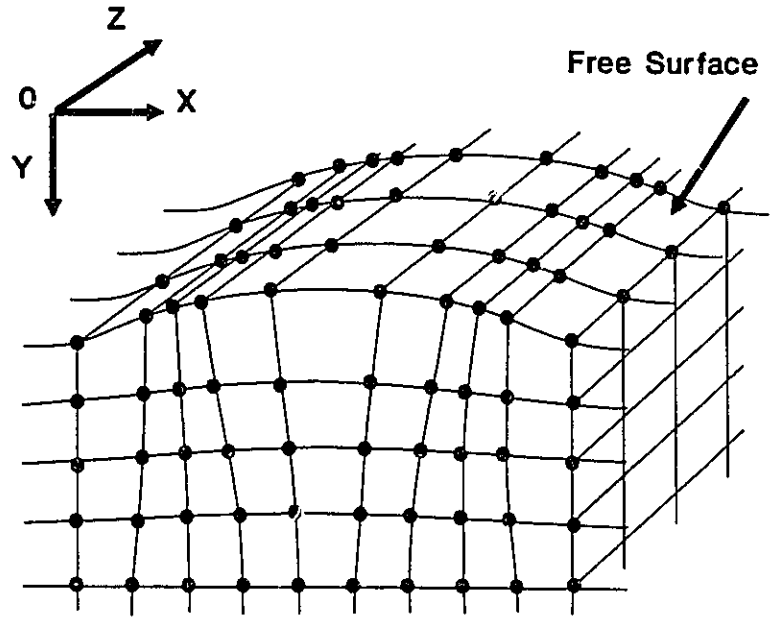

Figure G.3 A grid diagram depicting SAW propagation along the X axis.

G.3 Constitutive Relations in a Piezoelectric Elastic Solid

This section will consider the relations between mechanical parameters, stress **T** and strain **S** and the electromagnetic parameters, electric displacement **D**, electric field **E** and the permittivity ε for small static deformations of a piezoelectric elastic solid. An application of an electrical field to a nonpiezoelectric dielectric elastic solid would have no effect on its mechanical stress-strain characteristics. To analyze the effects of applying an electric field of intensity **E** (V/m) to a simple nonpiezoelectric dielectric, the electrical relationships for a simple parallel-plate capacitor containing a solid insulator will be considered. The electric field **E** established by applying a voltage V across the metallized plates will cause a distortion in one dimension, of the otherwise neutral molecular charge distributions in the insulator. This will cause an accumulation of surface charge on the capacitor plates. The electric displacement **D** (C/m^2) will be proportionally related to **E** by

$$\boldsymbol{D} = \epsilon_r \epsilon_o \boldsymbol{E} = \epsilon \boldsymbol{E} \quad , \tag{G.2}$$

where ε_r = relative dielectric permittivity, and ε_0 = permittivity of free space = 8.856 x 10^{-12} F/m [3], [60].

The piezoelectric constitutive relations associate the mechanical stress and strain (**S**,**T**) with the electric field and electric displacement (**E**,**D**) variables. The relation presented in eqn (G.2) will no longer be valid for piezoelectric dielectrics because of the coupling between the electric and mechanical parameters. An application of an electric field stimulus to an IDT situated on the surface of a piezoelectric crystal will give rise

to mechanical deformations and vice versa. This interaction can be expressed in terms of a piezoelectric constant matrix [e] with units of C/m^2. The electrical displacement **D** is then given by a Taylor expansion [60], from the one dimensional case shown previously in eqn (G.2) as (with all derivation to be considered with partial derivatives)

$$D = \left(\frac{\delta D}{\delta S}\right)_E S + \left(\frac{\delta D}{\delta E}\right)_S E \ , \qquad \text{(G.3)}$$

where **S** = strain and **E** = electric field intensity and the subscripts indicate that the experimental conditions are measured at zero or constant strain (S) or electric field (E).

In a similar fashion, the strain (T) relationship of eqn (G.1) can be modified to accommodate the effects of a piezoelectric material to produce

$$T = \left(\frac{\delta T}{\delta S}\right)_E S + \left(\frac{\delta T}{\delta E}\right)_S E \ . \qquad \text{(G.4)}$$

The material constants of the above equations are,

$$c^E = \left(\frac{\delta T}{\delta S}\right)_E = \textit{elastic stiffness constant} \qquad \text{(G.5a)}$$

$$e^E = \left(\frac{\delta D}{\delta S}\right)_E = \textit{piezoelectric constant} \qquad \text{(G.5b)}$$

$$e^S = \left(\frac{\delta T}{\delta E}\right)_S = \textit{piezoelectric constant} \qquad \text{(G.5c)}$$

$$\epsilon^S = \left(\frac{\delta D}{\delta E}\right)_S = \textit{permittivity constant} . \qquad \text{(G.5d)}$$

These material constants allow a *piezoelectric coupling* to take place as was seen in eqn (G.3) where the strain (S) is coupled to the effects of the electric displacement (D) and the electric field (E) by the piezoelectric constant e^E. The two piezoelectric constants are related, from [60],

$$- e^S = e^E = e , \qquad \text{(G.6)}$$

allowing eqns (G.3 and G.4) to be re-written as

$$\boldsymbol{D} = e\,\boldsymbol{S} + \epsilon^S \boldsymbol{E} , \qquad \text{(G.7a)}$$

$$\boldsymbol{T} = c^E \boldsymbol{S} - e\,\boldsymbol{E} . \qquad \text{(G.7b)}$$

The material solids used for the analysis of the piezoelectric effect so far may not always be isotropic. The above equations describing the displacement and stress must therefore be expressed in terms of tensor quantities. The following section will explain the tensor relationship of eqn (G.7a), starting with the definition of the electric displacement ($\mathbf{D}_i$) and electric field ($\mathbf{E}_j$) parameters as,

$$[\, D_i \,] = \begin{bmatrix} D_x \\ D_y \\ D_z \end{bmatrix} , \tag{G.8a}$$

$$[\, E_j \,] = \begin{bmatrix} E_x \\ E_y \\ E_z \end{bmatrix} . \tag{G.8b}$$

The dielectric tensor ε_{ij} that will replace the permittivity constant of eqn (G.5d) is a second-order symmetric tensor with $\varepsilon_{ij} = \varepsilon_{ji}$, and having six independent variables

$$[\, \epsilon^S_{ij} \,] = \begin{bmatrix} \epsilon^S_{xx} & \epsilon^S_{xy} & \epsilon^S_{xz} \\ \epsilon^S_{xy} & \epsilon^S_{yy} & \epsilon^S_{yz} \\ \epsilon^S_{xz} & \epsilon^S_{yz} & \epsilon^S_{zz} \end{bmatrix} . \tag{G.9}$$

The piezoelectric tensor e_{ijk} that will replace the piezoelectric constant of eqn (G.5b) is a third-rank tensor with $e_{ijk} = e_{ikj}$. The last two indices j and k are symmetric due to the symmetry in the strain and stress tensors. The following notation is used to define these six indices along with each of the corresponding strain component [63].

Indices j k	Notation J	Corresponding strain
xx	1	longitudinal in x direction
yy	2	longitudinal in y direction
zz	3	longitudinal in z direction
yz = zy	4	shear y - z
xz = zx	5	shear z - x
xy = yx	6	shear x - y

The piezoelectric stress tensor can then be written with $e_{i\,J} = e_{i\,j\,k}$ and i = x, y, z ; and J = 1 to 6

$$[\, e_{i\,J} \,] = \begin{bmatrix} e_{x1} & e_{x2} & e_{x3} & e_{x4} & e_{x5} & e_{x6} \\ e_{y1} & e_{y2} & e_{y3} & e_{y4} & e_{y5} & e_{y6} \\ e_{z1} & e_{z2} & e_{z3} & e_{z4} & e_{z5} & e_{z6} \end{bmatrix} . \qquad \text{(G.10)}$$

For lithium niobate piezoelectric with trigonal crystal classification, for which most of the devices used in chapters 3, 4 and 5 in this Thesis were fabricated on, $[e_{i\,J}]$ is then

$$[\, e_{i\,J} \,] = \begin{bmatrix} 0 & 0 & 0 & 0 & e_{x5} & -e_{y2} \\ -e_{y2} & e_{y2} & 0 & e_{x5} & 0 & 0 \\ e_{z1} & e_{z1} & e_{z3} & 0 & 0 & 0 \end{bmatrix} . \qquad \text{(G.11)}$$

G.4 SAW Velocity and the Electromechanical Coupling Coefficient

The electromechanical coupling coefficient K^2 is a measure of the efficiency of a given piezoelectric material in converting an applied electrical signal into mechanical energy associated with a surface acoustic wave. K^2 and SAW velocity v represents the two most important practical material parameters used in SAW device design.

The coefficient K^2 can be defined for acoustic waves on a piezoelectric material in terms of the piezoelectric constant [e], the elastic constant [c] and the dielectric permittivity [ε] (with tensor notation deleted) [3], as

$$K^2 = \frac{e^2}{c\,\epsilon} . \qquad (G.12)$$

Since K^2 values are small, they are usually expressed as percentages. Another method of determining K^2 is done experimentally. This is accomplished by observing the change in the SAW velocity v, when the free surface of the piezoelectric material is shorted by a thin conducting metal film. The electric field (E) associated with the propagating wave will cause a charge to accumulate on the metal surface. Using an equivalent electrical transmission line for analysis with distributed inductance - capacitance (L-C) parameters, an increase in charge will appear as an increase in capacitance (C). The relationship of an electromagnetic wave velocity on an electrical transmission line is $v_{em} = (LC)^{1/2}$, which decreases v_{em} by Δv as the capacitance increases. Therefore for a SAW transmission line model a similar decrease in velocity will occur when a conducting metal film is placed on the piezoelectric surface. By determining the Δv of the SAW the coupling coefficient can be

$$K^2 = \frac{-2\,\Delta v}{v} . \qquad \text{(G.13)}$$

The leaky waves that were described in chapter six of this thesis differ from the surface waves in a fashion such that, as they propagate, they leak their energy successively into the interior of the solid. This phenomenon occurs because the SAW velocity is larger than the shear wave velocity [60], [63].

Velocity and coupling coefficient values for some typical piezoelectric substrates are given in Table G.1 on the following page.

Table G.1

Some Current SAW/SSBW/LSAW Piezoelectric Crystal Substrates

Substrate	Wave Type	Velocity (m/s)	K^2 (%)
ST-quartz	SAW	3158	0.14
YZ-$LiNbO_3$	SAW	3488	4.5
Rotated Y-cut ST-quartz	SSBW	4990	1.89
64° X-prop $LiNbO_3$	LSAW	4742	11.3

REFERENCES

[1] R. Schneiderman, *Wireless Personal Communications,* IEEE Press, New York, 1994.

[2] C.K. Campbell, "Applications of surface acoustic and shallow bulk acoustic wave devices," *Proc. of the IEEE,* Vol. 77, No. 10, pp. 1453-1484, October , 1989.

[3] C.K. Campbell, *Surface Acoustic Wave Devices and Their Signal Processing Applications*. Academic Press, Boston, Mass., 1989.

[4] C.K. Campbell, "SAW oscillators and resonators," in K. Shibayama (ed), *Proc. Int. Symp. SAW Devices for Mobile Comm.* Tokyo Press, Tokyo, Japan, pp. 171-178, 1992.

[5] G. Fischerauer and I. Schropp, "Influence of fabrication tolerences and circuit variations on the performance of SAW RF filters,"*Proc. 1993 IEEE Ultrasonics Symp.*, Oct. 31-Nov. 3, 1993, Baltimore, MD, IEEE Cat. No. 93CH3301-9, pp. 257-261, 1993.

[6] R.M. White and F.W. Voltmer, "Direct piezoelectric coupling to surface elastic waves," *Appl. Phy. Lett.*, Vol. 7, pp. 314-316, Dec. 1965.

[7] C.S. Hartmann and V.P. Plessky, private communication.

[8] W.S. Jones, C.S. Hartmann and T.D. Sturdivant, "Second order effects in surface wave devices," *IEEE Trans. Sonics and Ultrasonics*, Vol. SU-19, No. 3, pp. 368-377, July, 1972.

[9] D.C. Malocha, "Surface acoustic wave filters," in R.C. Dorf (ed), *The Electrical Engineering Handbook*, CRC Press, Boca Raton, Florida, Chapter 45, 1993.

[10] H.A. Haus, *Waves and Fields in Optoelectronics*, Prentice-Hall, New Jersey, 1984.

[11] P.J. Edmonson and C.K. Campbell "Radiation conductance and grating reflectivity weighting parameters for dual mode leaky-SAW resonator filter design, "*Proc. 1994 IEEE Ultrasonics Symp.*, 1-4 November, Cannes, France, IEEE Cat. No. 94CH3468-6, pp. 75-79, 1994. See Appendix C.

[12] E.A. Ash, "Surface wave grating reflectors and resonators," *Proc. 1970 IEEE MTT Symposium*, pp. 385-386, May, 1970.

[13] G.K. Montress and T.E. Parker, *High Stability SAW oscillators: Design and Performance*, Short Course presented at the 1991 IEEE UFFC Symposium.

[14] B. van der Pol, "Forced oscillations in a circuit with nonlinear resistance," *Philosophical Magazine*, Vol. 3, No. 13, pp. 65-80, January, 1927.

[15] R. Adler "A study of locking phenomena in oscillators," *Proceedings of the IRE*, Vol. 34, No. 6, pp. 351-367, June 1946.

[16] T.L. Osborne, "Amplitude behaviour of injection-locked oscillators," *IEEE Trans. on Microwave Theory and Techniques*, Vol. MTT-18, No. 11, pp. 897-905, Nov., 1970.

[17] C.J. Buczek, R.J. Freiberg and M.L. Skolnick, "Laser injection locking," *Proc. of the IEEE*, Vol. 61, No. 10, pp. 1411-1431, Oct., 1973.

[18] P.J. Edmonson, P.M. Smith and C.K. Campbell, "Injection locked oscillators: Dynamic behaviour and applications to neural networks,"*Proc 1993 IEEE Ultrasonics Symp.*, Oct. 31-Nov. 3, 1993, Baltimore, MY, IEEE Cat. No. 93CH3301-9, pp.131-135, 1993. See Appendix D.

[19] C.K. Campbell, "FM demodulation at UHF frequencies using an injection-locked SAW oscillator," *IEEE Trans. on Sonics and Ultrasonics*, Vol SU-29, No. 6, pp. 310-316, Nov., 1982.

[20] C.K. Campbell, P.J. Edmonson and P.M. Smith, "Effect of amplifier saturation on one-sided beat spectrum of driven unlocked oscillator," *Electronics Letters*, Vol 28, No. 12, pp. 1121-1122, June, 1992.

[21] L.W. Couch, *Digital and Analog Communication Systems*, MacMillan, New York, 1990.

[22] W.P. Robins, *Phase Noise in Signal Sources*, London: Peregrimus, 1982,

[23] C.B. Saw, C.K. Campbell, P.J. Edmonson and P.M. Smith, "Multifrequency pulsed injection-locked oscillator using a novel, low-loss SAW comb filter," *Proc. 1986 IEEE Ultrasonics Symp.*, Williamsburg, Nov. 17-19 1986 VA, Vol. 1, IEEE Cat. No. 86CH2375-4 pp. 273-276, 1986.

[24] C.B. Saw, P.M. Smith, P.J. Edmonson and C.K. Campbell, "Mode selection in a multimode SAW oscillator using FM chirp mixing signal injection," *IEEE Trans. on Ultrasonics, Ferroelectrics and Frequency Control*, Vol. UFFC-35, No. 3, May, 1988.

[25] I.D. Avramov, P.J. Edmonson and P.M. Smith, "Surface transverse wave based FM modulator/demodulator," *Electronics Letters*, Vol. 26, No. 6, pp. 364-365, March 1990.

[26] P.M. Smith and P.J. Edmonson, "An acoustic modem for microwave applications," *Proc. 1990 Canadian Conference on Electrical and Computer Engineering*, Ottawa, ON, pp. 4.4.1-4.4.4, Sept. 4-6 1990.

[27] I.D. Avramov, P.J. Edmonson and P.M. Smith, "A surface transverse wave based MSK system," *IEEE Trans. on Ultrasonics, Ferroelectrics and Frequency Control*, Vol. UFFC-38, No. 3, pp. 194-198, May 1991.

[28] P.M. Smith, P.J. Edmonson and C.K. Campbell, "An automatic gain controlled oscillating amplifier," *Electronics Letters*, Vol. 27, No. 21, pp.1919-1921, October 1991.

[29] P.J. Edmonson, P.M. Smith and C.K. Campbell, "Injection locking techniques for a 1 GHz digital receiver using acoustic wave devices," *IEEE Trans. on Ultrasonics, Ferroelectrics and Frequency Control*, Vol. 39, No. 5, pp. 631-637, September 1992. See Appendix E.

[30] S. Pasupathy, "Minimum shift keying: A spectrally efficient modulation," *IEEE Communications Magazine*, Vol. 17, No. 4, pp. 14-22, July, 1979.

[31] P.J. Edmonson, SAW Pulse Compression Using Combined Barker Codes," M.Eng Thesis in Electrical Engineering, McMaster University, Hamilton, Ontario L8S 4L7, Canada, March 1989.

[32] R. deBuda, "Coherent demodulation of frequency-shift keying with low deviation ratio," *IEEE Trans. Communications*, Vol. COM-20, No. 6, pp. 429-435, June, 1977.

[33] T. Khanna, *Foundations of Neural Networks*, Addison-Wesley, Massachusetts, 1990.

[34] S. Mori, Y.C. Suen, and K. Yamamoto, "Historical review of OCR research and development," *Proc. of the IEEE*, Vol 80, No. 7, pp. 1029-1058, July, 1992.

[35] P.K. Das and C.M. Decusatis, *Acousto-optic signal processing*, Artech House, Massachusetts, pp. 408-422, 1990.

[36] F. Heismann, "In-line electro-optic frequency translator for fiber-optic sensors," *Proc. SPIE*, Vol. 517 Integrated Optic Circuit Engineering, pp. 206-211, 1984.

[37] P.J. Edmonson, P.M. Smith and C.K. Campbell, "SAW-based carrier recovery without phase ambiguity for 915 MHz BPSK wireless digital communications," *Proc. 1992 IEEE Ultrasonics Symp.*, Oct. 20-23, Tucson, AZ, IEEE Cat. No. 92CH3118-7 pp. 241-244, 1992. See Appendix F.

[38] R. Seydel, *From Equilibrium to Chaos*, Elsevier, New York, pp. 198-206, 1988.

[39] F. Moon, *Chaotic and Fractal Dynamics*, Wiley-Interscience Publications, New York, 1992.

[40] P.J. Edmonson, C.K. Campbell and P.M. Smith, "Periodic pulse generator employing a driven unlocked surface acoustic wave oscillator," *Electronics Letters*, Vol 30, No. 13, pp. 1101-1102, June, 1994.

[41] T. Morita, Y. Watanabe, N. Tanaka and Y. Nakazawa, "Wideband low loss double mode SAW filters," *Proc. 1992 IEEE Ultrasonics Symp.*, Oct. 20-23, Tucson, AZ, IEEE Cat. No. 92CH3118-7, pp. 95-109, 1992.

[42] N. Mishima, Y. Yasuhara, Y. Kuroda, S. Ichikawa and S. Mitobe, "Mass productivity of wide band SAW resonator filter," in K. Shibayama (ed), *Proc. Int. Symp. SAW Devices for Mobile Comm.* Tokyo Press, Tokyo, Japan, pp. 142-147, 1992.

[43] R. Almar, B. Horine and J. Anderson, "High frequency STW resonator filters," *Proc. 1992 IEEE Ultrasonics Symp.*, Oct. 20-23, 1992, Tucson, AZ, IEEE Cat. No. 92CH3118-7, pp. 51-56, 1992.

[44] V.P. Plessky, "A two parameter coupling-of-modes model for shear horizontal type SAW propagation in periodic gratings," *Proc. 1993 IEEE Ultrasonics Symp.*, Oct. 31-Nov. 3, 1993, Baltimore, MD, IEEE Cat. No. 93CH3301-9, pp. 195-200, 1993.

[45] P.S. Cross and R.V. Schmidt, "Coupled surface-acoustic-wave resonators," *Bell System Technical Journal*, Vol. 56, pp. 1447-1482, Oct. 1977.

[46] T. Uno and H. Jumonji, "Optimization of quartz SAW resonator structure with groove gratings," *IEEE Trans. Sonics and Ultrasonics*, Vol. SU-29, pp. 299-310, Nov., 1982.

[47] V.P. Plessky and C.S. Hartmann, "Characteristics of leaky SAWs on 36 $LiTaO_3$ in periodic structures of heavy electrodes," *Proc. 1993 IEEE Ultrasonics Symp.*, Oct. 31-Nov. 3, 1993, Baltimore, MD, IEEE Cat, No. 93CH3301-9, pp.1239-1242, 1993.

[48] C.S. Hartmann and V.P. Plessky, "Propagation, attenuation, reflection and scattering of leaky waves in Al gratings on 41-, 52- and 64-$LiNbO_3$," *Proc. 1993 IEEE Ultrasonics Symp.*, Oct. 31-Nov. 3, 1993, Baltimore, MD, IEEE Cat, No. 93CH3301-9 , pp.1247-1250, 1993.

[49] D.F. Thompson and B.A. Auld, "Surface acoustic wave propagation characteristics," in K. Shibayama (ed), *Proc. Int. Symp. SAW Devices for Mobile Comm.* Tokyo Press, Tokyo, Japan, pp. 49-58, 1992.

[50] Y. Shimuzu, "Leaky SAW propagation characteristics," in K. Shibayama (ed), *Proc. Int. Symp. SAW Devices for Mobile Comm.* Tokyo Press, Tokyo, Japan, pp. 59-66, 1992.

[51] K.Y. Hashimoto, M Yamaguchi and H. Kogo, "Interaction of high-coupling leaky SAW with bulk waves under metallic-grating structure of 36^{o}YX-$LiTaO_3$," *Proc. 1985 IEEE Ultrasonics Symp.*, Oct. 16-18, 1985, San Francisco, CA, IEEE Cat, No. 85CH2209-5 , pp.16-21, 1985.

[52] K. Yaminouchi and M Takeuchi, "Applications for piezoelectric leaky surface waves," *Proc. 1990 IEEE Ultrasonics Symp.*, Dec. 4-7, 1990, Honolulu, HI, IEEE Cat, No. 90CH2938-9, pp.11-18, 1990.

[53] H. Engan, K.A. Ingebrigsten and A. Tonning, "Elastic surface wave in α-quartz: observation of leaky surface waves," *Appl. Phys. Lett.* ,Vol. 10, pp. 311-313, June, 1967.

[54] K.Y. Hashimoto, M. Yamaguchi and H. Kogo," Experimental verification of SSBW and leaky SAW propagating on rotated Y-cuts of $LiNbO_3$ and $LiNbO_3$," *Proc. 1983 IEEE Ultrasonics Symp.*, Oct. 31-Nov. 2, 1983, Atlanta GA, IEEE Cat, No. 83CH1947-1 , pp.345-349, 1983.

[55] W.H. Louisell, *Coupled Mode and Parametric Electronics*. John Wiley and Sons: New York, 1960.

[56] C.K. Campbell, P.M. Smith and P.J. Edmonson, "Aspects of modelling the frequency response of a two-port waveguide-coupled SAW resonator-filter," *IEEE Transactions on Ultrasonics, Ferroelectrics and Frequency Control*, Vol. 39, no. 6, pp. 768-773, November 1992.

[57] B.A. Auld, *Acoustic Fields and Waves in Solids*, Volumes 1 and 2, John Wiley and Sons, New York, 1973.

[58] D.P. Morgan, *Surface-Wave Devices For Signal Processing*, Elsevier, Amsterdam, 1985.

[59] E. Dieulesaint and D. Royer, *Elastic Waves in Solids*, John Wiley and Sons, New York, 1980.

[60] V.M. Ristic, *Principles of Acoustic Devices*, John Wiley and Sons, New York, 1983.

[61] G.W. Farnell, "Elastic surface waves," in H. Matthews (ed), *Surface Wave Filters*, John Wiley and Sons, New York, Chapter 1, 1977.

[62] M.F. Lewis, "On Rayleigh waves and related propagating acoustic waves," in E.A. Ash and E.G.S. Paige (eds), *Rayleigh-Wave Theory and Application*, Springer-Verlag, Berlin, pp. 122-130, 1985.

[63] G.S. Kino, *Acoustic Waves: Devices, Imaging, and Anolog Signal Processing*, Prentice-Hall Inc., Englewood Cliffs, 1987.